Self-Powered Multi-Function Harmonics-Based Wireless Sensing System Using Graphene Bioelectronics

BY

MEHDI HAJIZADEGAN
B.S., Shahid Rajaei University, Tehran, 2010
M.S., Tarbiat Modares University, Tehran, 2013

DISSERTATION

Submitted as partial fulfillment of the requirements
for the degree of Doctor of Philosophy in Electrical and Computer Engineering
in the Graduate College of the
University of Illinois at Chicago, 2020

Chicago, Illinois

Defense Committee:

Pai-Yen Chen, Chair and Advisor
Piergiorgio Uslenghi
Danilo Erricolo
Vitaly Metlushko
Jie Xu, Bioengineering

Copyright by

Mehdi Hajizadegan

2020

ACKNOWLEDGMENTS

First, it would be impossible to overstate the thanks I owe to Pai-Yen, whose mentorship for the past four years has been beyond formative. It is a great opportunity for me to work on my Ph.D. studies with Prof. Pai-Yen Chen as my adviser who have been supportive of my career goals and who worked actively to provide me with the protected academic time to pursue those goals. Thanks for everything!

I am grateful to all of those with whom I have had the pleasure to work during this and other related projects. Each of the members of my Dissertation Committee has provided me extensive personal and professional guidance and taught me a great deal about both scientific research and life in general.

I thank all the staff members of the ECE department at both Wayne State University and University of Illinois at Chicago for their help during my Ph.D. study.

Nobody has been more important to me in the pursuit of this project than the members of my family. I would like to thank my parents; whose love and guidance are with me in whatever I pursue. They are the ultimate role models. Most importantly, I wish to thank my best friend and my research partner, Maryam, who provides unending inspiration.

MH

CONTRIBUTION OF AUTHORS

In Chapter 3, a graphene-based harmonic sensor is introduced. I was responsible for modeling graphene field-effect transistor (GFET) by physics-based drift diffusion model, designing, simulating and developing the RFID sensor including fabrication, measurements and manuscript editing which has been published in [17],[215]. Other authors contributed in developing of antenna simulation and measurements setup and editing the manuscript.

The content of Chapter 5 is based upon the self-powered graphene sensing modulators. A portion of the content of this Chapter has been published in [17],[97]. I was responsible for the design and simulation different circuit topologies using GFET model. All other authors helped me to improve the proposed formulas used in the paper and edited the manuscript.

In Chapter 6, I propose a novel harmonic sensing system comprising flexible graphene antenna. I was responsible for designing, simulating, of this antenna system. A version of this Chapter has been published in [17],[122]. Other authors contributed in fabrication and measurement of the antenna as well as editing the manuscript.

TABLE OF CONTENTS

CHAPTER PAGE

LIST OF FIGURES

FIGURE PAGE

LIST OF FIGURES (continued)

FIGURE PAGE

LIST OF FIGURES (continued)

FIGURE PAGE

SUMMARY

We introduce a new paradigm of low-noise and low-interface wireless sensing system, which receives a radio signal at the fundamental frequency f_0 and retransmits high harmonics (e.g. second harmonic $2f_0$) with the conversion gain being modulated by the targeted agent. Specifically, the harmonic-transponder sensor (or harmonic sensor) is based on all-graphene radio-frequency (RF) circuits. Thanks to unique properties in graphene field-effect transistors (GFETs), such as the ambipolar carrier transport and the shiftable charge neutral point, the frequency modulation and chemical/molecular sensing functions can be combined into a single RF component (i.e., chemically-sensitive modulator). By transmitting and interrogating RF signals with orthogonal frequencies, the backscattered signal can be free from severe background clutters, jamming, multipath-scattering and background electromagnetic interfaces, regardless of the sensor's scattering cross-section. Moreover, a GFET-based RF modulator circuit may enable dual/multi-functional sensing by employing the machine learning approach to interpret output harmonics. The proposed graphene-based harmonic sensor may be used to a variety of sensing applications, including, but not limited to, real-time monitoring of chemical and gas exposures, as well as biological agents. Further development of such technique may have an impact on wearable and implantable devices, internet of things (IoTs), industry 4.0, and smart city.

I. INTRODUCTION

With the rapid development of network communications, wireless sensing systems attracted more attentions due to emerging new generation of communications such as industry 4.0 and internet of things (IoTs) [1]-[4]. On the other hand, growing demands for wireless communications beyond the earth populations to making connection between machines, humans, and recently objects, forced the technologies to fill the gaps and overcome hurdles to obtain worldwide internet-based infrastructures [5]-[7]. Sensor technologies, which have been improved during the decades thanks to the new micro/nano fabrication techniques as well as electronic devices invention, known as the main part of these systems, potentially viable to develop the new generation of communications. Since miniaturized wireless sensors suffer from required power source which might increase complexity, cost, and lifetime, thus inventing passive radio frequency identification (RFID) tags improved feasibility of such systems [8]-[15]. Although these passive tags have been inexpensive and small size which work in zero power, backscattering field without any amplification is communicating just in short distance due to background interferences. Hence harmonic RFID sensors have been introduced to overcome the drawback of backscattering clutter noise by taking advantage of the frequency difference between received and modulated signals [16]-[22]. However, using the active and complicated harmonic sensing system still has a room for improvement to be proper for future applications such as IoTs. Therefore, in this project we are first proposing a compact sensing system based on the dual functionality of graphene-based electronics to operate as

a compact sensor and frequency modulator. Afterward, we plane to develop self-powered graphene-based circuit which benefits IoTs applications. Furthermore, we investigate the possibility of making an integrated all-graphene module beneficial for wearable healthcare application as a smart contact lens. Finally, using machine learning approach and system-level demonstration we will develop multi-functional harmonic sensing system toward smart city applications.

1.1. State of the art

The word “Internet of Things” (IoTs) which has been intended by Kevin Ashton in 1998, refers to a global internet-based infrastructure that overcomes the gap between physical objects and the informational systems [5]. In other words, machine-to-machine and human-to-computer communications complemented with the new paradigm of things communication [6]; it means that physical objects are promoted to the active “smart objects” suitable for communicating through the internet. Hence any ordinary object either stationary or mobile, such as a smartphone, car, fire detector, any apparel, book, groceries, industrial facilities, laboratory facilities, materials, auto parts, bags, army facilities, etc. can be introduced in IoTs. During the last two decades, many applications have been emerged in the terms of IoTs to provide connection services including workers [24]-[26], assets [25],[27]-[28], vehicles [29]-[32], commerce [33]-[35], mines [36],[37], and healthcare [38]-[42] as schematically shown in Fig. 1.1 [24]. The importance of this technology will be clearer when we know that the number of devices connected per person became more than earth population from 2008 which is estimated 6.58 devices per person until 2020 (totally 50 Billion devices connected) based on the Cisco report [6], as schematically shown in Fig. 1.2 [6]. Since the speed of the technologies and internet progression is slower

than growing the number of devices, implementation of such infrastructure as IoTs seems mandatory to manage this huge number of devices and objects.

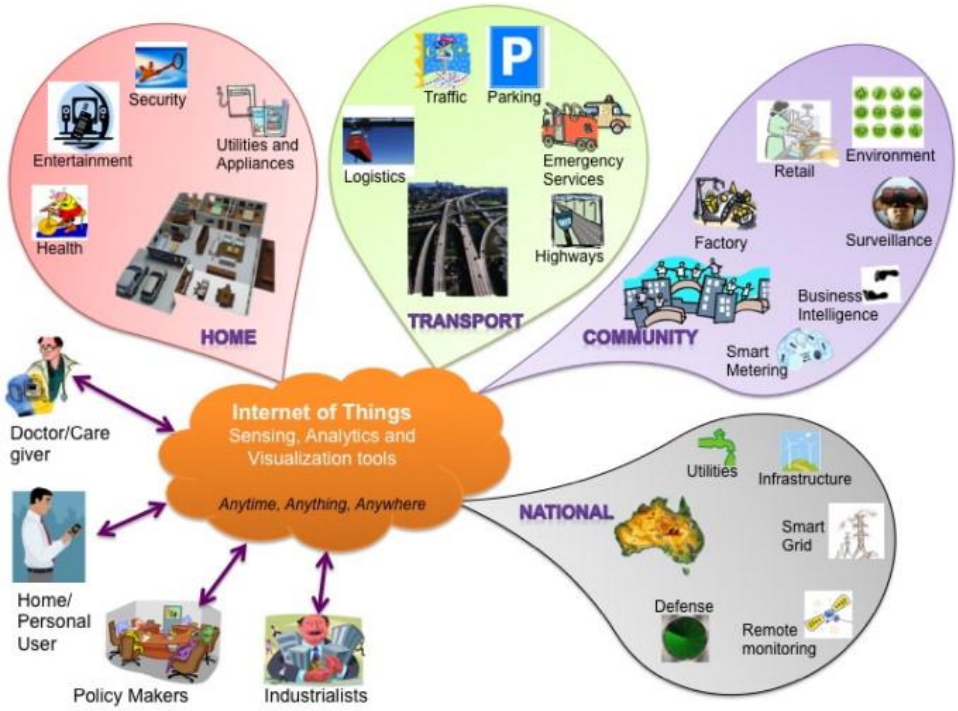

Figure 1.1. Schematic of IoTs possible users and applications [24].

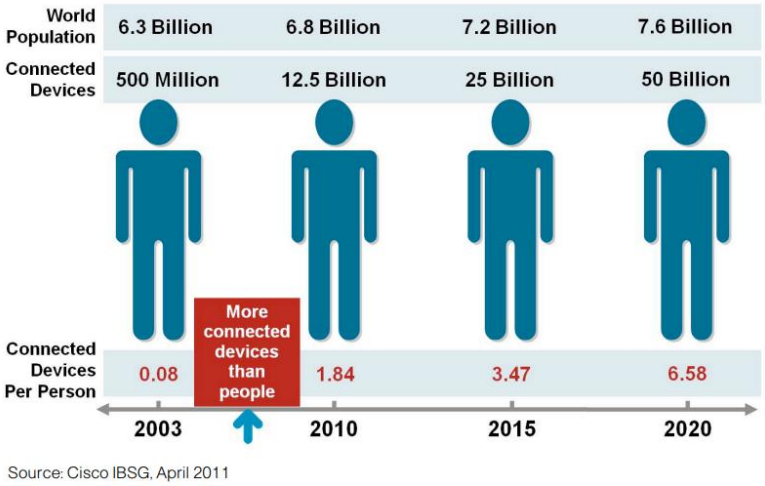

Figure 1.2. The Internet of Things was "Born" between 2008 and 2009 [6].

In order to collecting data, monitoring miscellanies quantities (e.g. temperature[43], pressure, liquid volume, humidity, mechanical strain, and chemical reaction, [22],[43]-[53]), and controlling the objects performance (e.g. vehicle navigation [54]-[57], robot controls [58]-[63], remote controls of facilities [64]-[66]), sensors play significant rule under IoTs applications. Sensor technologies have been improved during the decades consequent to the new applications demand like IoTs. Enhancing the sensing systems based on the elevated fabrication techniques such as "Micro-Electro-Mechanical Systems" (MEMS), leads to emerging new applications like human body wearable sensors for healthcare monitoring as well as monitoring hazardous and inaccessible environmental conditions for various purposes [67]-[76]. However, the sensors for IoTs applications should be viable to wirelessly connect to the internet-based cloud without huge energy consumption. Hence developing low-cost smart sensors consistent with the internet-based

infrastructure engender to several technological challenges. Figure 1.3 [7] shows a block diagram of conventional wireless sensors that need to be as compact as possible for IoTs applications. The most important challenge of this block diagram is the power supply which is required to provide the energy for other blocks such as signal processing and wireless communication [7]. To provide consistent power supply we need consider different parameters like the size, lifetime, safety issues, environmental impact, cost, and type of battery (Alkaline, Lithium-Ion, NiCad, NiMH, Lead-Acid) [7]. On the other hand, using renewable energy sources as photovoltaic cells and rectennas have the same cost issues. Thus, for wireless applications, especially here for IoTs, designing zero-power sensors could dramatically spread its utilization.

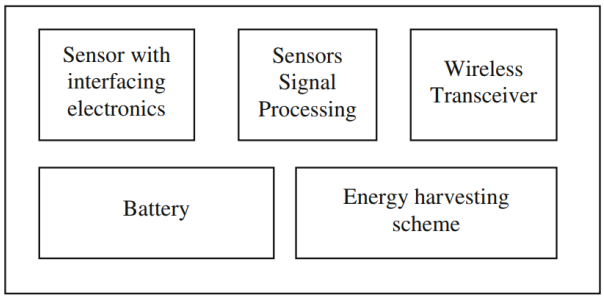

Figure 1.3. Block diagram for conventional wireless sensors [7].

Radiofrequency identification (RFID) has been one of the most attractive wireless sensing technique during recent decades due to its potentially battery-free, ultralow-profile, and ultralow-cost features [8]-[15]. Traditionally, RFIDs constructed by three main parts as RFID readers, tags, and software [13], as the block diagram and their connection shown

in Fig. 1.4 [77]. Indeed, depending on how to supply energy to the tag, they can be categorized into three classes as passive, active, and semi-active tags [13], as the detailed classification shown in Fig. 1.5 [77]. Although an internal battery is utilized to continuously supply an active and semi-active RFID tag, there is no internal power supply needed for a passive tag (typically a portion of the transmitted signal will supply the loaded tag), where RF power transmitted to the tag is backscattered after modulation without any amplification [13]. Since the tag is free from the power source, it can be very small and low cost suitable to use in IoTs applications. However backscattered RF signal, which is attenuated due to interrogated with a passive tag, is not detectable for relatively long distance. In the other hand such attenuated signal typically suffers from non-negligible background noises, clutters, and backscattered echoes due to the same frequency of transmitted and backscattered signals from the ultra-small tag. Hence advent of a zero-power sensor capable to operate for longer distance free from noises, clutters, and backscattered echoes will strongly benefit several IoTs applications, as smart homes [78]-[81], smart city [82]-[84], healthcare monitoring [38]-[42], smart retail [85]-[86], and industry 4.0 [1]-[4], to name a few.

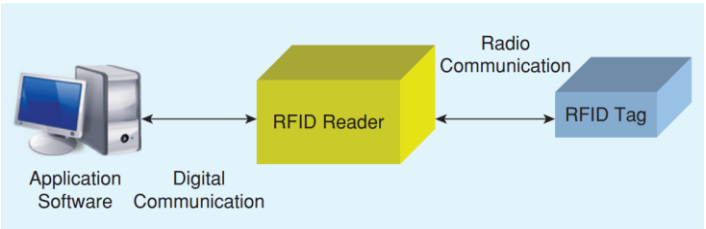

Figure 1.4. Block diagram for a typical RFID system and the connections [77].

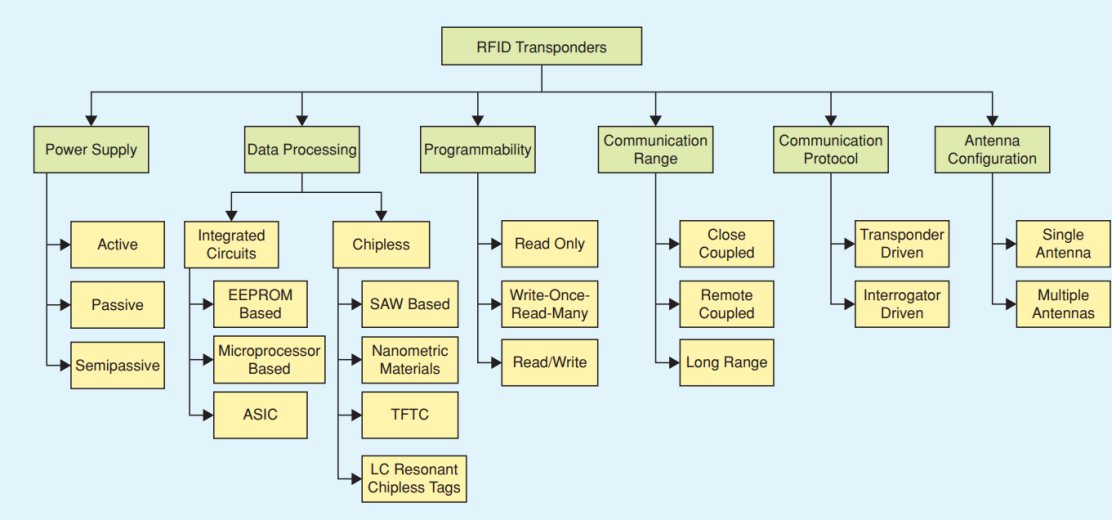

Figure 1.5. Detailed classification of RFID transponders available on the market until 2008 [77].

Nonlinear radar emerged in opposition to the leaner one, exploits the different frequencies between radar waves and reflected waves from nonlinear targets [87]-[93]. In this mechanism due to use nonlinear target, the reflected waves are propagated in a different frequency which offering high rejection of backscatter noise and clutter; thanks to this advantage, it has been used for several applications especially for tracking insects [94],[95], bees [18],[19], and vital signs monitoring [96], as two examples shown in Fig. 1.6. Since the nonlinear target needs a much higher power to generate a comparable signal to noise (SNR) rather than linear ones, in addition to the distance limitation based on the Friis path loss [92], this mechanism for radars still seems not highly applicable. However, this mechanism developed to the sensing systems as harmonic sensors where show the capability to overcome the backscattering RFID limitation for IoTs applications.

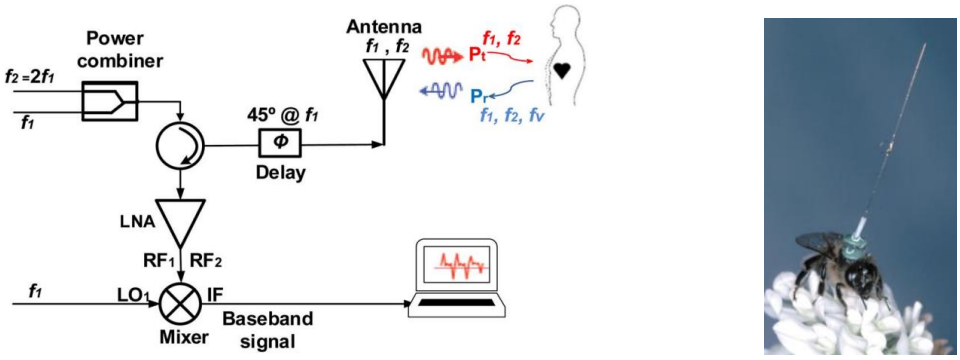

Figure 1.6. Harmonic radar

Architecture of harmonic radar system for vital signs monitoring (left) [96], and a bee wearing transponder for flight tracking using harmonic radar system (right) [19].

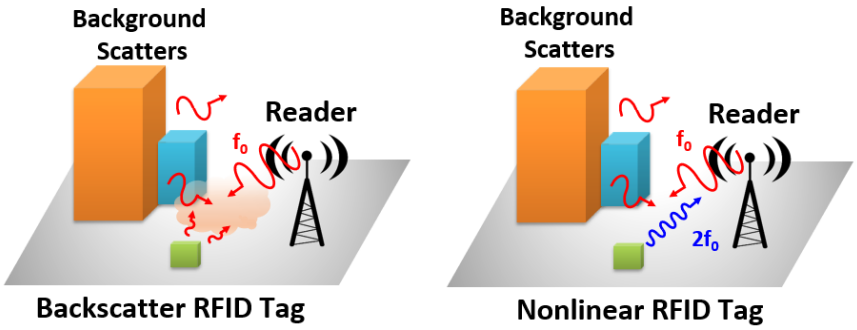

Figure 1.7. Backscatter-RFID sensor

Schematics of backscatter-RFID sensor (left) and harmonic sensor (right) [97].

The working principle of harmonic sensors is like harmonic radars, where the nonlinear target here is a sensor that modulating the received signal tuned by the miscellaneous quantities (e.g. pressure, temperature, humidity, chemical or bioagents, micro-liter liquid volume and gas molecules) to be measured. In this type of sensing system, the RF signal at the fundamental frequency f_0 is received with the RFID tag and after modulation is retransmitted to the reader at a higher harmonic frequency (e.g. second harmonic $2f_0$) [16]-[22]. Since the backscattered signal frequency differs from the fundamental tone, the modulated signal could be free from severe background clutters, jamming, multipath-scattering and background electromagnetic interfaces, as illustrated in Fig. 1.7 [97]. As mentioned above, generating higher frequency harmonics by a nonlinear tag typically needs more energy which means making a passive RFID in this mechanism is doubtful. Furthermore, compare with the passive RFIDs, this harmonic sensor tag needs at least four elements as a receiving (Rx) antenna, a filter and sensor, a harmonic generator (which typically is an active device such as diode) and a retransmitting (Tx) antenna, as a block diagram and an example of temperature harmonic sensor are shown in Fig. 1.8 [98]. Hence, to make this sensing system consistent with IoTs application we need to overcome challenges like the system complexity and power consumption which may result in the design of a passive RFID free from backscattering interference. Very recently a graphene device has been invented which shows the extraordinary capability to operate as a nonlinear device to generate higher harmonic frequency as well as its molecular-level sensitivity useful for sensing systems [99]-[110]. Thus, inspired with this device capability we can propose a compact harmonic sensor, while the sensor and frequency modulator can be integrated into a single device. Beside, another way to make this system even smaller, is

that combine the Rx and Tx antenna in a dual-band antenna which will be investigated in this project.

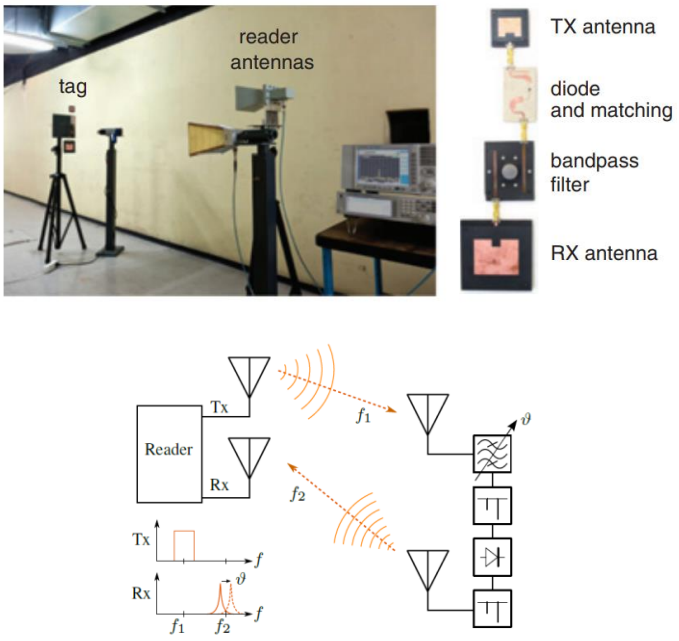

Figure 1.8. Harmonic tag diagram

The wireless setup, harmonic tag elements, and harmonic tag block diagram for a temperature harmonic sensor [98].

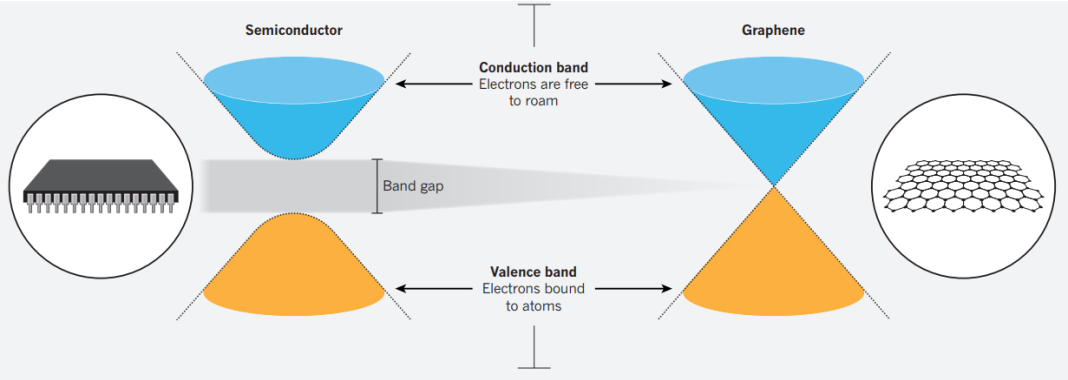

Figure 1.9. Graphene bad-diagram

Schematic of band gap compression of semiconductor and graphene; graphene known as gapless material that sits between metal and semiconductor [123].

Single-layer graphene comprising one-atom-thick carbon arranged in honeycomb lattice as a two-dimensional material has attracted great scientific and technological interest since its first-time appearance in 2004 [99],[100]. The extraordinary electrical, optical, and mechanical characterization of graphene such as high carrier mobility and electrical conductivity, strong conductivity dependency on chemical and electrostatic gating effect, optically transparent, highly flexible, lightweight, mechanical robustness, etc., make it unique structure beneficial for a broad application fields [99]-[122]. We know that electrons must move through a hurdle called bandgap to generate electrical current; the bandgap is ultra-large for insulators, small for semiconductors, and near-zero for metals [123]. However, graphene sits on the boundary of metal and semiconductor which is known as gap-less material as schematically illustrated in Fig. 1.9 [123], where its ultra-small band gap benefits moving electrons to generate current 100 to 200 times faster than

semiconductors as silicon [123]. Thus, this advantage makes graphene an interesting material for RF and optical frequency applications.

Besides, the graphene-based nano-sensors emerging by a molecular-level sensitivity to certain gas and biomolecular agents can be widely useful by the concept of the internet of things (IoTs). The most recent approach of graphene-based electronics is the graphene field-effect transistor (GFET) which has had a revolutionary impact on the radio-frequency and analog platform due to a unique working principle compare with the conventional semiconductor devices [114]-[120]. In this type of FET, graphene plays the channel role (as schematically shown in Fig. 1.10 including small-signal equivalent RF operation [124]); thus, based on the ambipolar charge transports in the gapless graphene, drain and source in GFET have the same effect on the current which means the drain current for both negative and positive gate voltage will be positive [124]. In ambipolar devices, unlike unipolar MOSFET, with a constant carrier majority which is determined by channel doping in the fabrication process, conduction can be switched between p-type and n-type; in an ambipolar FET, this switching is controlled by gate bias that controls the position of Fermi level. Ambipolar FETs have been demonstrated based on several types of semiconductors such as graphene [125], carbon nanotubes [126], amorphous silicon [127], and organic semiconductor heterostructures [128]. However, graphene is the only high mobility and well scalability semiconductor beneficial for RF and high-frequency devices [124]. Thanks to this feature, with a gate voltage below the minimum conduction point (sometimes called charge neutral point "V_{cnp}" (Dirac point)) hole carriers, will be dominant in charge transport while for the voltage above this point the dominants carriers will be switched to electrons. Hence as schematically illustrated in Fig. 1.10 (right), Drain current- Gate voltage (I_{ds}-V_{gs})

characteristic has a unique symmetric “V” shape which makes this device excellent to achieve frequency doubling for RF applications [124]. In this regime, the incoming RF signal applied to the gate can generate the higher frequency harmonics on the drain output. Furthermore, modulation of amplitude, as well as phase, is possible based on the symmetric characteristics as illustrated in Fig. 1.11 [129]. For the GFET with zero charges neutral point “V_{cnp}” the applied signal at the fundamental frequency f_0 with the zero-offset input voltage V_{in} generating the higher frequency harmonics at the drain output. Here the amplitude of the output harmonics is related to the slope and shape of the I_{ds}-V_{gs} curve for the designed GFET as well as the value of the Dirac point. Subsequently detuning of the Dirac point can be monitored by the amplitude of the output harmonics. Therefor one beneficial application of this frequency multiplier can be defined as the sensing Dirac point position, while we know that it is tunable with the chemical dopants (e.g. gases or molecules) which may be attached to the graphene surface. Hence, we can easily design a harmonic sensor using one single GFET as the working principle is schematically shown in Fig. 1.12 (left) [17]. From the sensing point of view, graphene shows many advantages such as high sensitivity, because it is a two-dimensional material which whole of the dopants volume will expos to the surface absorber; in addition, since it has conductivity very close to metals, very small extra electron can dramatically change the carrier concentration [108]. Thus, here using a single device we can create a compact multifunction sensor and frequency multiplier which benefits an integrated harmonic sensing system.

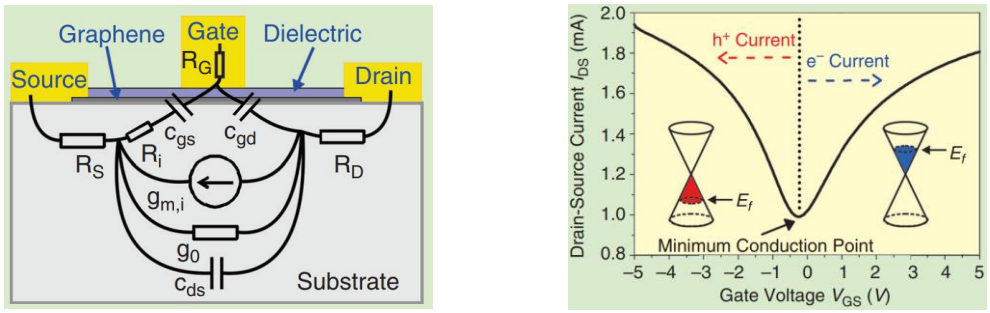

Figure 1.10. Field effect transistor and graphene characteristics

Typical structure of a graphene field effect transistor (left). "The small-signal equivalent for RF operation is an overlay on top of the device schematic. R_S and R_D are the source and drain access resistances. R_i is the intrinsic resistance. $g_{m,i}$ is the intrinsic transconductance. g_0 is the output conductance. C_{ds} is the source-drain capacitance. C_{gs} and C_{gd} are the gate-source and gate-drain capacitances. R_G is the resistance in the gate electrode". Conical-shape band structure of graphene and ambipolar conduction in GFETs (right) [124].

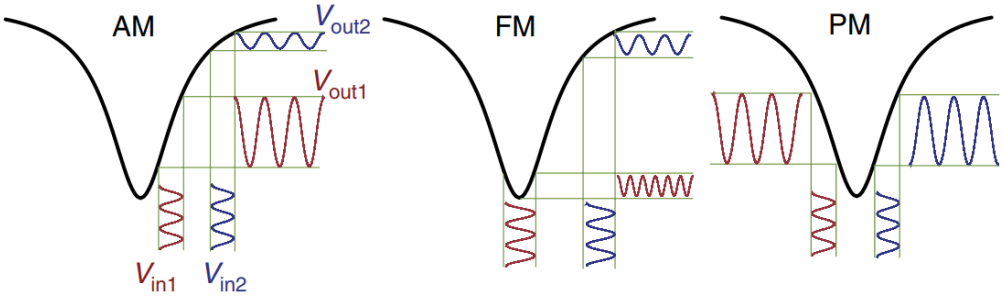

Figure 1.11. GFET based modulations

Illustrations of amplitude, frequency, and phase modulation of a sinusoidal wave achieved by operating a single ambipolar graphene transistor at different gate biases. [129].

The first step to fabricate a graphene-based device is growing the graphene. During the decades after the advent of graphene, many ways have been proposed to produce graphene in bulk quantity and high-quality in both single-layer and multi-layer synthesis [125], [130],[133]. Chemical vapor deposition (CVD) is well known as the frontier technique to cost-efficient and simply growing graphene onto the metallic substrate. For RF application, the fabrication of desired high-frequency GFET has been achieved by using wafer-scale graphene grown by CVD and standard nanolithography processes [120]. Thus, we can design our GFET-based circuit for the harmonic sensing approach by cutoff frequency (f_T) up to 300 GHz [120]. Furthermore, with the transfer technique of graphene, not only electronic device such as GFETs fabrication is easily feasible, but also with some optimization, we are able to make fully transparent and flexible graphene-based chemical sensor on PET substrate. In this sensing regime, we will take the advantage of chemically-sensitive conductivity of the graphene to measuring the concentration of gas, chemical, or biological dopants (e.g. bacterial or infectious agents) on the graphene surface. Consequently, thanks to the frequency modulation by GFET, we will develop a new generation of harmonic based sensing systems comprising graphene electronics which may lead to a compact system suitable for IoTs applications.

Figure 1.12. GFET frequency modulator overview

Illustrations of frequency modulation by a single GFET for different V_{cnp} positions with schematics of frequency modulation in chemically-doped ($|V_{cnp}| > 0$ V) GFETs (left). Architectures for a harmonic sensor based on the new graphene-based sensing-modulator circuit that integrates several functions into a single module (right) [17].

1.2. Primary sensing approaches by graphene flexible tags

Graphene emerged as one of the most appropriate candidates for sensing approach while a combination of several advantageous features such as its optical transparency, mechanical flexibility and strength, and chemical-dependent conductivity, all can satisfy what a flexible compact sensor may need. The first practical step for this project has been realizing sensing approach based on the flexible electronic and grown graphene. One of the primary studies is transferring the single-layer graphene to the flexible and heat-resistive transparent-substrate to analyze the graphene sensitivity and compatibility to the flexible substrate. Here we also use silver ink printing to create flexible contact with the graphene sheet. Figure 1.20 (a) shows the image of the graphene resistive sensor consisting of the graphene sheet with the length and width L and W respectively, contacted to the silver ink printed on the flexible substrate. For this step, some different samples with various W and L ratios are generated to verify the resistance and conductivity on graphene-channel. Figure 1.20(b) shows a good match between experimental measurement and theoretical calculation of resistivity ρ for different channel ratio, as well as the resistivity variations with adding the ammonia gas concentrations. Here the deviation of the resistivity is monitored by using different ammonia concentrations which follows our analytical expectation. On the other hand, for real-time monitoring, we used a sealed chamber with a constant gas injection on a room temperature heat controller, like the setup shown in Fig.

1.21(a). Here the flexible sensor connected to a multimeter is placed inside the chamber and the deviation of sample resistance is monitored during a long-time period and is recorded by real-time monitoring software. Figure 1.21(b) shows the resistance change of the graphene channel in the response to the different injected gas concentrations which verifies the working principle of the simple gas sensor using a resistive flexible circuit comprising a single-layer graphene and silver ink printing.

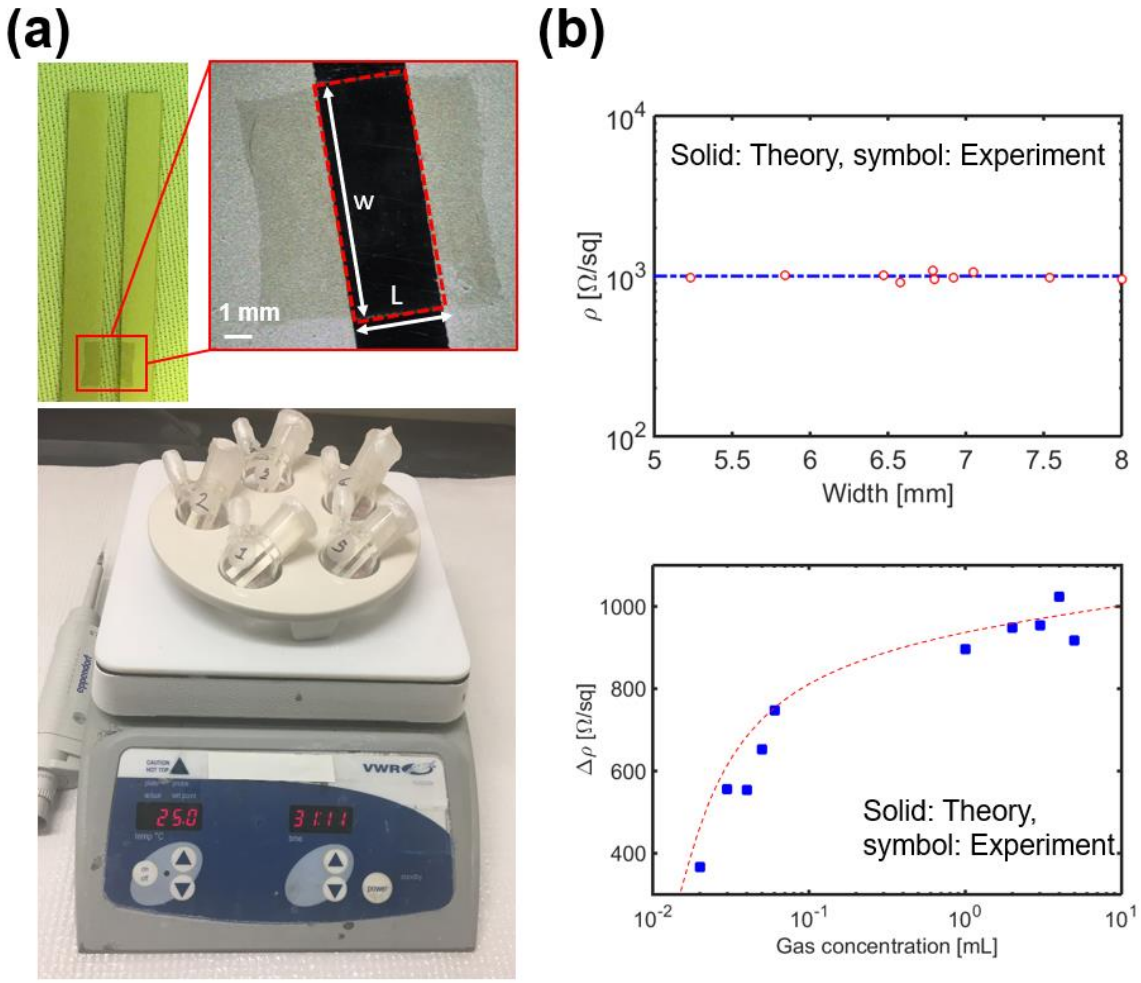

Figure 1.13. Graphene-based flexible resistive sensor

(a) The image of flexible sensor comprising graphene sheet and silver ink (top) and different samples inside the sealed chamber on room temperature heater (bottom), (b) The constant resistivity for different sample sizes (top), and resistivity variation by increasing ammonia gas concentration (bottom).

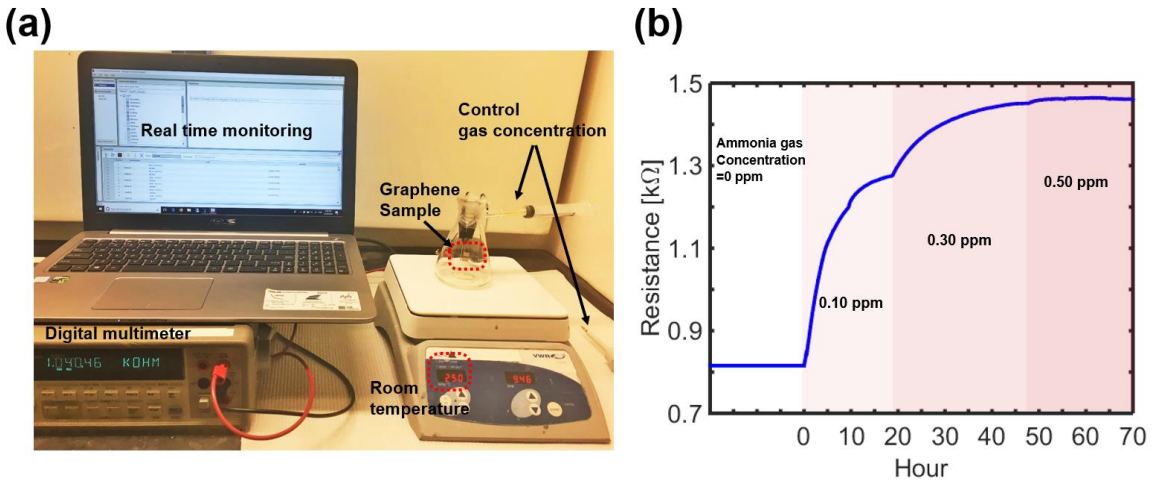

Figure 1.14. Real-time gas concentration monitoring by graphene sensor

(a) The setup of resistive sensor in connection with real-time recorder for gas-concentration monitoring, (b) variation of sample resistance during the time periods in response to the gas concentration.

In the next step, we experimentally investigated the possibility of wirelessly monitoring such a sensing system using an inductively interrogated system. For this purpose, we designed a planar coil structure viable to create an RL circuit in connection with the graphene sheet at the center. The designed structure is fabricated first using silver ink printing on the flexible substrate and tested with putting LED in the place of graphene to examine the mechanical strength and water resistivity as shown in Fig. 1.22(a). Here, the suggested wireless system needs adding a capacitor to create an RLC resonance structure which enables frequency monitoring. Although the designed coil consisting the parasitic

capacitance, the miniaturized design will shift the resonance frequency to a higher range than our system design requirement. Hence to monitor such an RL tag we take the advantage of a quantum physic concept known as PT-symmetry which can result in the resonance frequency appearance without the need to adding capacitance to our designed wireless sensor. For realizing such a system, we need a couple an exact symmetry RL to the sensor part, however with the negative sign of the resistance, as schematically shown in Fig. 1.22.(b). Here we can consider the wireless system as a non-Hermitian Hamiltonian system which shows a resonance frequency very dependent on the coupling coefficient as well as the variable resistance, in which the detail of this concept can be found in [134]-[136]. Thus, our flexible sensor comprising the silver ink planar coil and graphene sheet as the variable resistance can be modeled with the schematic circuit shown in Fig. 1.23(a), which with inductively interrogation with an active RL reader can generate the frequency resonance in the PT-symmetry regime. To experimentally realize and test the PT-symmetric RL system, we replace the flexible sensor with a PCB circuit comprising planar coil and variable resistance equal to the measured the equivalent inductive and resistance of silver in coil and graphene sheet, respectively. The reader also fabricated by the same planar coil on PCB with a negative impedance convertor (Colpitts oscillator) which provides the PT-symmetry requirement. As a result, in the PT-symmetry phase, we can find the resonance frequency that shows ultra-sensitivity to the non-Hermitian parameter defined as Υ in Fig. 1.23 (b). Here a dramatic frequency shift is observable in response to the resistance change. Nevertheless, a comparison of the counter of shifted resonance frequency in the reflection spectrum in Fig. 1.23. (c) and (d) for PT-symmetry reader and passive coil shows the huge sensitivity to the resistance is viable using active reader while

the passive coil just shows a constant resonance frequency which is happened through the matching between 50 Ω load and the input impedance of network analyzer (VNA) to the reader part. Hence as a conclusion, we theoretically investigate and experimentally demonstrate the graphene-based chemical sensor in a flexible and transparent scheme of wireless resistive sensing system which is realized by silver ink printing and single-layer graphene wirelessly communication with an active reader to take the advantage of a physical concept known as PT-symmetry. This primary experimental analysis verifies the graphene capability for wireless sensing systems which benefits our further study on graphene-based sensors as the main part of this dissertation.

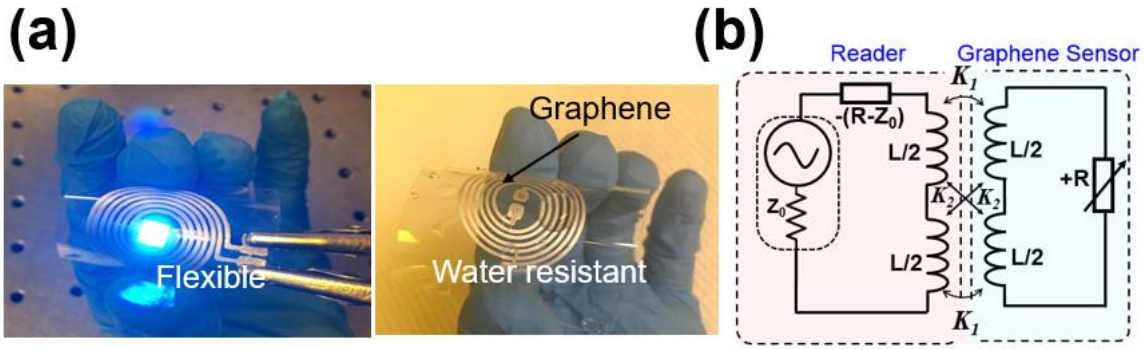

Figure 1.15. Graphene-based flexible wireless resistive senor

(a) The image of flexible tag for wireless sensing comprising silver ink coil and graphene sheet (left image shows the test of coil conduction with placing LED instead of graphene and the right image shoe flexibility and water resistivity of graphene-silver ink tag), (b)the equivalent circuit consist of RL sensor inductively coupled to the active reader.

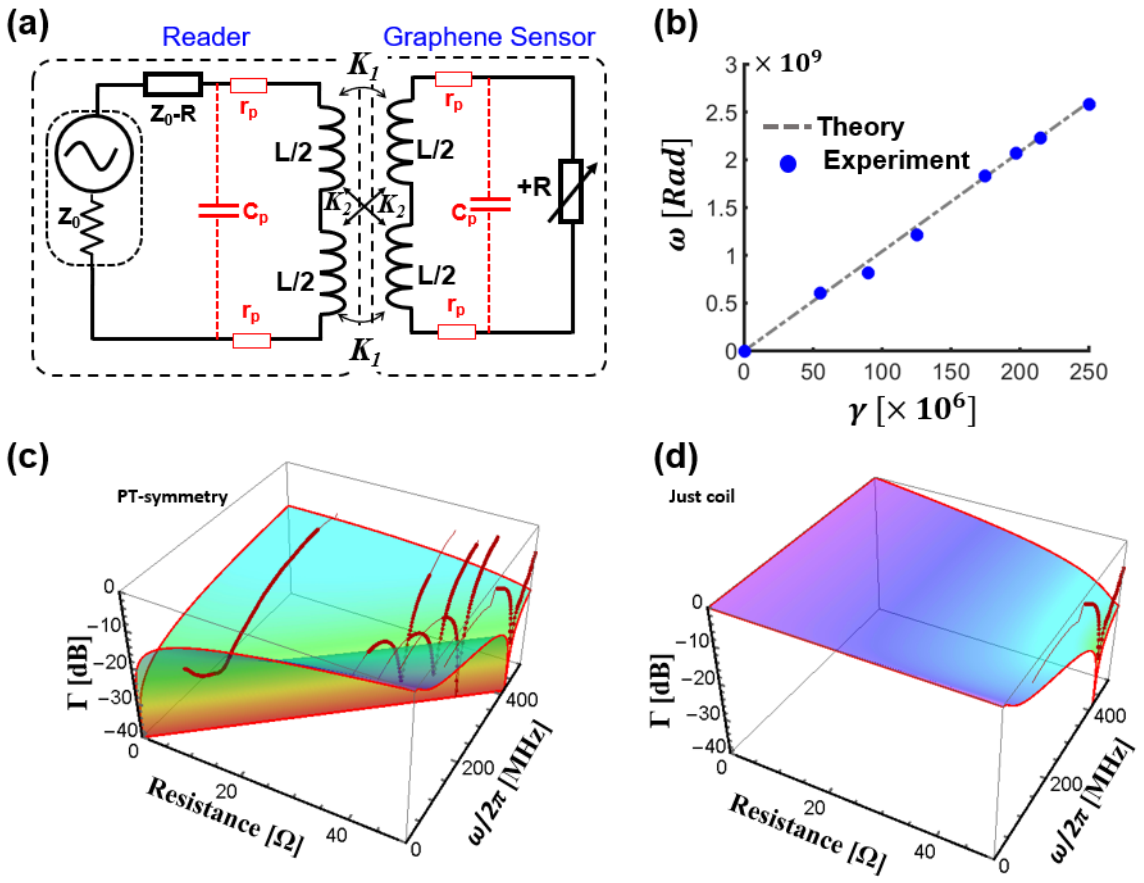

Figure 1.16. PT-symmetric wireless resistive sensor

(a) The equivalent circuit consist of RL sensor (can be the designed graphene-silver ink tag or its equivalent PCB RL circuit) inductively coupled to the active reader, (b) resonance frequency shift in the response to non-hermiticity parameter, (c) contour of the reflection frequency spectrum variation in the response to the resistance variation, and (d) similar to (c) but for the passive system without PT-symmetry realization.

1.3. Thesis organization

In Chapter 2 we review the RF and high-frequency applications of two-dimensional materials devices. By introducing the characteristics and advantages of the most applicable 2D-materials such as graphene and TMDs, we review the possible functions for the high-frequency circuits designed based on these devices. At the end of this chapter, the most considered application by this dissertation is introduced as the harmonic-sensing approach taking advantage of graphene field-effect transistors (GFET). Here we explain how multiple advantages of graphene can benefit the noise-free, light-weight, and transparent wireless sensing system.

In chapter 3, compact harmonic sensing is demonstrated in detail based on the single GFET. Here we show the working principle of the GFET-based harmonic sensor and how the single transistor operates as a frequency multiplier as well as chemical/biosensor. Then we modeled the transistor with the physics-based analytical method. Further, we verify our analytical model with the experimental measurement of the fabricated back-gate GFET. Thus, we conclude that the model can accurately be used for circuit designs and analysis through high-frequency and more complicated applications. Finally, we experimentally demonstrate a zero-bias RFID PH-sensor by a PCB based circuit designed for near-field communication (NFC). As a result, a compact GFET-based RFID tag is experimentally proofed the concept of harmonic sensing for PH detection.

Chapter 4 is a step forward to practical bio/chemical sensing models. In this chapter, we investigate the possibility to have a multifunctional harmonic sensing system based on the functionalized GFETs. Here we designed some possible circuits comprising functionalized GFETs and show that with analyzing the higher frequency harmonics

conversion gain can beneficially provide the capability to detect and monitor the concentrations of multiple chemical/bioagents. On the other hand, we propose the use of a machine learning technique to improve the feasibility of analysis higher harmonics conversion gain for retrieving the concentrations of multi-agents via training a neural network (NN) with numerous combinations of data of frequency components.

In chapter 5, based on the proof of concept from earlier experimental verifications, we design some feasible circuits based on the modeled GFET viable to operate as self-powered sensing modulators. In this paradigm, we utilize some conventional RF circuit designs as quad-ring and dual-ring topology, to develop the compact sensing modulator. We also contacted our simulation data to the sensitivity analysis to compare the performance of such different circuit topologies and find the optimum performance criteria to enhance the circuit design.

Chapter 6 is the development of harmonic sensing concept toward the systematic performances. Here we investigate the potential applications on harmonic sensing systems such as all-graphene compact transponder sensor based on a graphene planar monopole antenna and the dual-band microstrip antenna. Finally, we conclude that the system can efficiently operate in a near-field and far-field communications which benefits low-power and zero-bias as well as low-noise and clutter-free applications.

II. 2D-MATERIALS RADIO FREQUENCY APPLICATIONS

During at least recent 15 decades, layered materials have been studied in its bulk circumstance while in the very recent decades the scientists have found that the novel potential can be emerged with thinning it to the physical limits. This physical limit refers to the confinement of charge and heat transport in a perpendicular direction to a two-dimensional (2D) plane [137]. The most considered 2D-material is graphene comprising the single-atom carbon layer arranged in a honeycomb lattice that first time in 2004 was obtained from its van der Waals solid [100]. Besides its broad extraordinary characteristics such as flexibility despite mechanically strong, optically transparent, and its conductivity dependency to the chemical and electrostatic gating, the unique gapless energy band diagram which provides an ambipolar carrier transport with ultra-high mobility makes it very interesting material to generate some unique electronic devices for high-frequency applications. Graphene field-effect transistor (GFET) is one of the well-known graphene-based electronic devices which provides numerous possibilities to achieve interesting radio-frequency (RF) and analog platform through its symmetric "V-shape" drain current-gate voltage characteristic. During a decade, the simplest high frequency application as frequency multiplier, multiplexer, frequency doubler, diplexer, and modulator have been demonstrated using GFETs to benefit compact low power RF circuits proper for sensing and internet of things (IoTs) approaches [115]-[118], [121], [129],[97], [138]-[144],[117]. In the other hand, since the gapless band diagram can be a hurdler for switching applications, where a large on-off ratio is in the demand, the scientists have also utilized some other 2D-material for high-frequency electronic devices known as transition-metal dichalcogenide (TMD) family, to benefit the low-power switching applications due to its

adjustable bandgap. However, there are several trade-offs between high-frequency applications using graphene and TMDs, such as mobility, cut-off and maximum frequency, transconductance, and effective carrier velocity, which may result in the design criteria based on the intended application. In addition to the TMDs which provide a wide range of electrical, optical, chemical, thermal and mechanical properties thanks to the variety of elements as well as the layer-dependency that result processing indirect bandgap for bulk crystals to direct-bandgap semiconductors in the single-layer limit, graphene analogues are another important type of 2D-material, which includes hexagonal boron nitride (hBN) with a large bandgap up to 6 eV, anisotropic black phosphorus (BP), and borophene [145]. The detailed comparison and its high-frequency characteristics will be discussed later in this chapter.

From RF and high-frequency circuit design point of view, the 2D-material based electronic devices provide the capability to generate an ultra-low profile, ultra-low cost, and low power circuit components, reaching to a transit frequency up to several hundreds of gigahertz (GHz) [120],[146],[147]. Most of the functional circuits such as modulator, mixer, multiplier, and amplifier, generally are utilizing active devices as transistors; hence achieving to the design and fabrication technology on 2D-material based active device and circuits, incorporated with nanotechnology and microsystem engineering, has had a revolutionary impact on RF and microwave compact systems. Moreover, the combination of these high-frequency circuit functions with the other advantageous properties of 2D-materials aroused from the innate thinness, as the flexibility, transparency, light-weight, and chemical gating, renders lucrative systems for the new generation of IoTs communications in 4G and 5G infrastructures. For instant, the typical sensor network can

be made by the separate and independent modules as sensor, modulator, and memory that are necessary components as a graphene chemical sensor which need to be combined with a silicon-based modulator to make it compatible with wireless radio frequency (RF) operation [148],[149]. However, in the case of nanosensors based on nanomaterials and nanostructures, their small sizes and heterogeneous features compared with conventional solid-state electronic devices could make their integration particularly challenging. Although integrating nanomaterial sensors with commercial silicon-based modulation interfaces, needs complicated post-transfer processes that result in a high-cost and non-compatible nodal structure and therefore limits the applicability of nanomaterial sensors for the internet of nano-things (IoNT), monolithic 2D-material based components paradigm can enable virtually simultaneous in situ chemical sensing and signal modulation, thereby significantly reducing the integration complexity and cost, which is of great interest for ubiquitous sensor network applications [121].

In this chapter, we first review two-dimensional transistors in RF and microwave applications; following by graphene transistor characteristics, modeling, and its potential to operate as a functional circuit component in RF and microwave systems. Afterward, we present an overview of the alternative 2D-materials for graphene analogues circuit components and its technical trade-off for the same high-frequency applications.

2.1. Radio-frequency and microwave two-dimensional transistors

This part is a review on Ref. [150]-[188]

The Transistors, as a major part of analog and digital circuits, have experienced a supreme grow in operation frequency, gain, and its footprint. Although reducing the transistor size provides advancement of high-frequency performance due to decreasing electron transit time and consequently, the gate capacitance, dwindle the vertical size of semiconductor transistors has limited its frequency response enhancement [150]. Hence the conventional semiconductors have been replaced with nanoscale materials to overcome this limit. One-dimensional (1D) nanostructures such as Silicon nanowires (SiNWs) and Carbon nanotube (CNT) have been the first candidate to operate as the channel of field-effect transistors (FETs) that potentially has been expected to increase the range of the high-frequency performance up to terahertz (THz) due to the ballistic transport of one-dimensional (1D) conductor and its consequent highly linear relation between drain current and gate-source voltage [151]. However, in the practical experiment, the operation frequency was limited to 23 GHz due to a high impedance created at the ohmic contact with the small size CNT channel [152]. Replacing CNT with graphene was a solution for reducing the impedance mismatch where the 2D-nanomaterials generally have conformal and intimate contact with metal electrodes compare with the 1D-channel, in addition to its larger lateral size which improves the control on the channel structure [150]. Moreover, the 2D nature of graphene results in another distinct advantage, where the drive current of a graphene device can be easily scaled up by increasing the device channel width. This width scaling capability of graphene is of great importance for realizing high-frequency graphene devices with adequate drive current for large circuits and associated measurements [153].

In the other hand, although the gap-less band-diagram of graphene causes small on-off current ratio (that is not necessary for all the circuits), high carrier mobility ($2.5*10^5$ cm^2/Vs) and carrier velocity that leading to a large transconductance g_m and the consequent high cut-off frequency f_T, make it sufficient for high-frequency performance. Nevertheless, owing to the gapless graphene channel, achieving saturation is relatively difficult and so $f_{max} < f_T$ that consequently results in a large drain conductance g_{ds} which limits the voltage gain $A_v = g_m / g_{ds}$; since for some RF applications f_{max} (the frequency at which the power gain equals unity) is in the same importance of f_T (the frequency at which the current gain equals unity), it can limit GFETs high-frequency performances. Although f_{max} for GFETs has been improved up to 70 GHz utilizing some technique on FET design, recently some other 2D-materials known as transition-metal dichalcogenide (TMD) family show even extra capability for high-frequency performances which will be discussed in detail later in this chapter.

2.2. Graphene field-effect transistors

Graphene research has been accelerated exponentially in high-frequency electronics because it has extremely high carrier mobility. The state-of-the-art graphene field-effect transistor (GFET) already exhibits a cutoff frequency (f_T) up to 300 GHz, which is much higher than conventional silicon-based transistors. Besides, its unique symmetric "V" shape drains current gate voltage characteristic, triggered by the ambipolar charge transports in the gapless graphene, makes GFET the simplest possible frequency doubler that can operate at very high-frequency range (up to the tens of GHz). On the basis of this unique property, special modulation functions, such as full-wave rectification, frequency

mixing, amplitude modulation (AM), frequency modulation (FM), and phase modulation (PM), can be directly achieved with a single graphene device, which is not possible for conventional semiconductor devices.

Even though the first graphene transistor was reported in 2004 with the extensive discussion regarding its electric field effect, the IBM group comprehensively studied the high-frequency performance of graphene transistors with variable gate lengths in 2009. The small-signal current gain of graphene transistors derived from S-parameter measurement shows a dependency to *1/f*, while the resulting f_T value exhibits a strong adherence to drain and gate voltage, as well as the dc transconductance g_m. In particular, the cutoff frequency inversely related to the square of the gate length ($\sim 1/L^2$), has reached as high as 26 GHz with a gate length of 150 nm, in its primary study. Hereafter, the high-frequency performance began to draw attention and a growing number of studies have been reported to further increase the cutoff frequency of GFET. In early 2010, a graphene MOSFET with a 240 nm gate showing an f_T of 100 GHz has been presented, soon followed by a 144 nm gate graphene transistor with f_T approaching 300 GHz. Afterward, in 2012, a GFET with a 40-nm-long gate showing 350 GHz f_T and a 67 nm gate GFET with a cutoff frequency 427 GHz has been reported. The high-frequency response of the initial devices with limited cutoff frequency up to several gigahertz is primarily restricted by two factors: First, the dielectric integration process uses an oxidative functionalization layer, resulting in a drastic degradation of the electronic properties of graphene with carrier mobility as low as 400 cm^2/Vs. Second, in these initial devices, a large gap exists between source/gate and/or gate/drain electrodes, in which the graphene is not effectively modulated by the gate but functions as a series access resistance.

To overcome the limitation of graphene transistors and improve their RF performance, various gating configurations and different dielectric/substrate materials have been comprehensively studied. For the gating configurations, dual gate and self-alignment gate graphene transistor are two common alternatives. Contrary to the first top gate GFET, dual gate structure consists of both local top-gate and global back-gate has been reported, in which the access resistance of the graphene transistor is modulated by the back-gate through electrostatic doping. By varying the back-gate voltage, the access resistance can be significantly reduced by more than a half, contributing to a four-fold increase of the transconductance g_m. As a result, an intrinsic cutoff frequency of 50 GHz is achieved in this 350 nm gate graphene transistor. Another viable gating scenario to mitigate the access resistance is through optimum alignment of the source/drain and the gate electrodes. In this technique, L. Liao's group developed a self-aligned approach, which utilized a metal/oxide Co_2Si/Al_2O_3 core/shell nanowire as the top gate and integrated it on graphene by a physical assembly process at room temperature, in which successfully demonstrating a graphene transistor with cutoff frequency up to 300 GHz. Further, in order to eliminate the imperfect contact interface with graphene due to the diamond-like cross-section of this $C_{o2}S_i/Al_2O_3$ core/shell nanowire, they proposed 100 nm channel long GaN nanowire with a triangular cross-section and a flat side surface as the self-aligned gate, which exhibits a scaled transconductance exceeding 2 mS/μm and a projected intrinsic $f_{T=}$840 GHz at V_{ds} = 1 V.

On the other hand, the interfaces existing in graphene/substrate and graphene/top-gate dielectric insulator, that are two dominant sources of scattering in graphene devices, resulting in the significant degradation of electrical transport due to the two-dimensional

nature of graphene. In 2011, Balandin's group mitigated the scattering effect associated with trapped charges through the usage of DLC film as the GFET substrate, which is advantageous because of the high phonon energy in sp^3- hybridized carbon (165 meV) and it's nonpolar, as well as the non-hydrophilic nature. Another desirable substrate is silicon carbide (SiC), which not only possesses a high intrinsic phonon energy 116 meV, but also high-quality graphene sheets can be directly grown on its surface by epitaxy. In these suitable substrate alternatives, the intrinsic cutoff frequency of graphene transistors can reach up to 300 GHz, based on both wafer-scale CVD grown graphene and epitaxial graphene on SiC. In summary, to further alleviate the scattering effect between the graphene and the dielectric surface during the integration process, miscellaneous types of oxidative functionalization layer, such as Al_2O_3, HFO, Y_2O_3, and Boron-Nitride, have also been studied extensively to reach the cutoff frequency up to 400 GHz.

2.3. TMD-based transistors

The general formula for TMD materials is in a form of MX_2 where M represents transition metal (e.g. Mo, W, Nb, Ta, Ti, or Re) covalently bonded with X atoms (X= Se, S, or Te). Molybdenum disulfide (MoS_2) is an interesting semiconductor from this family where its bandgap dependency on the thickness makes it an appropriate replacement for the graphene channel in FET. MoS_2 involves planes held together by van der Waals interactions, each plane comprising covalently bonded S-Mo-S atoms closely packed in a hexagonal arrangement. The weak interlayer interactions compare with strong intralayer bonding for MoS_2 make it feasible to synthesis a layer from bulk crystalline. Consequently, the bandgap of this semiconductor is adjustable from indirect bandgap for bulk E_g=1.29 eV to the direct bandgap of the monolayer (thickness of 0.65 nm) E_g=1.8 eV. Albeit the

mobility for MoS_2 (170 cm^2/Vs for few layers and 102 cm^2/Vs for monolayer at room temperature) is not as large as graphene ($2.5*10^5$ cm^2/Vs) but still is higher than metal oxide thin-film transistors (TFTs); the effective carrier velocity (v_{eff}) of MoS_2 transistor ($2.8*10^6$ cm/s for few layers and $1.1*10^6$ cm/s for monolayer) in combination with the relatively large bandgap makes it a proper candidate for low-power RF applications. On the other hand, an extraordinary enhancement of the current on/off ratio is achieved (10^8 for MoS_2) compare with the graphene transistor (<10), which is suitable for high-speed switching. Further, its natural bandgap creates a voltage gain larger than 10 as well as high intrinsic transconductance and drain-source current saturation, which all benefit the high-frequency applications. The most MoS_2 transistors show n-type behavior, while for p-n junction devices some methods such as electric double layer gating or p-doped plasma treatment have been used for this material. Simultaneously, p-type behavior has been observed in another TMD, tungsten diselenide (WSe_2) that even viable to show ambipolar carrier transport whenever grown as monolayers. To increase the high frequency capability, black phosphorus (BP) thin film has been also used due to the higher mobility (650 cm^2/Vs for crystal structure and 1000 cm^2/Vs for bulk at room temperature), however attracted less interest because of the low bandgap (0.3 eV for bulk) and difficulty of controlling the material quality. A comparison of these 2D material-based devices is shown in Table 1. In addition, a comparison between TMD-based transistor characterization with a nonconventional FET (monolayer MoS_2 transistors and $In_{0.7}Ga0_{.3}As$ Quantum-Well FET) shows the extraordinary on/off ratio enhancement for low power applications, as shown in Table 2. Next, we are introducing some high-frequency and RF applications based on these 2D-material devices.

2D material	Crystal class	Electronic structure	Bandgap (eV)*	Mobility ($cm^2 V^{-1} s^{-1}$)
Graphene	Hexagonal	Semimetal	NA	2,000–5,000 (supported; experimental values)[130] 200,000 (freestanding; experimental value)[131]
TMDCs (MoS_2)	Hexagonal	Semiconductor	From 1.29 for bulk (indirect) to 1.96 for monolayer (direct)[132]	<320 for electrons, <270 for holes (theoretical values)[133]
Phosphorene	Orthorhombic	Semiconductor	From 0.3 for bulk (direct) to 1.75 for monolayer (direct)	<10,000–26,000 (monolayer; theoretical values) 400–4,000 (few-layer; experimental values)
h-BN	Hexagonal	Insulator	5.971 (direct)[134]	–

h-BN, hexagonal boron nitride; NA, not available; TMDCs, transition metal dichalcogenides. *Bandgap values are all from experimental sources.

Table 1: Properties of phosphorene compared with those of other 2D materials [169]

	L_{ch} (nm)	EOT (Å)	I_{max} (mA/μm)	peak g_m (mS/μm)	max I_{ON}/I_{OFF}	min SS (mV/decade)
$In_{0.7}Ga_{0.3}As$ quantum-well FET (ref 22)	75	22	0.49	1.75	312	85
monolayer MoS_2 FET	75	22	0.19	0.3	1.4×10^7	60

Table 2: Comparison of key device performance parameters of $In_{0.7}Ga_{0.3}As$ quantum-well FET and monolayer mos_2 FET of identical EOT and channel length [173]

III. GRAPHENE-BASED HARMONIC SENSORS

Parts of this chapter have been presented in [17],[121],[215].

Copyright © AIP 2016, Springer 2016, IEEE 2017

Graphene field-effect transistors (GFET) are emerging as promising frequency multipliers, thanks to their unique "V-shape" drain current-gate voltage characteristic that is possible only with the ambipolar carrier transport in graphene [117]. In addition, the ultra-high carrier mobility of graphene may lead to a cutoff frequency f_T up to 300 GHz [114]. Very recently, graphene harmonic sensors, combining the frequency multiplication and chemical sensing functions of GFETs, have been reported for PH and chemical sensing [17],[97]. These harmonic sensors can be free from background electromagnetic interferences, clutters, and backscattered echoes, as they receive a RF signal at the fundamental frequency and re-transmit a second harmonic. However, simultaneous detection of two or more PH/gas/molecular/chemical agents remains challenging for such GFET-based wireless sensors or conventional CMOS wireless sensors.

3.1. Graphene Field Effect Transistor Harmonic Sensor

Advanced nanostructures such as two-dimensional carbon nanomaterials, namely, graphene [100], with their single-molecule-level sensitivity in chemical sensors and biosensors [99],[105]-[108], may establish a foundation for future ubiquitous micro-/nanosensor networks [189],[190]. In general, the sensor, modulator, and memory that are necessary components of a sensor network are separate and independent modules [148],[149]. For example, a graphene chemical sensor would need to be combined with a

silicon-based modulator to make it compatible with wireless radio frequency (RF) operation for data synchronization in internet-of-things (IoTs). However, in the case of nanosensors [105]-[108] based on nanomaterials and nanostructures, their small sizes and heterogeneous features compared with conventional solid-state electronic devices could make their integration particularly challenging [191],[192]. To integrate nanomaterial sensors with commercial silicon-based modulation interfaces, complicated post-transfer processes must be performed [192]; this results in a high-cost and non-compatible nodal structure and therefore limits the applicability of nanomaterial sensors for the internet of nano-things (IoNT) [193]. It has recently been reported that graphene field-effect transistors (GFETs) can exhibit not only ultrahigh mobility but also interesting gapless electron-hole spectra and ambipolar transport properties which lead to a nonlinear effect in the control of the gate voltage with respect to the drain current. On the basis of this unique property, special modulation functions, such as full-wave rectification, frequency mixing, amplitude modulation (AM), frequency modulation (FM), and phase modulation (PM), can be directly achieved with a single graphene device, which is not possible for conventional semiconductor devices [117],[116],[129],[144],[194]. Here we propose a different modulation mechanism utilizing chemical gating, instead of the application of an electrical signal, to directly modulate the input carrier signal by means of the chemical dopants (for example, gases or molecular substances) to which a GFET is exposed. This monolithic all-graphene paradigm can enable virtually simultaneous in situ chemical sensing and signal modulation, thereby significantly reducing the integration complexity and cost, which is of great interest for ubiquitous sensor network applications. For most graphene sensor applications, the sensor output signal, in information theory, is one-dimensional (1D), in

terms of either direct current (DC) or electrical resistance. This 1D spectrum offers limited information processing, storing, and distributing capabilities [99],[105]-[108], [195]-[198] because of the low-signal dimensionality. One advantage of the proposed chemically modulated sensing device, compared with other nanomaterial sensors, resides in its two-dimensional (2D) output signal, which provides information through both the amplitude and frequency of an RF signal. Very recently, Lee et al. have demonstrated that electrically gated modulation on graphene exhibits a transition from a fundamental input tone to a second-harmonic output tone [129], which enables AM to FM functions using a single device. Here we show that this signal transition is not abrupt and that the fundamental and second-harmonic tones instead coexist, with gradually varying strengths depending on the potential level of the graphene, which can be modulated by means of a chemical (or electrical) gating effect. In this scenario, mixed AM/FM modulation can be achieved and the amplitude responses at both frequencies constitute a 2D output signal, thereby improving the overall reliability and the tolerance to environmental noise and interference.

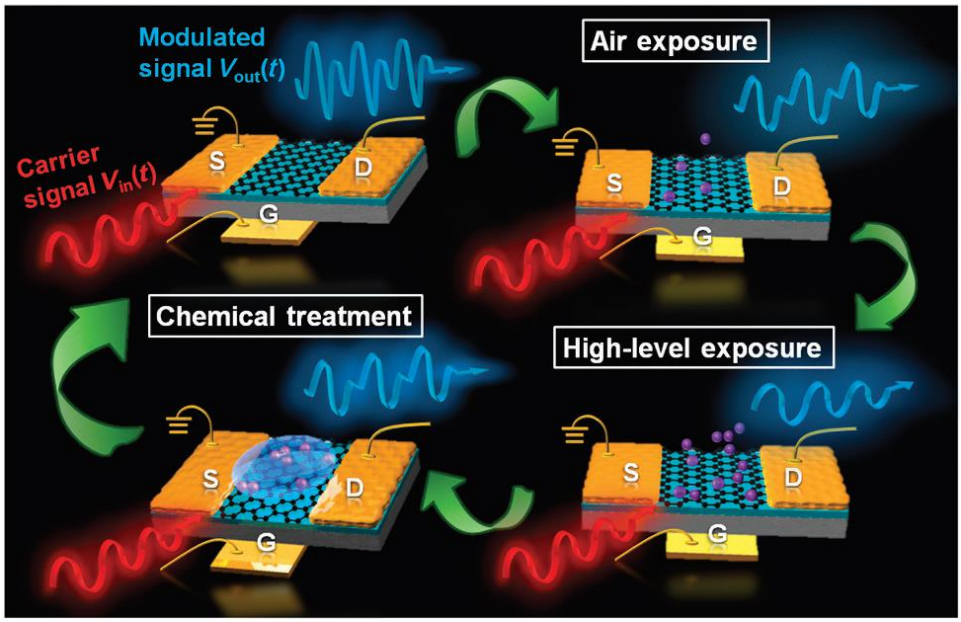

Figure 3.1. Single GFET harmonic sensor overview

Conceptual illustration of the chemical gating modulation of a single graphene device, in which a high-frequency input carrier signal is applied at the back gate without any DC gate bias and the modulated output at the drain varies throughout a modulation cycle consisting of alternating phases of gas exposure and wet chemical treatment [121].

Figure 3.1 illustrates the basic operation principle of the proposed device: the carrier signal is a single-tone sinusoidal (RF) wave applied at the back gate of a GFET, which is compatible with wireless or high-speed wireline communication systems. Under a given drain bias, the output drain current waveform consists of both fundamental and second-harmonic frequency components that are modulated by the chemical gating. The adsorption of p-type substances (for example, oxidizer-type gas molecules) will cause a gradual decrease in the amplitude of both tones at the output, with the second-harmonic

tone being the first to be fully suppressed. By contrast, the adsorption of n-type substances (for example, electron-donor-type chemical agents) will reverse the modulation of the output, restoring it to its original condition. These two phases essentially form a complete chemical modulation cycle, in which the two different phases, depending on the type of application, can be utilized for sensing and for the resetting (neutralization) of the sensor. For instance, in the sensing of oxidizing materials, materials with abundant electron donors may be used to reset the sensor. Similarly, in the sensing of electrondonating materials, an oxidizing material may serve as the reset agent. Figures 3.2 (a) and (b), respectively, show the circuit diagram for this graphene sensor and how the ambipolar transport behavior of the GFET, with a 'V-shaped' drain output–gate voltage characteristic curve, may lead to frequency doubling. From Figure 3.2(b), we note that the magnitude (modulation level) of the output signal at the doubled frequency is controlled by chemical gating, which involves a shift in V_{cnp}. When a single-tone input at a frequency f is applied to the gate with zero DC gate bias, the modulated output shows a visible change as V_{cnp} is altered through chemical gating: (1) if V_{cnp} is zero, then the drain output has a vanishing component at f and a strong component at 2f (gray curve); (2) if V_{cnp} is up-shifted above the critical point, then the signal component at f is amplified, whereas the 2f tone decreases (blue curve); (3) if V_{cnp} is far from the critical point, then the output signal begins to monotonically decrease, exhibiting drops at both f and 2f. With a large shift in V_{cnp}, the second-harmonic tone is completely suppressed, as the fundamental tone continues to decrease (red curve). A theoretical analysis of the mixed modulation output as a function of V_{cnp} is shown in Figure 3.2(c); the results were obtained using a compact, physics-based GFET model [199]. The best-signal linearity is observed at two critical conditions: the peaks in the fundamental-

tone curve (blue shaded region in Figure 3.2(c)) and the dips in the harmonic-tone curve (red shaded region in Figure 3.2(c); V_{cnp} = ± 1.4 V). This variation in nonlinearity is explained by the schematic diagram presented in Supplementary Figure S1a. The V_{cnp} of graphene can be shifted from positive to negative values, over a wide range, by means of exposure to p-/n-type dopants of different concentrations. As a result, there exists an ideal operating region in which both components are monotonic functions of V_{cnp}, as shown in the gray shaded region in Figure 3.2(c). In addition to the chemical-gating-induced V_{cnp} shift, the variation in carrier mobility also affects the output RF signal of the GFET. In fact, although the attachment of most chemical agents to graphene can affect its V_{cnp} [193], there is no material that shows a measurable impact on graphene's carrier mobility [194]. The results calculated for the two-tone output via 2D vector mapping clearly distinguish the traces of the V_{cnp} shifts at different mobility values. Our theoretical results indicate that the corresponding V_{cnp} can be retrieved from the 2D output even in the presence of variations in other parameters (for example, the carrier mobility), thereby demonstrating excellent robustness in sensing compared with conventional approaches involving the detection of only 1D outputs (for example, DC currents).

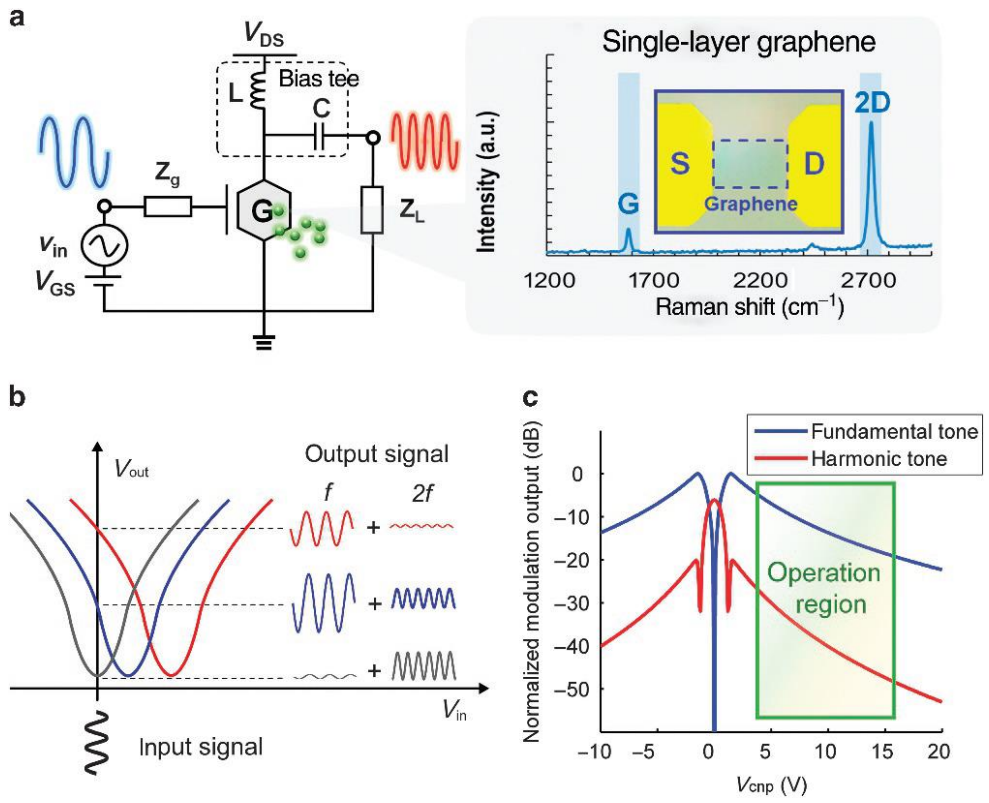

Figure 3.2. Principle of mixed modulation via the chemical gating of graphene.

(a) The circuit diagram; the inset shows a microscopic image of a GFET and the Raman spectrum of the CVD graphene channel. (b) Mechanism of mixed AM/FM GFET modulation; gray: if V_{cnp} is zero, then the output consists only of a strong harmonic tone; blue: when V_{cnp} shifts away from 0 V, a large fundamental tone is present and the harmonic tone decreases; red: when V_{cnp} shifts higher, both the fundamental tone and the harmonic tone decrease, but the harmonic tone decreases more rapidly. (c) Physics based modeling result (assuming electron-hole symmetry) for the two-dimensional modulation output (in terms of a normalized output voltage) depending on the V_{cnp} shift; a region is outlined in which both the fundamental and harmonic tones monotonically decrease, which can be used as the operation region for a demonstration of chemical modulation [121].

3.2. GFET Fabrication

For this experiment, the GFETs were fabricated using a shadow mask without any lithography step to preserve the pristine surface of the graphene. This is because in addition

to the H_2O/O_2 redox system, residues such as photoresist could also contribute to the formation of charge traps. The synthesized graphene was first transferred, using polymethyl methacrylate as a support, onto a SiO_2/Si substrate with a 285-nm thermal oxide layer as the dielectric to form a back-gate device structure. Raman spectroscopy with a 442-nm blue laser was used to confirm the quality of the graphene after transfer (see the inset of Figure 3.2(a)), revealing a G peak at 1582 cm^{-1} and a symmetric 2D band at 2695 cm^{-1} (bandwidth of ~ 32). Back-gated field-effect transistors were formed by means of the electron-beam evaporation of 2-nm Ti+48-nm Au metal contacts using a shadow mask to measure the electrical properties of the devices. The area of the metal contacts was 200 μm × 200 μm, which defined the graphene channel width; the devices were fabricated with various channel lengths of 25, 50, 100 and 200 μm. Further details regarding the graphene preparation [200]-[202] and device fabrication can be found in the previous work [203]. The intrinsic sensitivity of a graphene chemical sensor can be extremely high [108]. However, in this chapter, our focus was on demonstrating a novel multifunctional sensor/modulator module and its applicability for the sensing of time-varying chemical events rather than demonstrating the high intrinsic sensitivity of graphene-based devices.

3.3. Drift-Diffusion Transport Model of GFETs

For numerically investigate the GFET-based sensor circuits modeling in this project, we will employ the compact physics-based GFET model. In the drift-diffusion transport model, the drain-to-source current I_{DS} is described by [199]:

$$I_{\mathrm{DS}} = qW\left|Q_{\mathrm{tot}}(x)\right| v_{\mathrm{drift}}(x) = \frac{W}{L_{\mathrm{eff}}}\int_0^{V_{\mathrm{DS}}} \mu_{\mathrm{eff}}\left|Q_{\mathrm{tot}}\right| dV. \tag{1}$$

where W is the channel width, the effective channel length $L_{\mathrm{eff}} = L - \int_0^{V_{\mathrm{DS}}} 1/v_{\mathrm{sat}}\, dV$, accounting for the effect of saturation velocity, v_{drift} is the drift velocity, which, in a soft saturation model, is related to the channel electric field $F = -dV/dx$ as [199],[204]-[212]:

$$v_{\mathrm{drift}} = \frac{\mu F}{\left[1+\left(\mu_{\mathrm{eff}} F / v_{\mathrm{sat}}\right)^{\gamma}\right]^{1/\gamma}}, \tag{2}$$

where v_{sat} is the saturation velocity given by [199]:

$$v_{\mathrm{sat}} = v_{\mathrm{F}}\left(\frac{c_1}{1+c_2 (V_{\mathrm{ch}})^2} + c_3\right), \tag{3}$$

v_{F}=10^8 cm/s is the Fermi velocity in graphene, $c_1 = (v_{\mathrm{sat,max}} - v_{\mathrm{sat,min}})/v_{\mathrm{F}}$, $c_2 = [q/(5K_{\mathrm{B}}T)]^2$, $c_3 = v_{\mathrm{sat,min}}/v_{\mathrm{F}}$ [205],[206], K_B is the Boltzmann constant, T is temperature, and V_{ch} is the surface potential of graphene. The effective carrier mobility in Eq. (3) can be written as [207]-[209]:

$$\mu_{\mathrm{eff}} = \frac{n\mu_{\mathrm{n}} + n\mu_{\mathrm{p}} + n_{\mathrm{pud}}(\mu_n + \mu_p)/2}{n + n + n_{\mathrm{pud}}}\left(\frac{m}{m + V_{\mathrm{ch}}{}^2}\right), \tag{4}$$

where *n*, *p* are the electron and hole densities in a graphene channel, $\mu_{n,p}$ is the carrier low-field mobility (here $\mu_{n,p}$ = 1300 cm^2/(V·s)), n_{pud} is the residual charge due to electron-hole puddles (here $n_{pud} = 1.65\times10^{12}$ cm^{-2}), and *m* is the square of the reference channel potential as an empirical fitting parameter (here *m* = 1 V^2). The total mobile charge density Q_{tot} in graphene, involving the electron and hole sheet densities *n* and *p* [cm^{-2}] and the residual charge due to electron-hole puddles [208],[210], can be explicitly written as:

$$\begin{aligned} Q_{tot} &= Q_s + qn_{pud} \\ Q_s &= q\times\left[n_{imp} + \frac{\left(qV_{ch}\right)^2}{\pi\hbar^2 v_F^2} \right] \\ n_{pud} &= \frac{\Delta^2}{\pi\hbar^2 v_F^2} \end{aligned} \tag{5}$$

where Δ is the inhomogeneity of the electrostatic potential (here $\Delta = 150$ meV), n_{imp} is the sum of the intrinsic field-independent and impurity carrier concentrations (here $n_{imp} = 7\times10^{12}$ cm^{-2}), $\hbar$ is the reduced Planck constant, *q* is electric charge. The surface potential (V_{ch}) related to graphene's Fermi level E_F, can be expressed as a function of the gate-to-source voltage V_{GS} as [199]-[212]:

$$V_{ch}(x) = E_F(x)/q = \frac{C_{ox}}{C_{ox} + \alpha C_q}\left(V_{GS} - V_{cnp} - V(x)\right), \tag{6}$$

where α is the capacitance weighting factor [205] ($\alpha \approx 1$ when $q|V_{ch}| >> kT$, and $\alpha \approx 0.5$ when $q|V_{ch}| << kT$), the electrostatic capacitance C_{ox} is related to the permittivity

ε_{ox} and thickness t_{ox} of gate oxide as $C_{ox}=\varepsilon_{ox}/t_{ox}$, and the quantum capacitance C_q as a function of surface potential can be explicitly written as [213]:

$$C_q = -\partial(Q_s)/\partial V_{ch} = \frac{2q^2 K_B T}{\pi(\hbar v_F)^2} \ln\left[2\left(1+\cosh\frac{qV_{ch}}{K_B T}\right)\right]. \quad (7)$$

V_{cnp} is the back-gate voltage at the Dirac point, where the carrier sheet density becomes minimal for zero drain and source voltages. We note that V_{cnp} comprises the work function difference between the gate and the graphene channel (similar to the flatband voltage in conventional silicon transistors), interfacial charges at the graphene-oxide interfaces, and the charge neutrality point shift ΔV_{cnp} due to intentional or unintentional doping of graphene (e.g. chemical gating effects caused by gas, chemical or molecular agents). The channel voltage $V(x)$ in Eq. (6), as a function of the position in the channel, can be modeled using the gradual channel approximation: $V(x)=(x/L)V_{DS}$, which is zero at the source end (x = 0) and equal to the drain-to-source voltage V_{DS} at the drain end ($x = L$). The exact surface potential in graphene can be obtained by iteratively solving Eqs. (6) and (7). Once V_{ch} is calculated, the total charge density in the graphene channel can be obtained using Eq. (5), which, when substituted into Eq. (1) gives the drain current $I_{DS}(V_{DS},V_{GS})$. For a moderate input RF voltage, one may numerically calculate the small-signal transconductance of GFET $g_m = dI_{DS}/dV_{GS}\big|_{V_{DS}=const}$ and the drain conductance $g_{ds} = 1/r_{ds} = dI_{DS}/dV_{DS}\big|_{V_{GS}=const}$. The mobile channel charge, depending on V_{GS} and V_{DS}, can be modeled by the gate-to-source

capacitance C_{gs} and the gate-to-drain capacitance C_{gd}: $C_{gs} = -dQ_{ch}/dV_{GS}\big|_{V_{DS}=const}$, and $C_{ds} = -dQ_{ch}/dV_{DS}\big|_{V_{GS}=const}$, where the total net charge in the channel $Q_{ch} = W\int_0^L Q_{tot}dx$. The physics-driven GFET model was implemented in the circuit simulator [214].

3.4. RFID Sensor Based on Graphene Frequency Multiplier

Harmonic sensors are emerging as promising nonlinear wireless sensor that are free from background noises, clutters and backscattered echoes, as they receive a radio-frequency (RF) signal at the fundamental frequency and re-transmit a modulated RF signal at the orthogonal frequency [22], as illustrated in Fig. 3.3. However, compared to traditional backscatter-RF identification (RFID) sensors, a harmonic sensor usually increases cost and design complicity because it requires multiple antennas, sensors and actuators, and a frequency modulator that sometimes requires power source and energy harvesters [17]. Here, we propose a much simplified harmonic sensor design, which is based on a single module combining sensing and frequency modulation functions and a hybrid-fed antenna. Graphene field-effect transistor (GFET) has been proposed as an efficient frequency multiplier, thanks to its unique "V-shape" drain current-gate voltage characteristic resulting from ambipolar transports in graphene [117], as shown in Fig. 3.3(b), which is not found in any conventional semiconductor device. Besides, RF circuits based on graphene devices may have several unique advantages, such as optical transparency, flexibility, and high sensitivity to electrochemical reactions, since graphene is an atomically-thin, carbon-based material [108]. Figure 3.3(b) illustrates the chemically-sensitive frequency modulator based on a single back-gate GFET, in which chemical or

biological dopants (e.g. bacteria and infectious agents) bonded to the graphene may shift the charge neutral point V_{cnp} of device, thereby affecting the nonlinear conversion gain. Although sensor and frequency modulator can be combined in such device, it still requires a drain-to-source dc bias, implying the need for power module that could impede the practical use in ubiquitous wireless sensor systems.

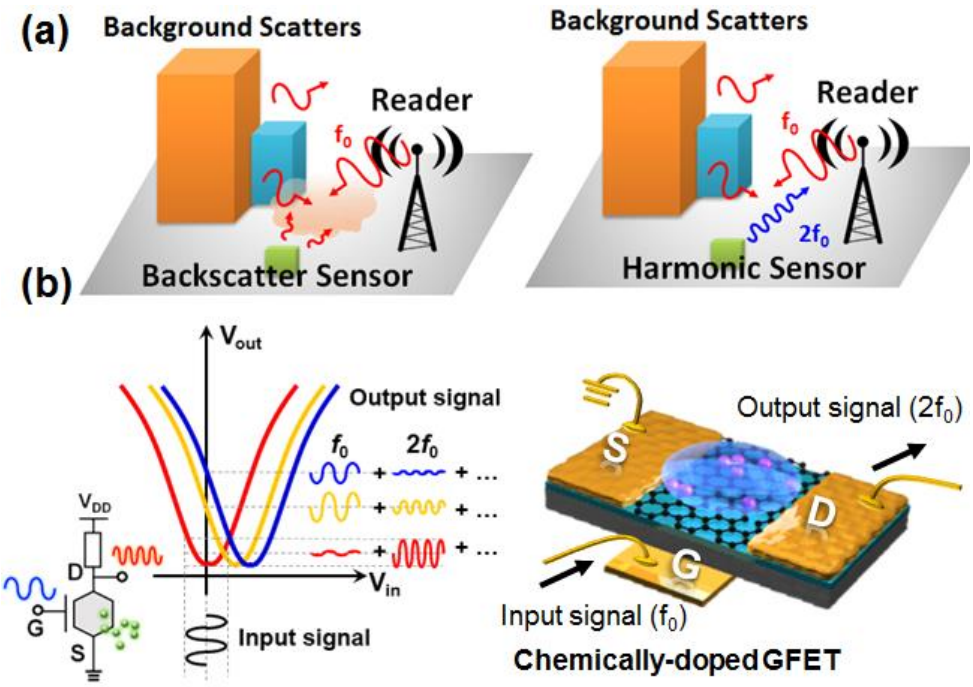

Figure 3.3. Single GFET harmonic RFID overview

(a) Schematics of backscatter-RFID sensor (left) and harmonic sensor (right). (b) A hybrid sensor-frequency modulator based on a graphene transistor [215].

In this section, we propose a new GFET-based RF circuit that realizes a fully-passive frequency modulator-sensor, as the key component of harmonic sensor for dynamically detecting PH/gas/molecular/chemical agents. We also investigate new antenna designs and wireless interrogation solutions, suited for miniature harmonic sensors.

Near-Field Graphene Harmonic Sensor

We have designed and characterized a near-field harmonic sensor, which consists of a GFET-based sensor-frequency modulator, two planar coils, and an AC-to-DC rectifier, as shown in Fig. 3.4(a). In this near-field harmonic sensing scheme, one microstrip-coil receives the incoming fundamental tone, with part of its power rectified to bias the GFET. After the second harmonic is generated, the second coil will re-transmit it to the reader. Here, the wireless interrogation is based on the inductive coupling and frequencies of input and targeted output signals are 125 KHz and 250 KHz, respectively. Fig. 3.4(b) shows the layout and photograph of such harmonic sensor; the inset of Fig. 3.4(b) shows the microscope image of the microfabricated GFET. In our experiments, chemical solutions with different PH values were dropped onto the graphene surface for observing changes in Vcnp and second-harmonic conversion gain of the GFET. The spectral analysis of this harmonic sensor at PH = 5 is presented in the inset of Fig. 3.4(c), showing a quite promising frequency-doubling effect. Fig. 3.4(c) summarizes (1) V_{cnp} of GFET and (2) magnitude of generated second harmonic as a function of PH values of liquid drop (chemical dopant). It is clearly evident that changes in PH value (chemical doping level) would linearly increase Vcnp of GFET, which accordingly varies the nonlinear conversion gain [117]. From Fig.

3.4(c), it is seen that the magnitude of output second harmonic can be quite sensitive to PH values. Due to the ambipolar transport in graphene, the magnitude of second-harmonic signal reaches its maximum at PH = 7 and decreases with increasing (decreasing) the PH value, corresponding to p-type (n-type) doping. As a result, by launching a RF input signal and reading the magnitude of the frequency-modulated output [Fig. 3.4(c)], one may be able to sensitively detect the existence and concentration of chemical dopants and charged impurities.

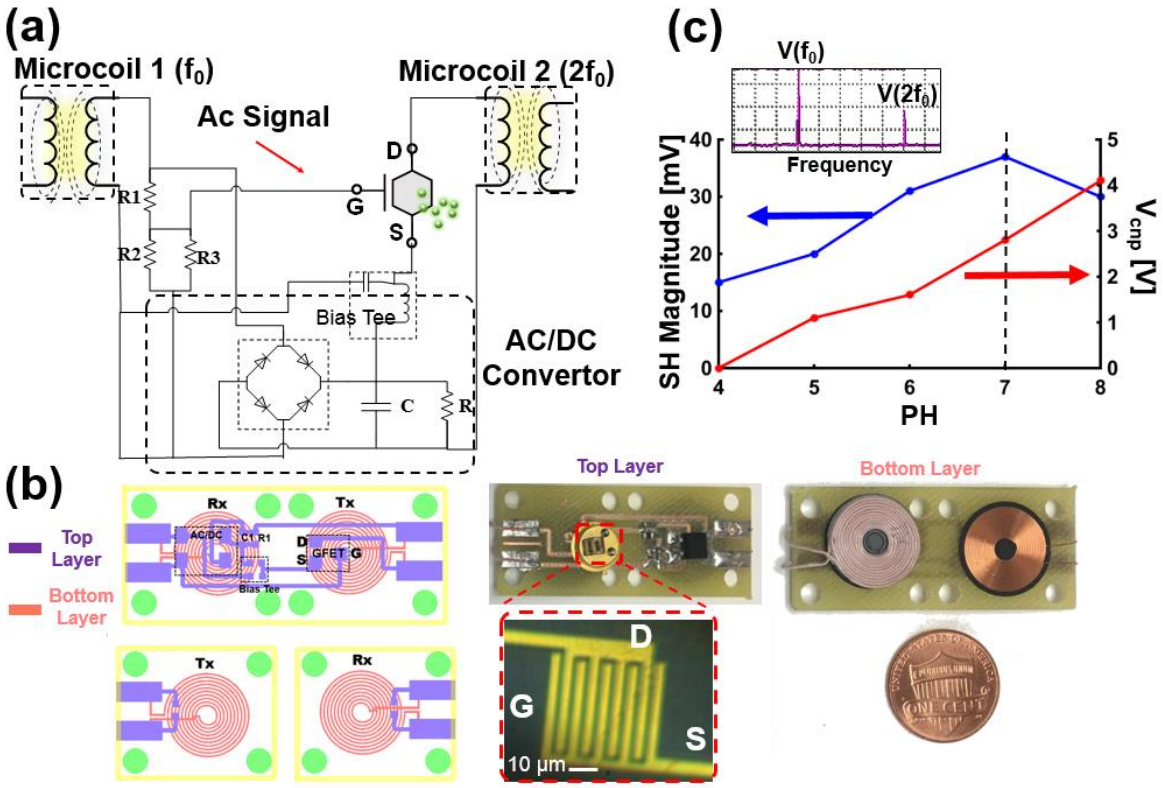

Figure 3.4. GFET-based PH sensor

(a) System diagram and (b) Architecture and photograph for the near-field harmonic sensor comprising a single GFET. (c) Magnitude of second harmonic V_{SH} (blue) and charge neutral point V_{cnp} (red) against the PH values of liquid drop on the graphene surface [215].

Furthermore, we have designed the layout of a monolithic integrated harmonic-sensor circuit based on the microfabrication process. Figure 3.5 shows the layout of the GFET frequency modulator/sensor circuit that may be manufactured within a compact size, much smaller than conventional harmonic sensor usually realized in on-board technologies.

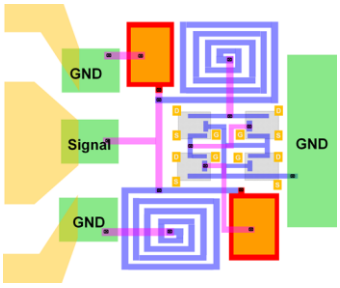

Figure 3.5. RFID circuit layout

A virtual image of the layout that may be manufactured using CMOS-compatible microelectronic technology[17].

IV. MULTI-FUNCTIONAL SENSING SYSTEMS

As mentioned earlier, the unique characteristic of GFETs as "V" shape symmetry drain current-gate voltage makes it a viable harmonic frequency generator. Considering one ideal back-GFET with an exact symmetry *I-V* characteristic as shown in Fig. 4.1(a), the fundamental signal at f_0 implying to the gate of GFET generates higher frequency harmonics (e.g. 2^{nd}, 3^{rd}, 4^{th}, and so on) at the drain output, where the second harmonic here is the dominate frequency if the DC offset of input be matched to the Dirac point of GFET. Thus, the harmonic sensor has been demonstrated based on the second harmonic modulation via a gating effect on the GFET Dirac point. In this paradigm, based on the single or multiple identical GFETs, either p-type or n-type doping effect on the graphene channel has the same effect on the generated higher harmonics due to the symmetric "V" shape *I-V* characteristic; then simultaneous detection of different agents and multiple doping effect seems impossible by using identical GFETs. However, inspired by the graphene-based frequency Tripler demonstrated by [234], here we propose a new technique based on the combination of non-identical GFETs capable to identify the level of more than one agent in a mixture medium. Figure 4.1(b) illustrates the working principle of higher harmonics generation based on the combination of two ideal GFETs by different charge natural points (V_{cnp}), where the fundamental frequency implied at the common gate of both GFET generates higher harmonics at the drain output; here with tuning the V_{cnp} of each GFET to combine two misaligned "V" shape *I-V* curve, a "W" shape drain current-gate voltage characteristic can be created which viable to demonstrate harmonic sensing applications for multi-agents sensing via the capability of generating and modulating number of harmonic frequencies. Hence, we expand the recent GFET based harmonic

sensor system performance to the new paradigm of multi-agent sensing application using the same physics-based drift-diffusion model for analytical study which has been quite matched with our recent experimental report [17][97]. The new circuit design of non-identical GFETs not only shows a unique behavior that benefits higher harmonics generation but also functionalizing graphene surface develops the sensor's selectivity area to a wider range of chemical or biological agents.

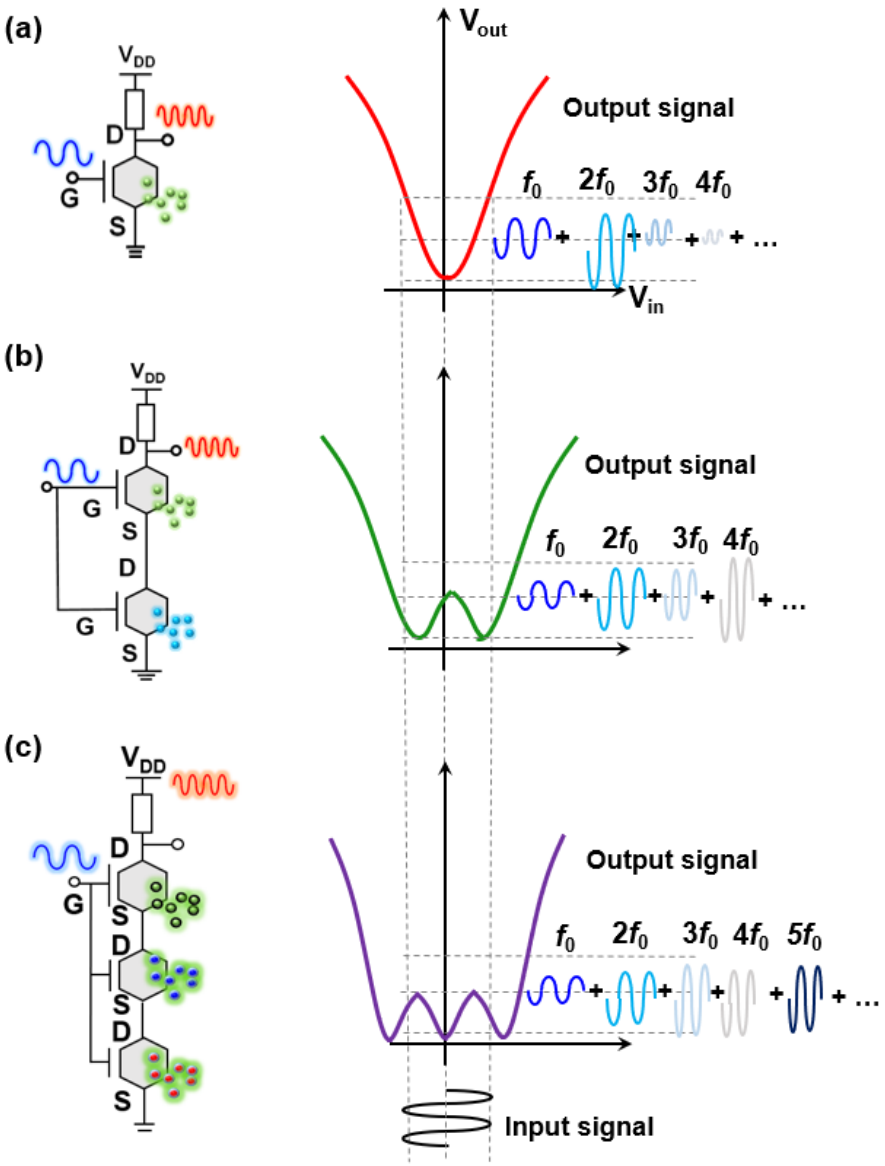

Figure 4.1. Multi-functional harmonic sensors overview

Schematic of GFET circuit design (left) and the equivalent Drain current-gate voltage characteristics (right) for (a) single, (b) double, and (c) triple agent harmonic sensors.

4.1. Multi-agents Harmonic Sensing Based on Functionalized GFETs

For multi-agent sensing purposes, a simple circuit design comprising two series non-identical GFETs with a common gate is proposed first, as shown schematically in Fig. 4.1(b). Since the charge natural point V_{cnp} is easily tunable with n-type or p-type graphene channel doping to drift the "V" shape *I-V* curve to the right or left respectively, we show that with combining two GFET by misaligned *I-V* curve a unified circuit by "W" shape *I-V* curve is obtained. On the other hand, by functionalizing each GFET, it is possible that any GFET is sensitive to one special agent which means the proposed circuit is viable to operate for multi-sensing approaches.

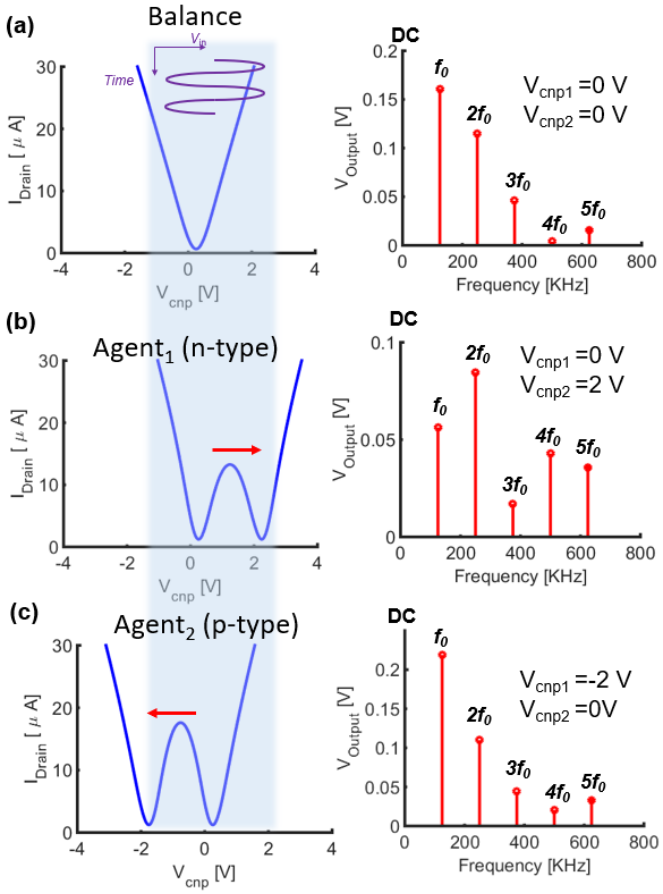

Figure 4.2. Double-agent harmonic sensor analysis

Simulation results for the circuit of double-agent RFID sensor in Fig. 4.1.(b). Drain current-gate voltage characteristics (left) and spectral analysis (right) for this double-agent sensor with (a) no chemical doping, (b) n-type chemical doping, and (c) p-type chemical doping.

In the first case, we consider two GFET with the same "V" shape *I-V* curve at the balanced condition which is functionalized to be sensitive to the n-type and p-type agents assigned to the first and second GFET respectively. Figure 4.2 shows the simulation results for unified circuit *I-V* curve and the corresponding output of fifth first frequency harmonics

amplitude for the three boundary conditions as the balanced, n-type agent binding ($agent_1$), and p-type agent binding ($agent_2$) effects; we assume that each agent at maximum binding level can shift the absolute value of V_{cnp} for 2 V. Here it is obvious that the combination of frequency harmonics for each condition is unique which means the effect of two distinct agents is monitored based on the proposed circuit. However, to continuously measuring each agent concentration, we need to extract the combination of harmonics amplitude modulation in the response to the all possible *I-V* curve shape via two agent mixture binding on the functionalized GFETs. Accordingly, the continuous contour of the four first harmonics conversion gain based on the continuous variation of V_{cnp1} and V_{cnp2} between 0 V to 2 V is shown in Fig. 4.3. Here, with comparing the variation of conversion gain for each frequency component under effect of the agent concentrations, although finding out the desired point of V_{cnp1} and V_{cnp2} combination by considering just small number of frequency component seems difficult, a mixture of components amplitude may show a unique output characteristic assigned to a special level of the material concentrations. Thus, using a data analysis technique to train the sensing system seems to be mandatory, while simultaneously monitoring and data analysis can lead to a feasible sensing module. Hence in section 4.2, we synthesize the proposed harmonic sensor by Machine Learning (ML) technique as an Artificial Neural Network (ANN) analysis to obtain the generalized harmonic sensing system.

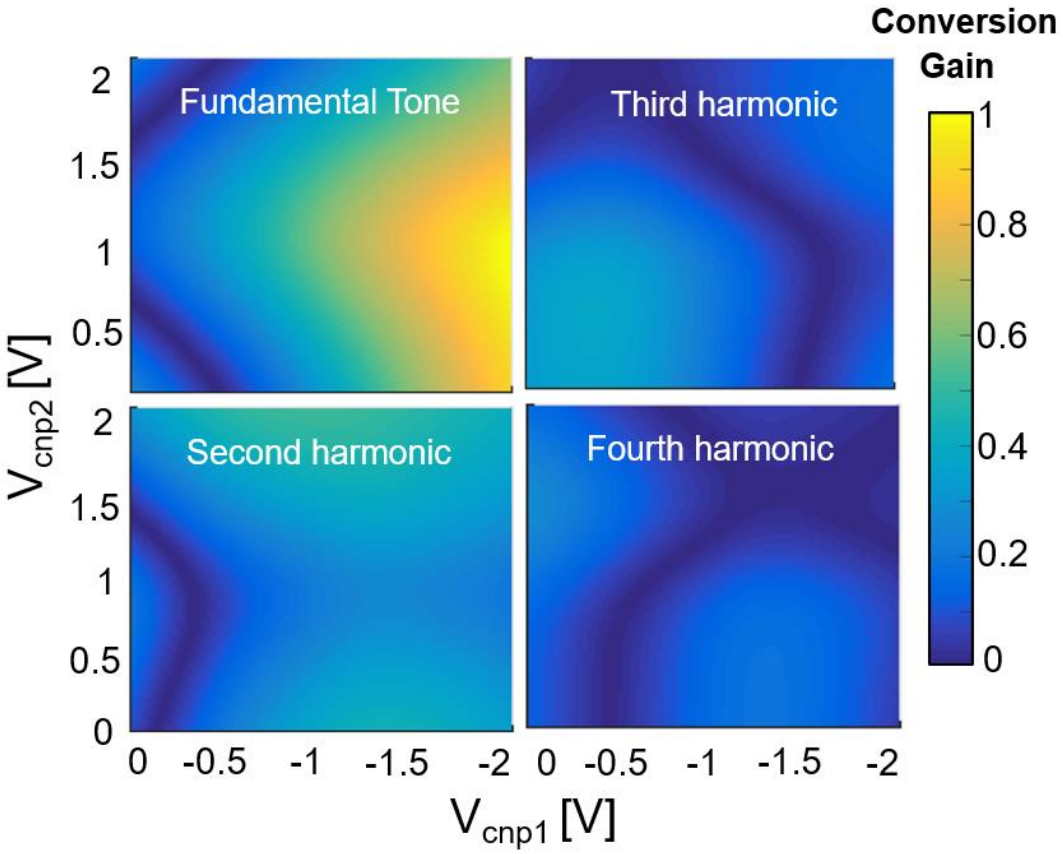

Figure 4.3. Harmonic frequencies conversion gain for dual-agent sensor

Contours of output signal as a function of V_{cnp1} and V_{cnp2} for the double-agent sensor in Fig. 4.1(b) and Fig. 4.2 at the (a) fundamental, (b) second-harmonic, (c) third-harmonic, and (d) fourth-harmonic frequency.

Before connecting our harmonic sensing system to the data analysis part, we need to investigate every possible functionality of the proposed GFET based circuit to obtain the maximum capability of the multi-agent harmonic sensors. Hence the second possible condition to measuring two agents with the same effect as p-type or n-type on the

functionalized GFET is illustrated in Fig. 4.4, where we assume two agents has an n-type effect on GFETs which shifts the Dirac point to the positive voltage. Here since the Dirac point shift is in the same direction then we need to distinguish the balance point for each GFET as shown in Fig. 4.4 (a); accordingly, the shift of Dirac point for each GFET causes a unique harmonic output due to a unique "W" shape *I*-*V* curve for each condition as shown in Fig. 4.4 (b) and (c) for bounded $agent_1$ and $agent_2$ respectively. Figure 4.5 shows that continues monitoring also is possible for this condition where the combination of the four first harmonic conversion gain is unique regarding two agent concentrations. Furthermore, this process is exactly the same when two n-type agents replaced with p-type where both the *I*-*V* curve shift to the negative voltage instead of positive, however, results in the same "W" shape *I*-*V* curve like Fig. 4.4.

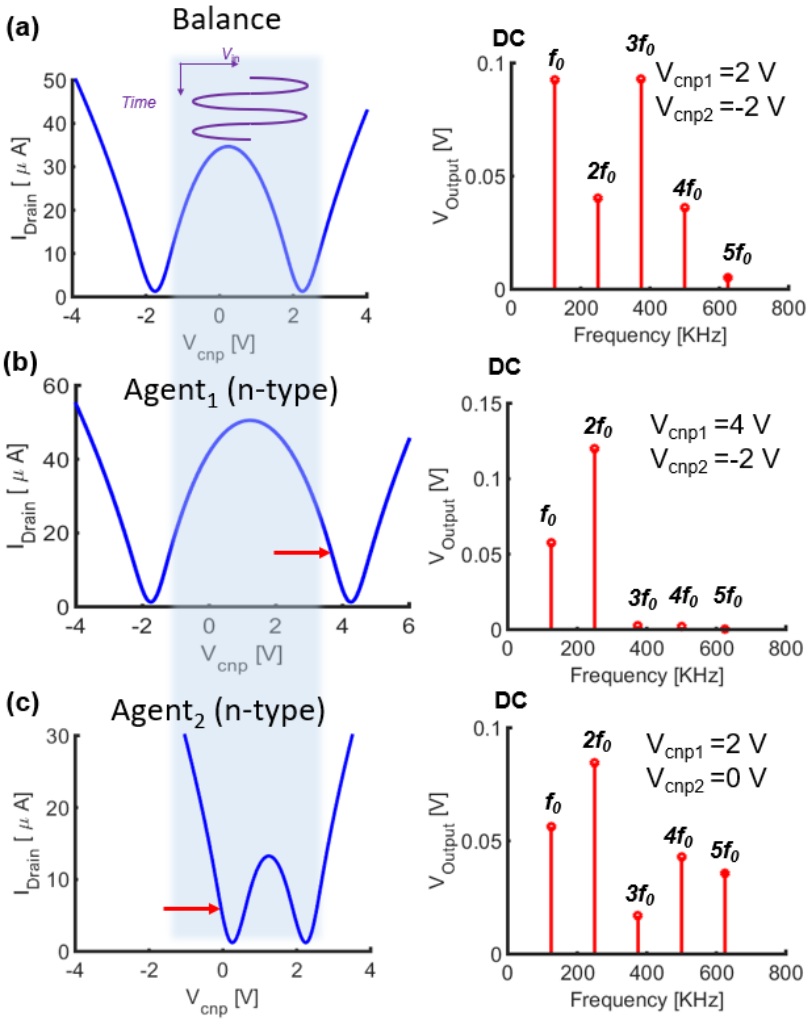

Figure 4.4. Double-agent harmonic sensor analysis (second type)

Simulation results for the circuit of double-agent RFID sensor in Fig. 4.1(b). Drain current-gate voltage characteristics (left) and spectral analysis (right) for this double-agent sensor with (a) no chemical doping, (b) first n-type chemical doping, and (c) second n-type chemical doping.

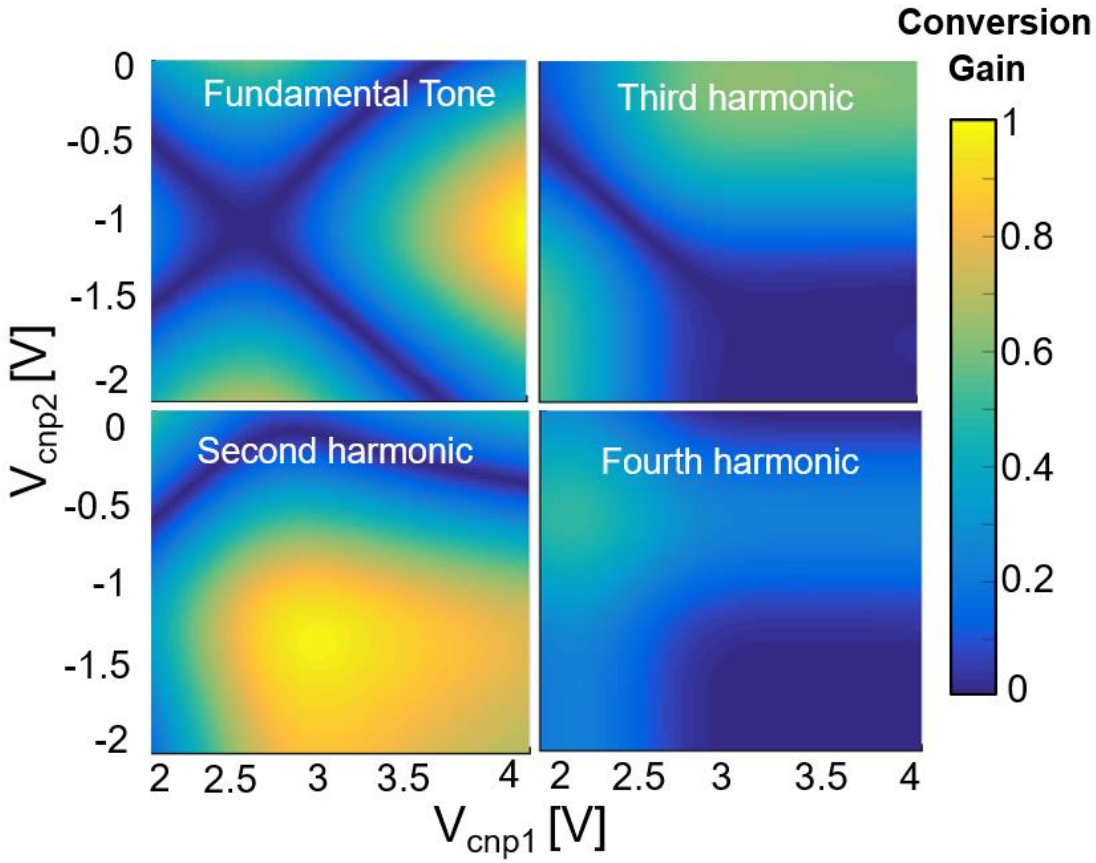

Figure 4.5. Harmonic frequencies conversion gain for dual-agent sensor (Second type)

Contours of output signal as a function of V_{cnp1} and V_{cnp2} for the double-agent sensor in Fig. 4.1(b) and Fig. 4.4 at the (a) fundamental, (b) second-harmonic, (c) third-harmonic, and (d) fourth-harmonic frequency.

Generally, we expand the GFET based harmonic sensing application from single-mode sensing to double mode sensing. However, in the next step, we try out the possibility of more agent measurement based on the harmonic sensing technique. Hence triple mode sensing is investigated where three functionalized GFETs may be viable to indicate the concentration of three different agents. For this purpose, there are more challenges to adjust the I-V curves of GFETs in the desired way to be applicable for generating unique

frequency components based on the variation of three agent concentrations. Thus, we assume a special condition for sensing a combination of three agents in which two of them have an n-type effect and another has a p-type effect on the functionalized GFETs; certainly, this process is the same for the condition that the environment includes two p-type and one n-type agent. Here we assume that the $GFET_1$ is functionalized to be sensitive to $agent_1$ as the p-type agent and $GFET_2$ and $GFET_3$ are sensitive to $agent_2$ and $agent_3$ respectively as the n-type agents. Accordingly, we can define four boundaries conditions for the triple sensing system as the balanced boundary in the absence of agents, and three boundaries in the presence of each agent; so, the sensing system performance is the areas between these four boundaries. To obtain a unique frequency components combination for each boundary, we first need to engineer the *I-V* curve combination for three GFETs at the balanced condition. After testing several combinations, we find that the best sensing approach is achieved when $GFET_1$ and $GFET_2$ be matched at the zero voltage while $GFET_3$ is adjusted to 4 V of V_{cnp}. Then with assuming that the maximum V_{cnp} variation for each agent is 2 V, four performance boundaries are simulated as shown in Fig. 4.6 (a) to (d). Here the *I-V* curve combination (left) and the consequent five first frequency components (right) show it is possible to have a unique harmonic response that benefits a triple harmonic sensor. However, still the same as single-mode and double mode sensing systems we need to connect this triple mode sensor to a neural network for reducing the complexity of extracted data as the frequency components which indicate the concentration of three agents as the level of V_{cnp}. In the next section, we illustrate the training system of our proposed multi-agent harmonic sensor using a machine learning technique and its achievable accuracy and feasibility.

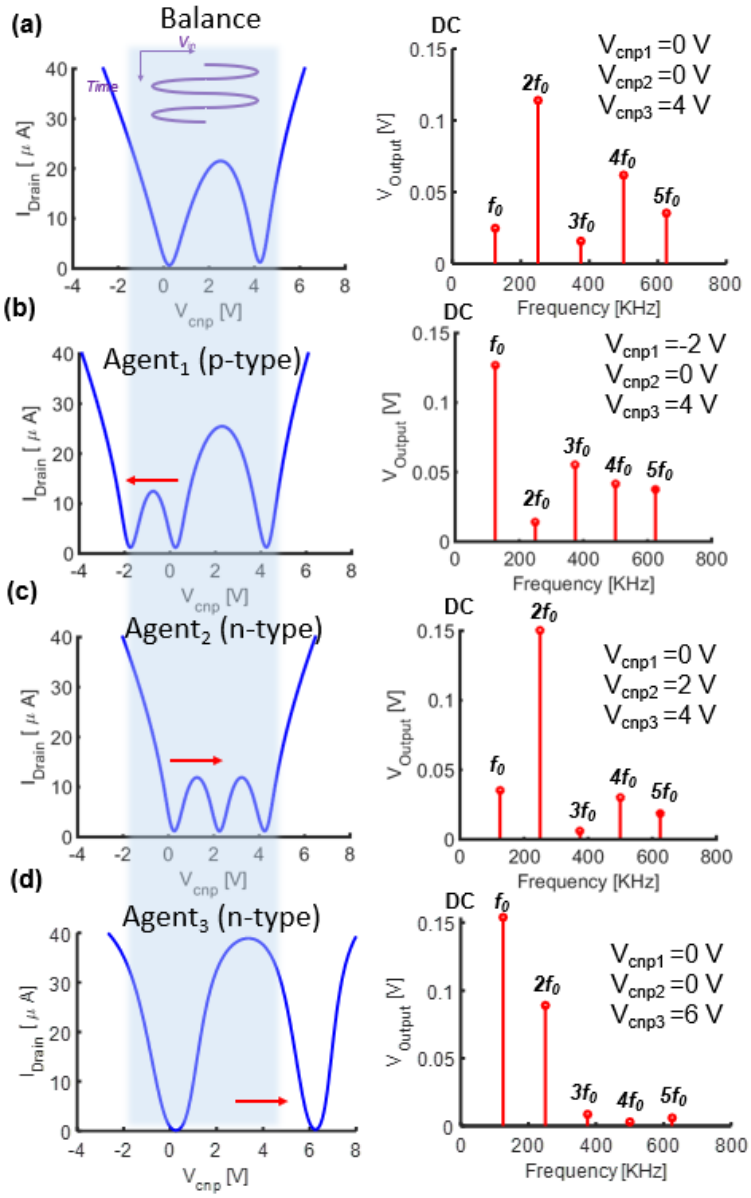

Figure 4.6. Triple-agent harmonic sensor analysis

Simulation results for the circuit of triple-agent RFID sensor in Fig. 4.1(c). Drain current-gate voltage characteristics (left) and spectral analysis (right) for this triple-agent sensor with (a) no chemical doping, (b) p-type chemical doping, (c) first n-type chemical doping, and (d) second n-type chemical doping

4.2. Neural Network Analysis Toward Multi-Agent Harmonic Sensor

Artificial intelligence (AI), also known as machine intelligence, is the intelligence exhibited by machines and software, in contrast to the natural intelligence demonstrated by humans and other animals. Artificial neural network (ANN) refers to a sort of Artificial Intelligence which intended to simulate the behavior of the human brain. An artificial neural network is a set of mathematical neurons that is inspired by the neural structure of the brain. Artificial intelligence techniques have been studied by many researchers in different fields and it is not surprising that ANNs have attracted attention in many application areas such as electrical engineering, biomedical application, machine vision, etc. Thus, here we are taking advantage of this technique to realize the application of our suggested multi-agent harmonic sensing system.

The main categories of networks are feedforward neural networks wherein the connection between the nodes does not form a loop and allows the signal to pass in only one direction, and recurrent neural networks which allow feedback. Among the most popular feedforward networks are multi-layer perceptron (MLP). Most MLP ANNs have three layers or more: an input layer, which is used to apply data to the network; an output layer, which is used to estimate an appropriate response(s) to the given input; and one or more intermediate layers, which are used to act as a collection of feature detectors. Figures 4.7(a) and 4.8(a) show a general architecture of a feedforward ANN which is used in this work, including one hidden layer. One-hidden-layer feedforward neural networks can fit any input-output relationship using enough neurons in the hidden layer. In general, simpler problems require fewer neurons, and more difficult problems require more neurons.

The ability of a neural network for information processing is obtained through a learning process that is done in the training phase. Learning is the adaptation of link weights so that the network can produce an approximate output(s). There are many different algorithms available for training a network and adjusting its weights. In this study, an artificial neural network is used to analyze multiple output harmonics for retrieving chemical properties of (bio-)chemical agents under detection. Since Extracting the exact value of two/three V_{cnp} based on four/five input harmonics seems not feasible, ANN is a useful tool for estimating its value.

The network is trained with the Levenberg-Marquardt backpropagation algorithm. The Bayesian regularization process is used to minimize the mean squared error (MSE) and adjust the synaptic weights to produce a network that could generalize well.

For training the double-agent harmonic sensors, the conversion gain of four harmonics (Fig. 4.3 and Fig. 4.5) is applied to the network as the inputs and the network estimated the value of V_{cnp1} and V_{cnp2} as the outputs. The network was tested by different numbers of neurons in the hidden layer and the optimum number (20 neurons) was used to minimize the error. Data are divided into three groups: training, validation, and testing set which are 70, 15, and 15 percent of data, respectively and chosen randomly. Figures 4.7 (b) and (c) show the testing data for n-type/p-type and n-type/n-type double agent harmonic sensors suggested in Fig. 4.3 and Fig. 4.5 respectively. Here 1000 epochs were considered for training the network and the best epoch is 456 and 167 to minimize the MSE for either n-type/p-type and n-type/n-type double agent harmonic sensors as shown in Fig. 4.7 (d) left and right respectively. Furthermore, an error histogram with 20 Bins (number of neurons) is shown in Fig. 4.7 (e) for both type of n-type/p-type and n-type/n-type double agents in

left and right respectively. Here the error analysis for the trained neural network shows a good performance of the suggested system due to very low MSE and low error values from the error histogram.

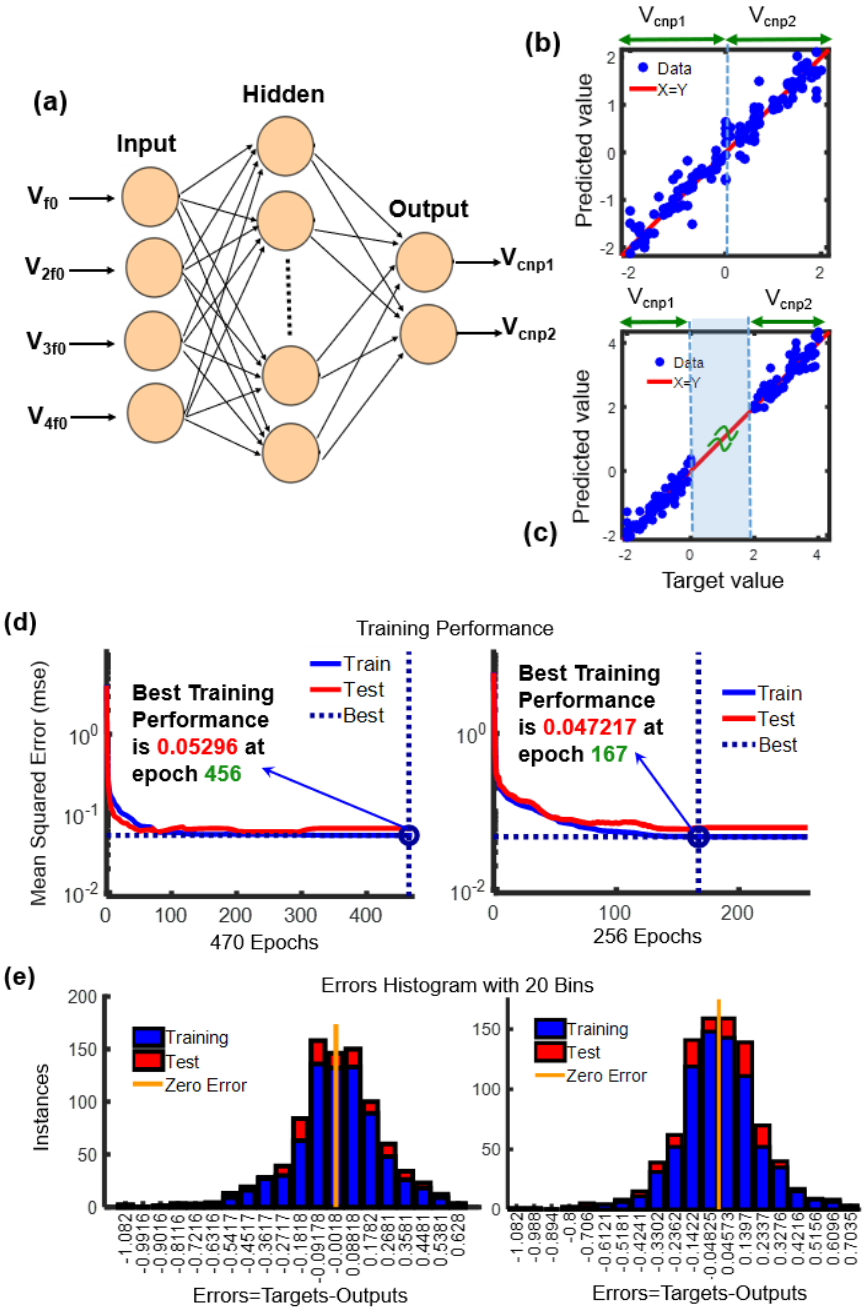

Figure 4.7. Machine learning for multi-functional harmonic sensor

(a) Inputs, hidden nodes, and outputs layers of the designed neural network (NN) for double agent sensor. (b) verification of the NN-predicted values of V_{cnp1} and V_{cnp2} with the exact V_{cnp1} and V_{cnp2} values in GFETs for n-type/p-type double agent sensor (Fig. 3). (c) is like (b), but for n-type/n-type double agent sensor (Fig. 5). (d) training, testing, and best achieved MSE value based on the number of epochs and (e) the error histogram with 20 neurons, for n-type/p-type double agent sensor (left) and n-type/n-type double agent sensor (right).

Finally, the same neural network is used for training the triple-agent harmonic sensor which suggested in Fig. 4.6. Here the only difference compare with double-agent sensor is the number of input and output; to indicate the concentration of three different material we have three different V_{cnp} as the output of our network which to obtain better performance of the ANN, the number of input is increased to five conversion gain of harmonic frequencies, as the architecture of the used feedforward ANN is shown in Fig. 4.8(a). The results of testing data for three estimations V_{cnp} using the neural network, mean squared error, and error histogram is shown in Fig. 4.8 (b), (c), and (d) respectively. For this type of sensor, with the same number of samples and epochs, the best epoch is 399 to minimize the MSE. Hence the best performance with minimum error is obtained too for this triple-agent harmonic sensor by taking advantage of the training neural network.

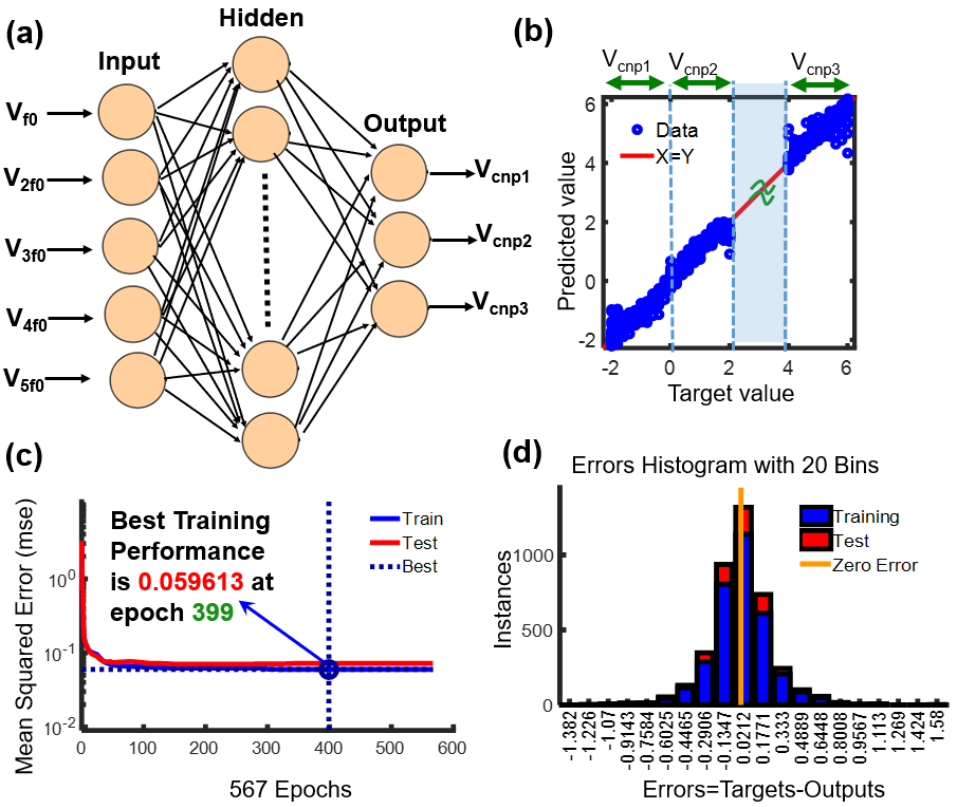

Figure 4.8. Neural network (NN) for triple agent sensor

(a) Inputs, hidden nodes, and outputs layers of the designed neural network (NN) for triple agent sensor. (b) verification of the NN-predicted values of $V_{cnp1,}$ $V_{cnp2,}$ and V_{cnp3} with the exact $V_{cnp1,}$ $V_{cnp2,}$ and V_{cnp3} values in GFETs for triple agent sensor (Fig. 4.6). (c) training, testing, and best achieved MSE value based on the number of epochs and (d) the error histogram with 20 neurons, for triple agent sensor.

V. SELF-POWERED GRAPHENE SENSING MODULATORS

Parts of this chapter have been presented in [17],[97].

Copyright © AIP 2016, IEEE 2017.

In the last chapters, we have proposed a simple but effective harmonic-sensing modulator using a single chemically gated graphene transistor, as shown in Fig. 5.1(a). When the chemical dopants (e.g., gases or molecules) bind to the graphene surface, the change in Dirac point (or charge neutral point V_{cnp}) position will shift the bias point and thus the nonlinear conversion gain, as illustrated in Fig. 5.1(b). This self-chemical gating effect, along with graphene ambipolar electrical property, can enable a dual sensing and frequency modulation function within a single common-source back-gate GFET:[121] the binding of chemical agents on the graphene surface can be known by launching an RF input signal and measuring the output second harmonic. The variation in the magnitude of second harmonic may serve as a good indicator of the concentration of chemical dopants. Figure 5.1(c) shows the magnitudes of output second harmonic (at 11.6GHz) compared with the input fundamental tone (at 5.8GHz) for a GFET with different V_{cnp} values. The circuit simulation was based on the physics-based drift-diffusion model with realistic physical properties of graphene that are summarized in the online supplementary material. From Fig. 5.1(c), it is seen that the magnitude of output second harmonic is highly sensitive to V_{cnp}. Although this prototyping device can already combine sensing and frequency modulation functions in a compact size, it, however, requires a relatively large drain-to-source dc bias to operate properly. For ubiquitous wireless sensor network applications,

passive (self-powered) sensor nodes that need no battery or power-harvesting module are typically preferred, as they allow minimizing the cost and simplifying the maintenance.

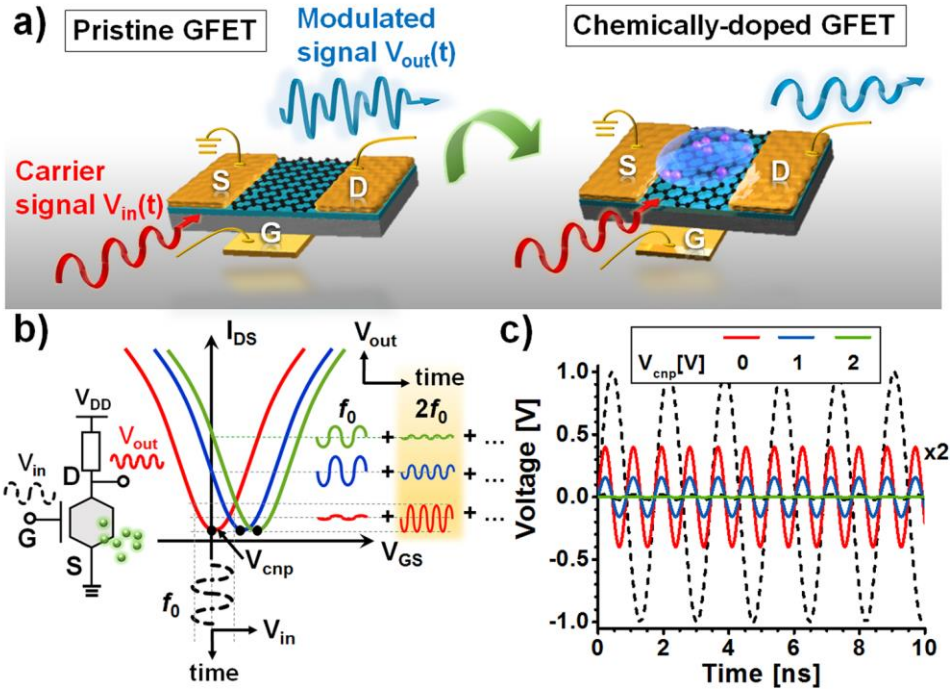

Figure 5.1. Graphene harmonic sensor

Schematics of frequency modulation in pristine (V_{cnp}=0V) and chemically doped ($|V_{cnp}|$>0V) GFETs. (b) Frequency modulation by a single GFET for different V_{cnp} positions. (c) Simulated (using Agilent Advanced Design Systems (ADS) frequencydoubling effect for a pristine GFET (dashed line) and a chemically doped GFET with different $|V_{cnp}|$ values (solid lines) [17].

5.1. Quad-ring Mixer Topology

Here, we propose and theoretically demonstrate the potential of a fully passive graphene-based harmonic sensor using an innovative graphene circuit, which combines functions of sensor, frequency modulator, and energy harvesters within a single module.

Figures 5.2(a) and 5.2(b) show the system block diagram and the circuit design for this all-graphene harmonic sensor. We adopt a diplexing technique, which consists of a dual-resonance graphene antenna and the chip-scale low-pass filter (LPF)/high-pass filter (HPF), to couple the received fundamental tone (e.g., 5.8GHz) into the graphene multiplier and to out-couple the modulated second harmonic (e.g., 11.6 GHz) back to free space, as schematically shown in Fig. 5.2(a). In the sensor-frequency modulator module, the quad-ring mixer topology formed by four GFETs may not only serve as chemical receptors but also constitute a passive, nonlinear transponder with the amplitude of second-harmonic output being dynamically modulated by chemical gating. In this scenario, the onset voltage of each GFET is tuned by the chemical or biological exposures on graphene channels of GFETs. Such harmonic tag may not only be tractable in position [18] but also re-radiate frequency-modulated RF signals that carry sensed information in terms of harmonic amplitude. We have conducted the circuit simulation based on the physics-driven GFET model for the quad-ring frequency multiplier in Fig. 5.2(b). Figure 5.2(c) shows the simulated second harmonic waveforms under different V_{cnp} values; here, the impedance of input and output ports are assumed to be 50 Ω, which is matched to most RF electronic systems, and the intrinsic V_{cnp} of each GFET is assumed to be zero (i.e., pristine graphene). For simplicity, we assume that the parasitic and resistance of contacts are ignorable. Due to the symmetric "V-shape" drain current-gate voltage characteristics of GFETs, the conversion gain (the voltage ratio between second harmonic and fundamental tone) is zero if all four graphene receptors are matched to zero V_{cnp}. It is surprisingly seen that when the V_{cnp} of graphene is slightly increased due to the surface binding of chemical or biological agents, the output amplitude of second harmonic can be dramatically modulated even for

a very small change in V_{cnp}. This can be attributed to the symmetry breaking in the drain current-gate voltage relationship of GFETs, which leads to the nonlinear rectification effect produced by the quad-ring circuit. Figure 5.2(d) shows the simulated conversion (voltage) gain against Vcnp for the GFET frequency multiplier in Fig. 5.2(c), with an input voltage of 0.3 V. The impact of input signal amplitude on the sensor performance can be found in the online supplementary material. We note that this passive graphene circuit as an RF rectifier can operate even when the input voltage is as low as 0.3 V, which is, however, not possible for conventional semiconductor rectifiers (e.g., silicon-based diode has a typical turn-on voltage at 0.7 V (Ref. [22]). It is seen from Fig. 5.2(d) that the conversion gain may sensitively reflect the value of V_{cnp} that is determined by the existence and concentration of dopants [121]. Due to the ambipolar charge transports in graphene, both n-type and p-type dopants may yield the same conversion gain, provided the resulted jV_{cnpj} are the same, as shown in Fig. 5.2(c). As can be seen in Fig. 5.2(d), the peak position of conversion gain $V_{cnp,peak}$ is around Vin/2. In the low V_{cnp} region ($V_{cnp}<V_{cnp,peak}$), the conversion gain experiences a dramatic increase even for a small increase in V_{cnp}. Such property could be of particular interest for highly sensitive, molecule-level sensing, as the detection of second-harmonic signal alarms specific chemical or biological events. On the other hand, in the high V_{cnp} region ($V_{cnp} > V_{cnp,peak}$) the conversion gain would slowly decrease and eventually saturate at certain V_{cnp} values, as the input RF signal experience a weaker nonlinearity. For very large V_{cnp} values, the conversion gain approaches zero. In other words, in high V_{cnp} region, it has lower sensitivity but larger dynamic range, making it suitable for the real-time monitoring of heavy doping process or long-term chemical/biological exposure events. In this sense, even if the intrinsic V_{cnp} is not close to

zero, it will still be useful as a sensor operating in high V_{cnp} conditions. Here, we also consider a realistic scenario, in which the fluctuation of V_{cnp} for four GFETs could possibly exist. For some selected V_{cnp} points in Fig. 5.2(d), we simulated a thousand of qual-ring mixers, with V_{cnp} values of their constituent GFETs being randomly perturbed by [100] 10%. The symbols and error bars in Fig. 5.2(d) represent the mean values and standard deviations of our numerical experiments, showing that the sensitivity of this GFET-based transponder sensor is quite robust to V_{cnp} fluctuations.

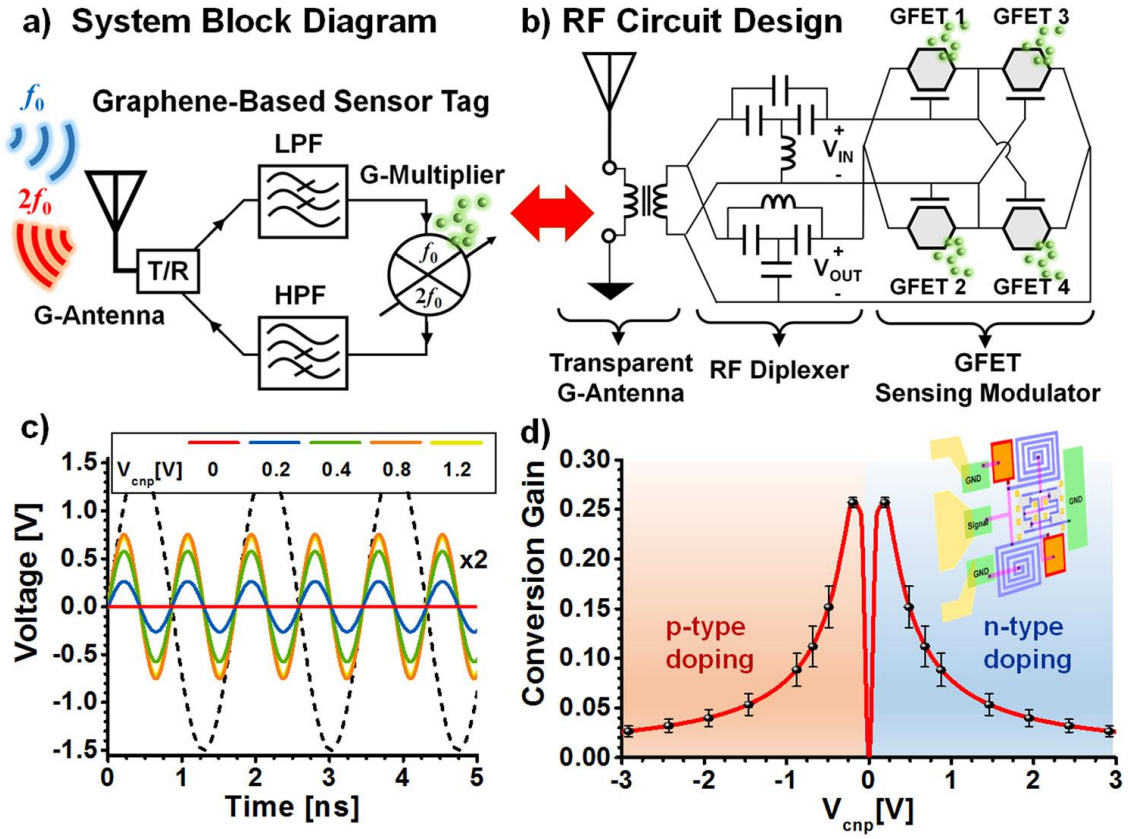

Figure 5.2. GFET-based quad-ring topology

(a) System and (b) circuit designs for a self-powered all-graphene harmonic sensor. (c) Simulated secondharmonic output waveform for the circuit in (b), with different V_{cnp} values of GFETs. (d) Simulated second-harmonic conversion (voltage) gain against the shift of V_{cnp}, under an RF input voltage as low as 0.3 V; here symbols and error bar represent mean values and standard deviations, which were obtained by simulating a thousand of qual-ring mixers, with V_{cnp} of four GFETs being randomly perturbed by 10% [17].

5.2. Dual-ring Sensing Topology

We propose here a new self-activated GFET-based harmonic sensor comprising reduced number of GFETs and much simplified interconnection scheme, as shown in Fig. 5.3(b). In this single-balance RF circuit, the paired GFETs are inductively coupled to a hybrid-fed antenna. Compared to the circuit topology of the quad-ring mixer in [17], this design allows a more compact device footprint and reduced fabrication complexity, while improved sensing linearity and reliability. In this study, we will compare the sensing performance between the dual-ring (single-balanced) and quad-ring (double-balanced) GFET-based sensing-modulator; here, the circuit simulations were conducted based on the realistic physics-based device compact model that has been verified with experimental results. We also consider a practical scenario in which chemical agents could randomly bind to receptors on the graphene surface, resulting in non-consistent drifts of V_{cnp} in different GFETs and, therefore, fluctuations in the frequency conversion efficiency of the GFET-based sensing-modulator. To address this issue, we present a new decoding and error estimation process for analyzing chemical gating levels from wirelessly sensed high harmonics, by means of the artificial neural network (ANN), within the realm of machine learning. We show that with the pattern recognition of the second and third-harmonic output signals, the mean value of V_{cnp} and its variations ΔV_{cnp}, and consequently the corresponding changes in chemical dopant concentrations can be robustly and accurately

read. This pattern-recognition-based method could potentially achieve more reliable harmonic sensing.

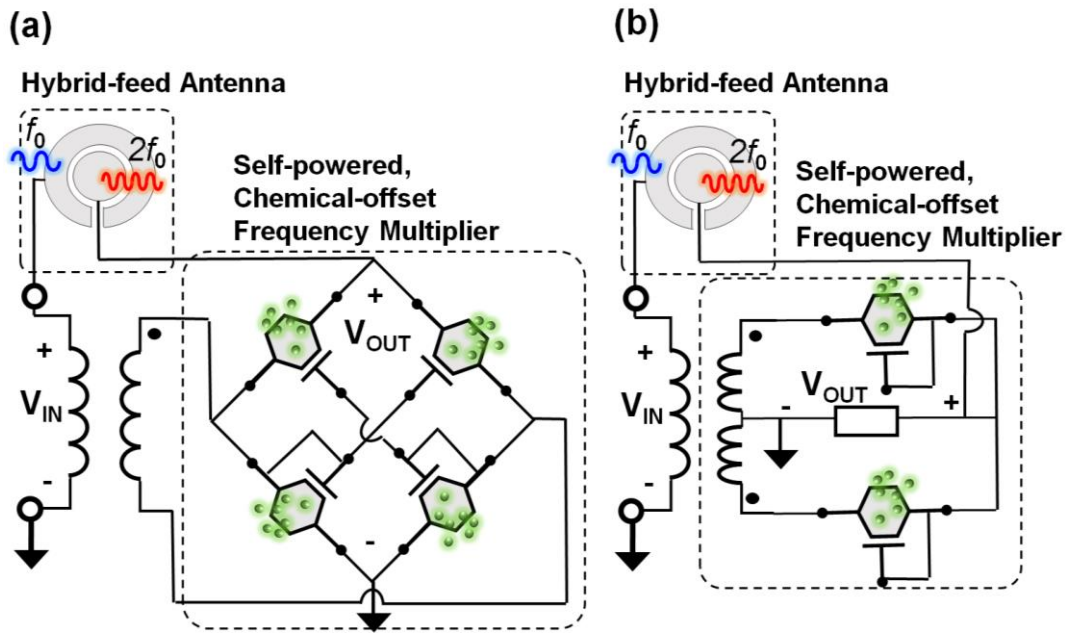

Figure 5.3. GFET-based dual-ring topology

Circuit diagram for (a) the quad-ring (double-balanced) sensing modulator and (b) the dual-ring (single-balanced) sensing-modulator. Both circuits are based on GFETs and inductively coupled to a hybrid-fed patch antenna, of which the first port receives the input signal at the fundamental frequency and the second port transmits the second-harmonic output to the interrogator/reader [97] .

Figures 5.3(a) and 5.3(b) respectively present the circuit design for two different types of fully-passive, graphene-based harmonic sensors, which are based on quad-ring and dual-ring self-biased GFETs. Such sensing-modulators can be coupled either to the RF input/output ports of a hybrid-feed antenna [233], or to two individual antennas resonating

at fundamental frequency and second harmonic. In this fully-passive circuit, the self-biased GFET plays a dual role: a receptor for chemical sensing and a nonlinear RF component for frequency modulation. In this scenario, V_{cnp} of individual GFETs would determine magnitudes of high harmonic outputs. In contrast to the quad-ring mixer circuit [Fig. 5.3(a)] [17], the single-balanced design [Fig. 5.3(b)], proposed for the first time here, possesses several advantages, as it requires fewer graphene transistors, much simplified interconnection circuits, and, therefore, more compact size and lower cost. More interestingly, it offers improved linearity and sensitivity than the quad-ring design. We have conducted the circuit simulations for the sensing modulator circuits in Fig. 5.3, by assuming the following device parameters: channel width $W = 80\ \mu$m, channel length $L = 50\ \mu$m, relative dielectric constant of gate oxide $\varepsilon_{ox}/\varepsilon_0 = 9$ (e.g. Al_2O_3), thickness of gate oxide $t_{ox} = 25$ nm, carrier mobility $\mu = 3000\ cm^2/(V.s)$, which is close to what reported in literature. For simplicity, we ignore the parasitic capacitance and resistance. This is approximately valid at moderately low operating frequencies. Figures 5.4(a) and 5.4(b) respectively present the time-domain and frequency-domain simulation results for the dual-ring sensing-modulator, with V_{cnp} of GFETs varying from 0 V to 0.5 V; here the input is a monochromatic, sinusoidal signal 432 MHz [dashed line in Fig. 5.4(a)]. Figures 5.5(a) and 5.5(b) are similar to Figs. 5.4(a) and 5.4(b), but for the quad-ring design. It is seen that for both designs, the magnitude of the output signal, particularly at the second harmonic, can be sensitively modulated by the drift of Dirac point. In general, V_{cnp} can be sensitively determined by concentrations of reactive gases or molecules that lead to n-/p-type doping effects. From Fig. 5.4(a), we find that the simple dual-ring design would act like a full-wave rectifier, of which fundamental tone and other odd harmonics are suppressed, with

their magnitude much lower than even harmonics. On the other hand, the quad-ring circuit [Fig. 5.5(a)] acts like the half-wave rectifier, of which even and odd harmonics are both significant. This is very counterintuitive, as in the conventional (unipolar) silicon-based frequency multiplier, the quad-ring circuit is comparatively better than the dual-ring structure in terms of generating clean odd-harmonic peaks. Figures 5.4(c) and 5.5(c) respectively present contours of the second-harmonic conversion gain (which is defined as the voltage ratio between the output second harmonic and the input fundamental tone) as a function of input voltage (V_{in}) and GFETs' V_{cnp}, for the GFET-based dual-ring and quad-ring circuits. We note that if V_{cnp} of all graphene receptors are matched to zero (i.e. pristine graphene), the conversion gain is zero for any arbitrary input voltage, due to the symmetric, V-shape current-voltage characteristics of GFETs. From Figs. 5.4(c) and 5.5(c), it is evident that V_{cnp} of GFETs can drastically affect the second-harmonic conversion gain, regardless of amplitude of the input signal. We should note that although the conversion gain increases with increasing the magnitude of input signal, however, even for a small input signal, the second-harmonic conversion gain can be modulated over a wide range by shifting V_{cnp} of GFETs. Figures 5.6(a) and 5.6(b) respectively report the contour of the sensitivity as functions of pH and V_{in} for the dual-ring and quad-ring circuits; here, the sensitivity is defined as the derivative of output second-harmonic amplitude with respect to the pH, which is related to the V_{cnp} by the Grahame equation. Again, it is seen that although the quad-ring circuit may offer a very high sensitivity in the low V_{cnp} regime, the dual-ring design, however, provides a better sensing linearity than the quad-ring one. Moreover, the sensitivity is rather independent of the amplitude of input signal, implying that robust sensing is potentially possible. We note that a large input signal is possible by

using passive transformers, which are commonly used in RFID tags and IoT sensors, or by adopting the nearfield communication (NFC) schemes.

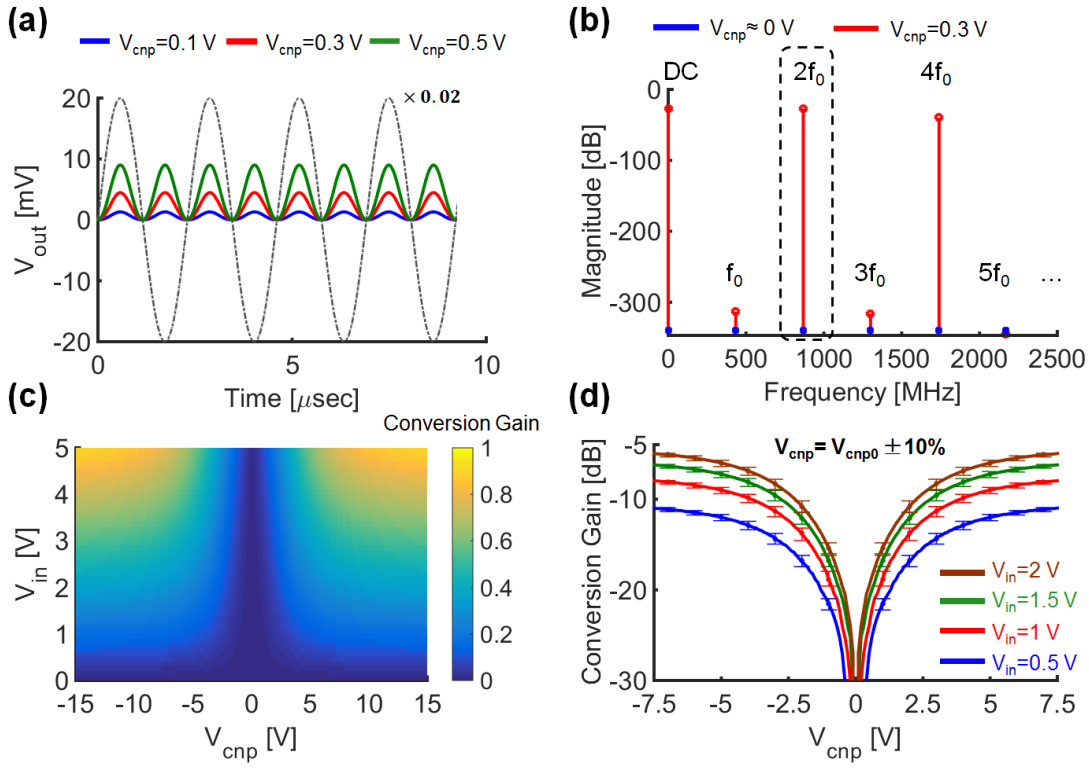

Figure 5.4. Dual-ring topology analysis

Simulation results for the dual-ring sensing-modulator circuit in Fig. 2(b). (a) Time-domain output signals for different V_{cnp} values of GFETs. (b) First five harmonics of the output signal (spectral analysis) with V_{cnp} = 0 V (blue lines) and V_{cnp} = 0.3 V (red lines); in (a) and (b), the voltage of input fundamental tone is 1 V. (c) Contours of second harmonic conversion gain as a function of input voltage amplitude (V_{in}) and GFET's V_{cnp}. (d) Second-harmonic conversion gain against V_{cnp} for different RF input voltages (error bar shows standard deviations obtained by carrying out 10^4 simulations, with V_{cnp} of individual GFETs randomly perturbed by 10 %) [97].

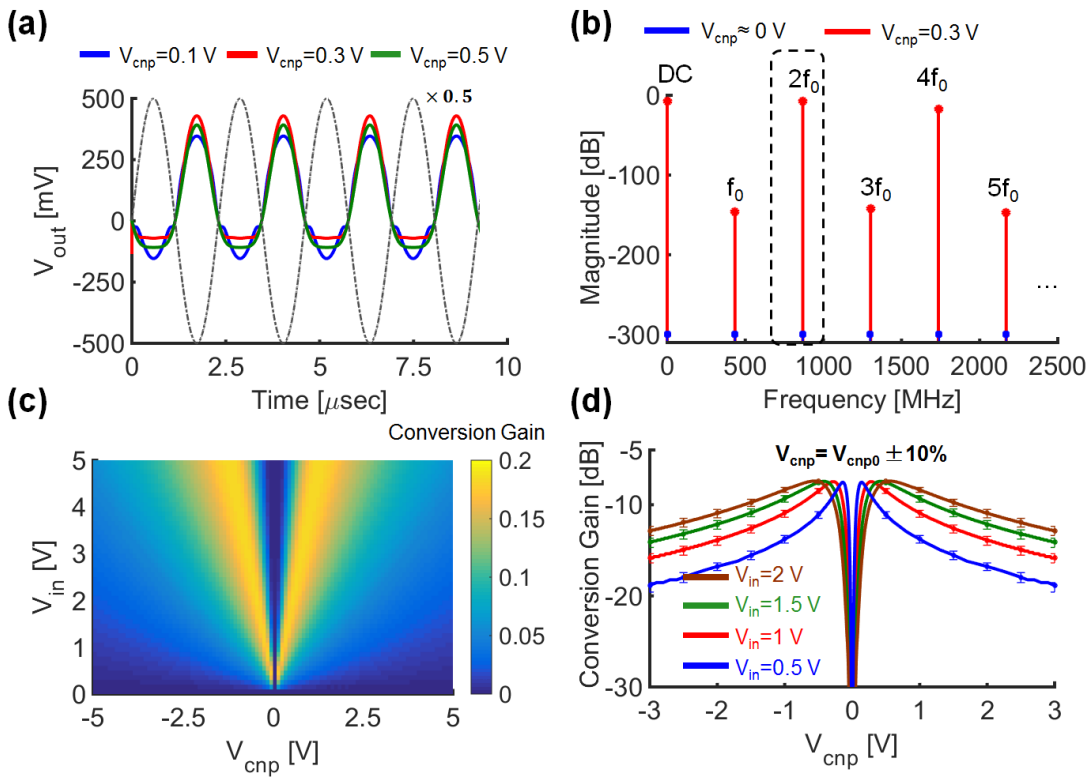

Figure 5.5. Quad-ring topology analysis

Simulation results for the quad-ring sensing-modulator circuit in Fig. 2(a). (a) Time-domain output signals for different V_{cnp} values of GFETs. (b) First five harmonics of the output signal (spectral analysis) with V_{cnp} = 0 V (blue lines) and V_{cnp} = 0.3 V (red lines); in (a) and (b), the voltage of input fundamental tone is 1 V. (c) Contours of second harmonic conversion gain as a function of input voltage amplitude (V_{in}) and GFETs' V_{cnp}. (d) Second-harmonic conversion gain against V_{cnp} for different RF input voltages (error bar shows standard deviations obtained by carrying out 10_4 simulations, with V_{cnp} of individual GFETs randomly perturbed by 10 %) [97].

Here, we also consider practical cases in which V_{cnp} of individual GFETs could fluctuate. To elucidate the influence of V_{cnp} fluctuation on robustness and reliability of the proposed sensing-modulators, we have randomly perturbed V_{cnp} of GFETs by +-10% in

both quad-ring and dual-ring circuits, and have conducted the simulation for 10^4 times for getting reliable statistical results. Figures 5.4(d) and 5.5(d) present the second-harmonic conversion gain against the average V_{cnp} for the dual-ring and quad-ring sensing-modulators, under different applied input voltages (V_{in} = 0.5, 1, 1.5 and 2 V). The symbols and error bars in Figs. 5.4 (d) and 5.5(d) represent the mean values and standard deviations of our numerical experiments, clearly showing that the sensitivity of both types of transponder sensors is quite robust to V_{cnp} fluctuations. Comparing the conversion gain between the dual-ring and quad-ring GFET circuits, we find that the dual-ring design exhibits better performance in terms of linearity and sensitivity. When a quad-ring sensor is exposed to chemical agents, there are two distinct operation regions. In the low V_{cnp} region ($V_{cnp} \leq V_{cnp,peak}$), a slight increment of V_{cnp} leads to a dramatic increase in the magnitude of the second harmonic output, whereas, in the high V_{cnp} region ($V_{cnp} \geq V_{cnp,peak}$), the conversion gain slowly decreases with increasing the V_{cnp} value and eventually saturates. On the other hand, the dualring GFET circuit shows a linear dependence between the conversion gain and V_{cnp}, over a broad range of V_{cnp}, thereby providing a better linearity than the quad-ring design. From Figs. 5.4(d) and 5.5(d), it is worth mentioning that the maximum second-harmonic conversion gain of the dual-ring circuit could be greater than that of the quad-ring one, as a direct consequence of the major difference between full-wave and halfwave rectifications.

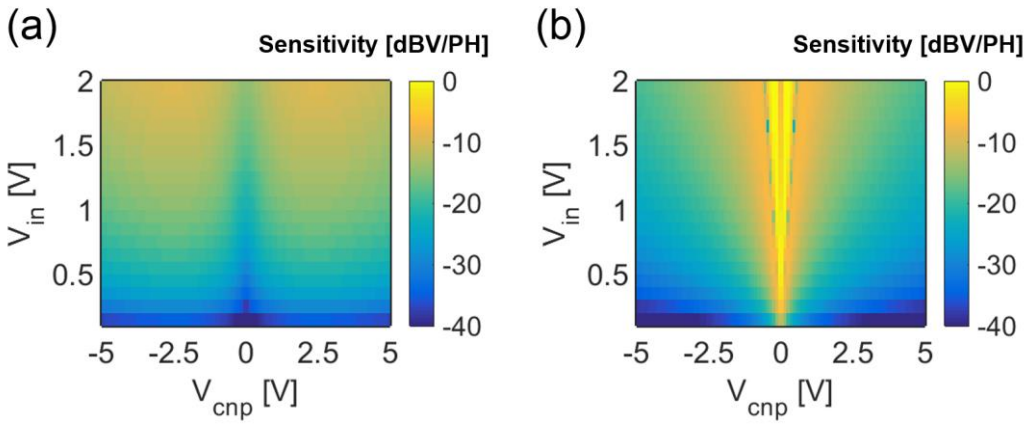

Figure 5.6. Two topology sensitivity analysis

Contours of sensitivity as a function of V_{in} and V_{cnp} for (a) the dual-ring sensing modulator and (b) the quad-ring sensing-modulator [97].

VI. HARMONIC SENSING SYSTEMS

Parts of this chapter have been presented in [17],[122].

Copyright © AIP 2016, IEEE 2016.

The possibility to Integration of harmonic sensing systems is investigated in this chapter considering two major characteristics of the earlier proposed topologies. First, all-graphene system is introduced based on the integration of proposed GFET-based sensors by dual-band graphene antenna which potentially enables a compact, light-weight, and flexible sensing system beneficial for enormous applications such as wearable and portable wireless sensors for healthcare monitoring. In the other part, a dual-band antenna design is experimentally investigated to merge both Rx an Tx antennas, those work in two separate frequency, to a single compact antenna viable to realize integrated harmonic sensing systems.

6.1. Integrated Graphene Antennas and Circuits

In this section, we propose the concept and design of all-graphene harmonic sensor that monolithically integrates graphene-based circuits and antenna to support all the necessary functions, including sensing, signal modulation, and wireless data transmission and power harvesting, as shown in Fig. 6.1 Graphene may offer higher electrochemical reaction sensitivity, better specificity (with suitable surface functional treatment) [99],[107]-[108], and physical properties that are particularly desirable for eye-wearable devices and transparent electronics, such as optical transparency and flexibility. Figure 6.1 shows a graphene-based harmonic sensor on a soft contact lens [235]-[236] that could

continuously detect, for instance, the pathogen and infectious keratitis of interest without intervening the users' quotidian life. A multilayered graphene antenna can be used here to ensure the optical transparency of device and the fabrication compatibility with the graphene circuitry, which will be studied in the following.

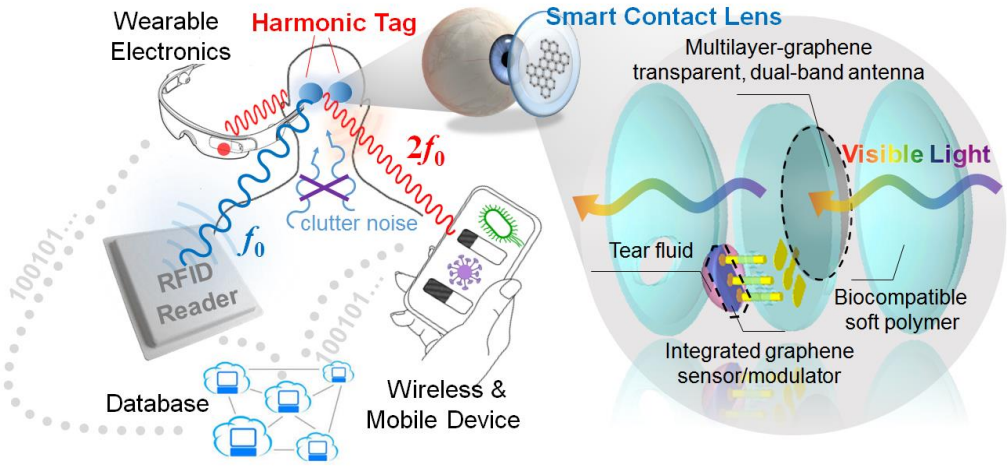

Figure 6.1. All-graphene harmonic sensor

Schematics of a compact harmonic transponder sensor (or harmonic sensor) based on the microfluidic-integrated, dual-resonance elliptical patch antenna connected to the diplexer and frequency doubler. The sensor can receive and retransmit RF signals with orthogonal frequencies and polarizations for avoiding clutter and cross talk [17].

The harmonic sensor system typically uses multiple antennas operating at fundamental and sub-harmonic/harmonic frequencies, which, although being convenient in design, will sacrifice the compactness of the sensing system. With the aim of making the whole sensor system compact and light-weight, we designed a dual-resonance graphene

monopole antenna, connected to a lumped-element-based diplexer that eliminates possible RF interference and intermodulation [227]. Figure 6.2(a) shows our designed graphene antenna, which is fed by a 50 Ω coplanar ground-signal-ground (GSG) transmission line on a flexible, transparent, and biocompatible polyethylene terephthalate (PET) substrate. The PET substrate has a thickness of 10 mil, permittivity of 3.5, and loss tangent of 0.0027. Although a monolayered graphene antenna offers advantages of transparency (i.e., 97.7% transparency in the visible spectrum), its radiation efficiency is lower than conventional printed metallic antennas, primarily due to the relatively low RF conductivity of graphene. To mitigate this problem, we study antennas made of multilayered graphene, which is expected to have higher RF conductivity. The graphene's dynamic conductivity in the RF regime can be modeled by the Kubo's formula as [111],[228],[229]-[230],

$$\sigma_{\mathrm{RF}}(\omega) = -j\frac{Nq^2E_{\mathrm{F}}}{\pi\hbar^2(\omega - j\tau^{-1})} \approx \frac{Nq^2E_{\mathrm{F}}}{\pi\hbar^2\tau^{-1}} \tag{8}$$

where N, E_{F} and γ are the number of layer, Fermi energy, and phenomenological relaxation time of graphene, ω is the angular frequency, q is the electron charge, and $\hbar$ is the reduced Planck constant.

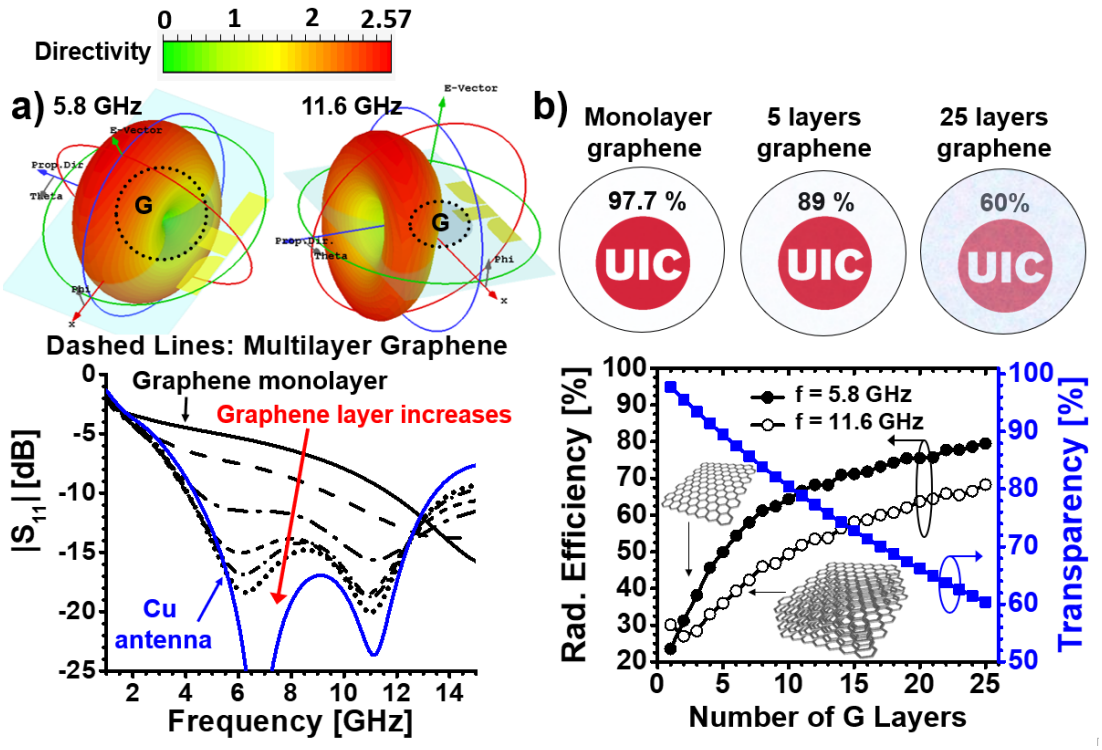

Figure 6.2. Graphene antenna

(a) Far-field radiation pattern of a graphene planar monopole antenna, and its return loss (S_{11}) for different number of graphene layers: N = 1, 2, 5, 10, 15, 25 (top to down). (b) Transparency and simulated radiation efficiency for the antenna in (a), made of different number of graphene layers [17].

Figure 6.2(a) shows the design and the full-wave simulation results for radiation pattern (top) and return loss (bottom) of this graphene antenna, designed to operate at 5.8 GHz (fundamental tone) and 11.6 GHz (second harmonic). The RF carrier frequency of 5.8 ± 0.75 GHz and 10.7-12.2 GHz should be compatible with the FCC protocol [231]. The multilayered graphene sheet has a diameter of 6 mm, a Fermi energy of 0.26 eV, and a

phenomenological relaxation time of 20 fs, which were extracted from experimental results [232]. It is evidently seen from Fig. 6.2(a) that the return loss can be lower than -10 dB for a multilayered graphene patch and that the impedance matching can be improved by increasing the number of graphene layer. The optical transmittance of a multilayered graphene is given by:

$$T_s = \left| 1 - \frac{\eta_0 / 2}{\eta_0 / 2 + \sigma_{\text{optical}}^{-1}} \right|^2 \tag{9}$$

where η_0 is the free space impedance and σ_{optical} is the optical conductivity of graphene. In the visible spectrum ($\hbar\omega_0 >> E_F, k_B T$), σ_{optical} is almost constant and can be expressed as [99]:

$$\sigma_{\text{optical}}(\omega_0) = N \frac{q^2}{4\hbar} \tanh\left(\frac{\hbar\omega_0 - 2E_F}{4K_B T} \right) \approx N \frac{q^2}{4\hbar} \tag{10}$$

, which ω_0 is the angular frequency of visible light, K_B is the Boltzmann constant, and T is the temperature.

Figure 6.2(b) shows simulated dependencies of optical transparency and RF radiation efficiency on the number of graphene layers for the graphene antenna in Fig. 6.2(a). It is seen that the radiation efficiency increases significantly with increasing the number of graphene layers. The radiation efficiency may approach 90% (comparable to printed metallic antenna) when the number of graphene layer $N > 25$ (which has a relatively low opacity of 60%). Although the opacity is sacrificed when multilayered graphene is used, a satisfactory transparency can still be obtained (e.g. for N = 15, the optical transmittance is greater than 70 %, while the radiation efficiency is greater than 55 %). For

a moderately thick graphene, i.e., $10 < N < 20$, there exists a good compromise between the device opacity and radiation efficiency. A transparent graphene antenna may be particularly suitable for the integration with the GFET circuitry, which makes the whole system transparent and flexible, of interest for various wearable and implantable sensing and communication applications.

From the system level point of view, with the aim of making the whole sensor system compact and light-weight, we have designed and fabricated a broadband graphene monopole antenna, which is connected to a lumped element-based diplexer [Fig. 6.3(a)]. We have designed a coplanar waveguide (CPW)-fed graphene monopole antenna on a flexible, transparent and biocompatible polyethylene terephthalate (PET) substrate. Here the graphene monolayer was prepared by the chemical vapor deposition (CVD). The CVD grown graphene was then transferred to the PET substrate, followed by the photolithographic patterning and the (Oxygen plasma) dry etching. The transfer process was repeated several times to make the multi-layered graphene. Finally, copper was deposited by E-beam evaporation and lithographically patterned as the CPW feed. In the RF regime, although a graphene antenna offers advantages of lightweight and optical transparency, it may be less efficient compared with the printed metallic antennas, due to its relatively high electrical resistance. In order to mitigate the low radiation efficiency and the difficulty in impedance matching, we investigate here the RF antenna made of multi-layered graphene, whose conductivity would increase with increasing the number of graphene layers. Figure 6.3(b) shows the fabricated transparent graphene antenna with different number of stacked monolayers. As expected, when a multilayered graphene is used, the opacity is somewhat sacrificed. Still, a high transparency can be obtained, even

with 8 graphene monolayers. In our numerical modeling, the full-wave electromagnetic simulation [237] was conducted, with the dynamic conductivity of graphene being modeled by the semiclassical Kubo formula [111],[228]. Here an elliptical graphene sheet has a long-axis diameter of 7 mm, short-axis diameter 5.9 mm, a Fermi energy of 0.25 eV, and a phenomenological scattering rate of 41.3 meV. It is evident from Fig. 6.2(a) that the return loss can be improved by increasing the number of graphene layer, which is verified both experimentally and theoretically. The measured return loss shows a moderately broadband bandwidth of operation, which may find potential applications in UWB communication systems that require a high transparency. For an 8-layergraphene antenna, the calculated radiation efficiency is 40 % ~ 55 % in the frequency range 3 GHz to 15 GHz. For a 3-layer graphene antenna, although being almost invisible in the visible light spectrum, shows a high reflection (S_{11}) and a low radiation efficiency of 10% ~ 20% in the same frequency range. We expect that the radiation efficiency and return loss of the graphene antenna can be further improved by increasing the number of graphene monolayers, which is experimentally feasible. This transparent, broadband monopole antenna, when used in the harmonic sensor system, allows for receiving the RF carrier frequency of 5.8 ± 0.75 GHz (C band) and retransmitting the modulated signal at 10.7-12.2 GHz (X band), which are compatible with the FCC protocol. The simulated radiation pattern for this graphene antenna, showing a satisfactory radiation directivity comparable to a linear monopole antenna.

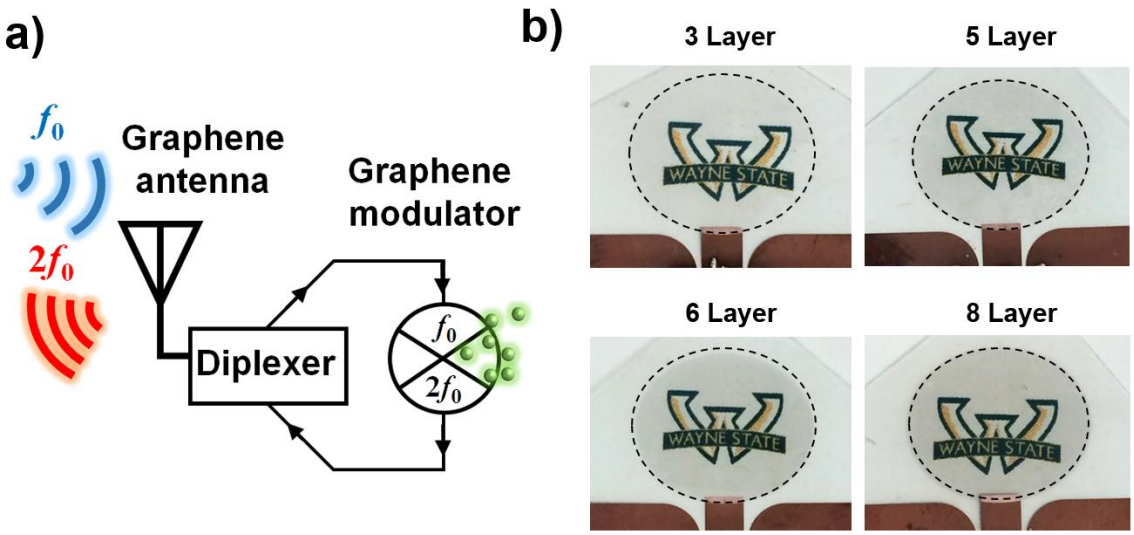

Figure 6.3. Graphene antenna

(a) Far-field radiation pattern of a graphene planar monopole antenna, and its return loss (S_{11}) for different number of graphene layers: N = 1, 2, 5, 10, 15, 25 (top to down). (b) Transparency and simulated radiation efficiency for the antenna in (a), made of different number of graphene layers [122].

Graphene Antenna Fabrication

The fabrication process is shown in Fig. 6.4 PET sheet was first cleaned with IPA and mounted on a Si wafer. Single-layer graphene was grown by chemical vapor deposition (CVD) using Cu foil (Basic copper, 75 μm thick) as a substrate. Briefly, the clean Cu foil was first loaded in the chamber and heated up to 1000 ºC while H_2 was flowing into the chamber with 3 sccm. Then CH_4 gas was added to the chamber as a source for Carbon with 30 sccm for 30 min and decomposed to form graphene sheets on the copper

surface. A thin poly-methyl methacrylate (Microchem PMMA 495) layer was spin-coated on top of graphene/Cu to protect graphene during the transfer process. Copper was etched using ammonium persulfate (Transene APS-100) diluted in DI water with a ratio of (1:10) overnight. The graphene/PMMA sheets were then transferred to the PET using a clean glass slide. In order to improve the adhesion between graphene and PET, 30 sec O_2 plasma was performed on the PET surface with 100 W right before the transfer. The sample was dried in the room temperature for 30 min and then washed using Acetone/IPA to remove the PMMA from the top. The same transfer process was performed to generate multi-layer graphene. Graphene was patterned in the cleanroom by photolithography and dry etching using O_2 plasma for 30 sec at 100 W. For the contact pads, a thin (150 nm) Cu was deposited by electron beam evaporation and patterned by photolithography and wet etching using APS. Finally, the device was released from Si wafer and attached to the SMA connector using a silver conductive epoxy kit (MG Chemicals). The whole process was performed at room temperature without the hot plate or oven drying to prevent the expansion of the PET sheet which can cause misalignment during photolithography.

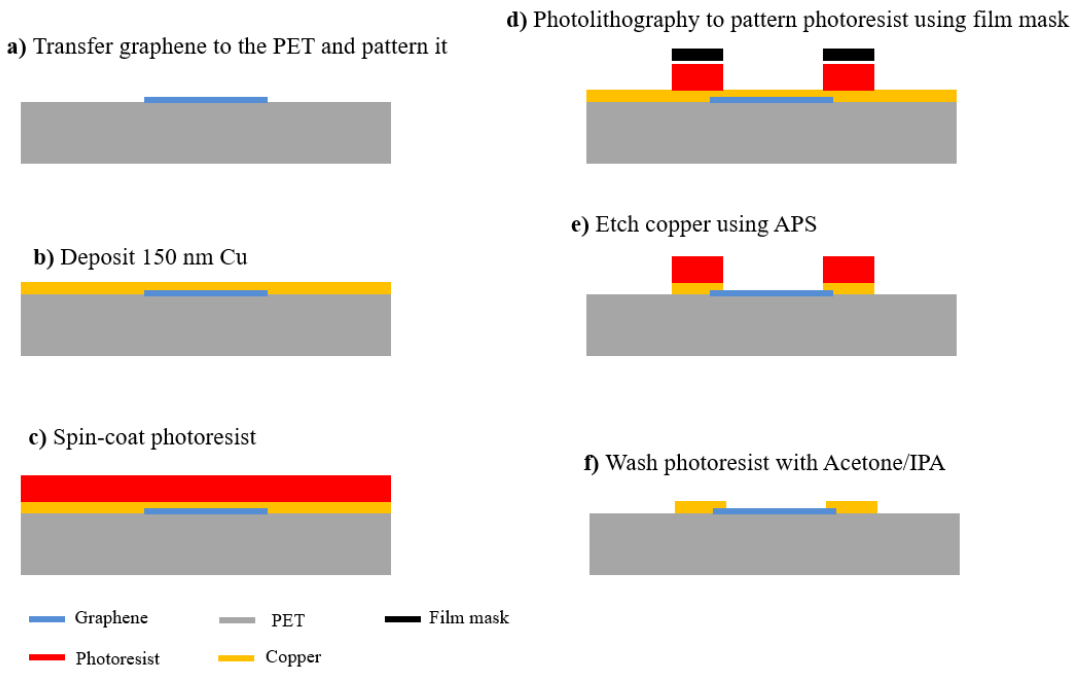

Figure 6.4. Graphene antenna fabrication process

6.2. Dual-Band Patch Antenna

Figure 6.5 presents the compact hybrid-fed patch antenna, which may remove at least one antenna, or diplexer and matching network in conventional harmonic sensor tags. Figure 6.5(a) compares measurement and full-wave simulation results for the reflection coefficients S_{11} and S_{22} of this hybrid-fed antenna, designed to operate at 2.9 GHz (received fundamental tone in port 1) and 5.8 GHz (re-transmitted second harmonic in port 2); S_{21} is less than -30 dB over the frequency band of interest (not shown here), ensuring very low crosstalk and good isolation between two ports. It is seen from Fig. 6.5(a) that experimental results show excellent agreement with the simulation results. Figure 6.5(b) presents full-

wave simulation results for radiation patterns of this antenna on the E and H planes at the fundamental and second-harmonic frequencies. Here, we obtain satisfactory antenna gain and sidelobe levels.

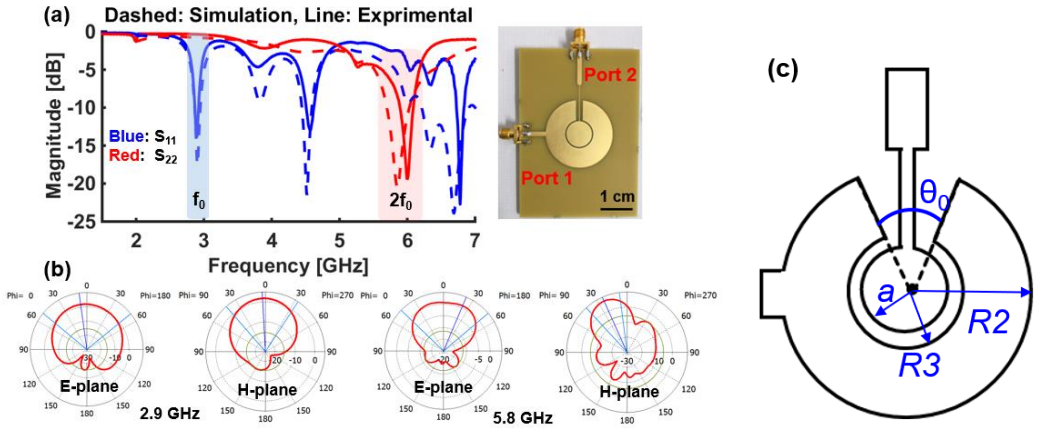

Figure 6.5. Dual-band patch antenna

(a) Measurement (dashed line) and simulation results (solid line) for the reflection coefficients at two ports of the hybrid-fed patch antenna. (b) Full-wave simulation results for radiation patterns on the E and H planes at the fundamental and second-harmonic frequencies, (c) the geometry of patch antenna [215].

Figure 6.5(c) shows the geometry of the proposed dual-band patch antenna consisting of an elliptical patch and a concentric split-ring patch. The transcendental equation for the split-ring resonant cavity can be derived as [238]:

$$J_n'(kR_2)Y_n'(kR_3) - J_n'(kR_3)Y_n'(kR_2) = 0,$$
$$n = \frac{m\pi}{2\pi - \theta_0} \text{ for } m = 1,2,3\ldots, \tag{11}$$

where $J_n(\cdot)$ and $Y_n(\cdot)$ are the Bessel functions of the first and the second kinds, $k = \omega\sqrt{\varepsilon_r \varepsilon_0 \mu_0}$, ε_0 and μ_0 are the free-space permittivity and permeability. Based on Eq. (11), we have designed the split-ring patch antenna with $m = 3$ (TM_{310} mode), $R_2 = 38.2$ mm, $R_3 = 22$ mm, and $\theta_0 = 30°$, which provides a narrow-band resonance at the fundamental frequency (1.31 GHz here).

VII. CONCLUSIONS AND FUTURE WORKS

Toward commercializing harmonic-based sensors, we have planned to prove this concept by a system-level demonstration analysis. For this purpose, first, we need experimentally demonstrate a harmonic transponder using commercial components such as frequency multiplexer and resistive or capacitive sensor. Making a compact module connected to a dual-band antenna or near-field coil antenna is the design challenges that should be investigated in the future works. On the other hand, considering the trad-off between the working frequency and the proper module size is the first part of the study which may lead to a commercial compact harmonic sensor. This work can be developed to a multifunctional system that benefits the smart city approach as schematically shown in Fig. 7.1 [83].

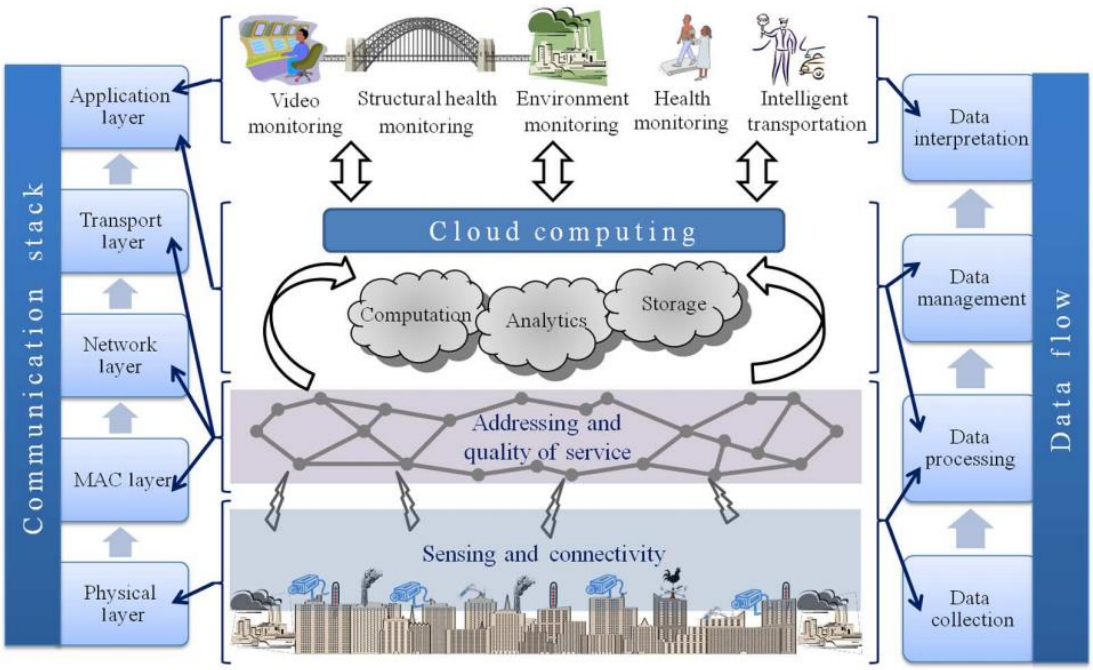

Figure 7.1. IoT infrastructure from three different domains for smart city approach [83].

Furthermore, commercial GFETs are easily accessible today which shed a light to the future progress of GFET based multifunctional sensing systems. One of the commercial products consisting of more than 30 GFETs with different characteristics in which easily can be used to develop more complicated topologies for harmonic sensing. On the other hand, with having several GFETs on a single substrate as a chip, it will be more feasible to demonstrate a multi-functional sensing system by functionalizing each GFET to detect the desired agent.

In summary, we propose a passive, compact and ultrasensitive wireless harmonic sensor based on the graphene transistors. We first theoretically show that such a circuit can act as a chemically-modulated frequency doubler with its second-harmonic conversion gain sensitively responsible for the chemical gating effect, which is not possible with conventional solid-state circuits. We experimentally demonstrate the possibility to achieve sensing and frequency modulation using a properly biased single-state GFET. Then, we develop a physics-based compact model to describe characteristics of GFETs and exploit it to simulating new types of self-powered sensing-modulators constituted by back-gate GFETs. Furthermore, we propose a fully passive harmonic sensor that monolithically integrates a dual-band multilayered graphene antenna and a passive graphene sensor/frequency modulator. We also demonstrate both near-field and far-field wireless sensing schemes with suitably designed GFET circuits and antennas. Next, we study a

multi-agent wireless RFID sensor consisting of a GFET-based frequency multiplier. We show that combining the (bio-)chemical sensing and frequency multiplication functions of GFETs, a compact and monolithically-integrated harmonic-based sensor can be realized. On the other hand, we propose a new wireless readout scheme based on the artificial neural network for accurately determining the drift of Dirac point (resulting from binding of gas, molecular or chemical agents onto GFETs) and the range of Dirac-point fluctuation in GFETs. We show that the machine learning approach can be useful in analyzing the measurement results of this harmonics-based nonlinear sensor with high data dimensions (i.e., multiple output harmonics). The proposed graphene-based harmonic sensors, receiving the fundamental tone and retransmitting the high harmonics, show great potential to realize the low-noise, low-interference chemical sensing in scattering-rich and noisy measurement environments. In the other hand, the proposed all-graphene wireless sensor has several unique advantages, including high sensitivity, lightweight, conformality, transparency, and low background and clutter noise, which are expected to benefit a variety of wireless health and wearable technologies on transparent platforms for sensing PH/gas/ molecular/chemical agents as well as IoTs sensor for smart city approach.

APPENDICES

APPENDICES

Typical CVD graphene

Even without intentional doping, CVD graphene is p-doped due to adsorption of adsorbed gas molecules and residual ammonium persulfate from the transfer process. Typical values for E_F and $\hbar\gamma$ we measure from ellipsometry is ~ 260 meV and ~33 meV, respectively. It corresponds to a mobility of ~ 2410 $cm^2V^{-1}s^{-1}$, using the relationship $\mu = e\pi\hbar V_F^2/(\hbar\gamma\ E_F)$. This mobility is consistent with the specification provided by our CVD graphene vendor. The scattering time $\tau = \gamma^{-1} \sim$ 20 fs.

We can chemically dope CVD graphene with magic blue. Using our doping recipe, we typically get E_F ~ 450 meV and $\hbar\gamma$ ~ 22 meV. A mobility μ of ~2100 $cm^2V^{-1}s^{-1}$ and a τ of ~ 30 fs can be calculated from these numbers.

The increase of scattering time τ after chemical doping can be attributed to the screening of charged impurities. This trend is consistent with the previous work done by IBM [Yan *et al.*, Nature Nanotechnology 7, 330-334 (2012).] However, the mobility in their paper is higher than ours, which means they have used graphene with better qualities.

APPENDICES (continued)

GFET model in simulators

Here I present the method which has been used for simulating GFET-based circuits in this dissertation. The analytical drift-diffusing model which is presented in chapter 3, has been verified by our experimental results and then for more complicated circuit design is defined in ADS software. The figures A1 and A2 show the GFET module definition and parameters, and the analytical equations for this model in simulator software. Further, another more accurate model also is used as illustrated in Fig. A3 comprising circuit elements inside the software.

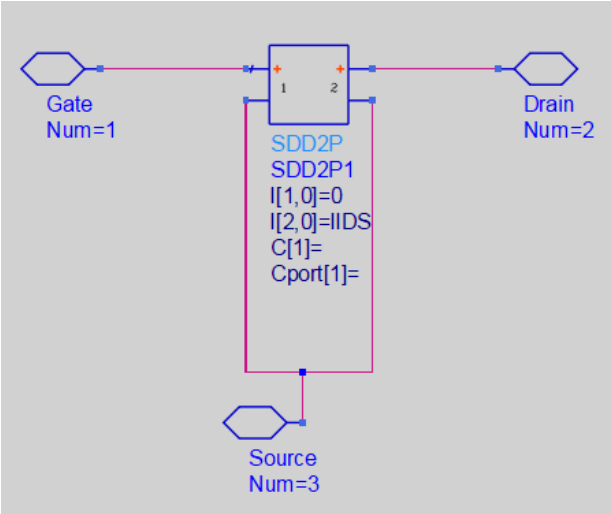

Figure A1: GFET topology circuit simulator Agilent Advanced Design Systems (ADS)

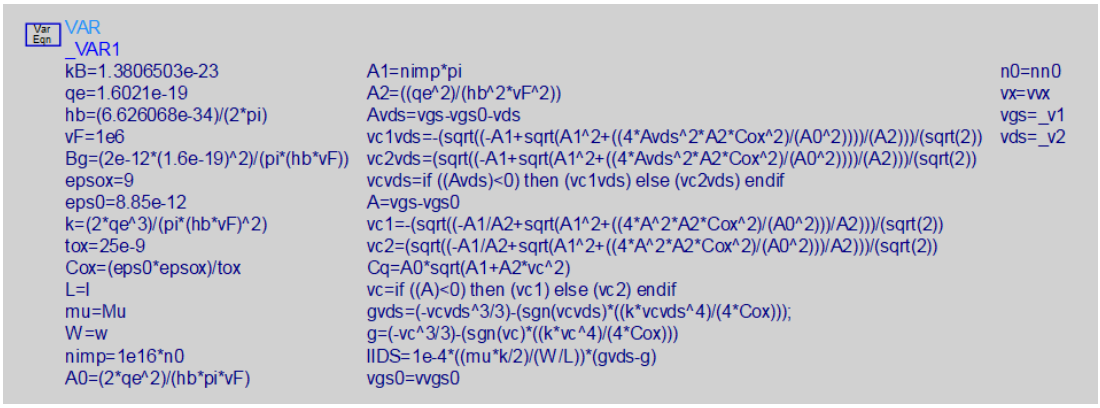

Figure A2: Analytical model defined in simulation environment

```
VAR
VAR1
kB=13806503e-23
hb=(6626068e-34)/(2*pi)
vF=1e6
Bg=(2e-12*(16e-19)^2)/(pi*(hb*vF))
epsox=9
eps0=885e-12
k=(2*e^3)/(pi*(hb*vF)^2)
tox=25e-9
Cox=(eps0*epsox)/tox
L=0.5e-4
mu=2000
W=25e-4
Vc=if ((VFB-Vgs+Vds)<0) then (-1*Cox+sqrt(Cox^2-(2*k*Cox*(VFB-Vgs+Vds))))/k else (Cox-sqrt(Cox^2+(2*k*Cox*(VFB-Vgs+Vds))))/k endif
Vc2=if ((VFB-Vgs)<0) then (-1*Cox+sqrt(Cox^2-(2*k*Cox*(VFB-Vgs))))/k else (Cox-sqrt(Cox^2+(2*k*Cox*(VFB-Vgs))))/k endif
gVc=(-(Vc^3)/3)-(sgn(Vc)*((k*(Vc^4))/(4*Cox)))
```

```
gVc2=(-(Vc2^3)/3)-(sgn(Vc2)*((k*(Vc2^4))/(4*Cox)))
Leff0=L+((mu*abs(Vds))/vF)
IDS=((1e-4*mu*k*W)/(2*L))*(gVc-gVc2)
gDiff=-Vc^2-((k*Vc^3*sgn(Vc))/Cox)
gDiff2=-Vc2^2-((k*Vc2^3*sgn(Vc2))/Cox)
gm=((1e-4*mu*k*W)/(2*L))*(gDiff-gDiff2)
VFB=Vdirac
Vgs=_v1
Vds=_v2
```

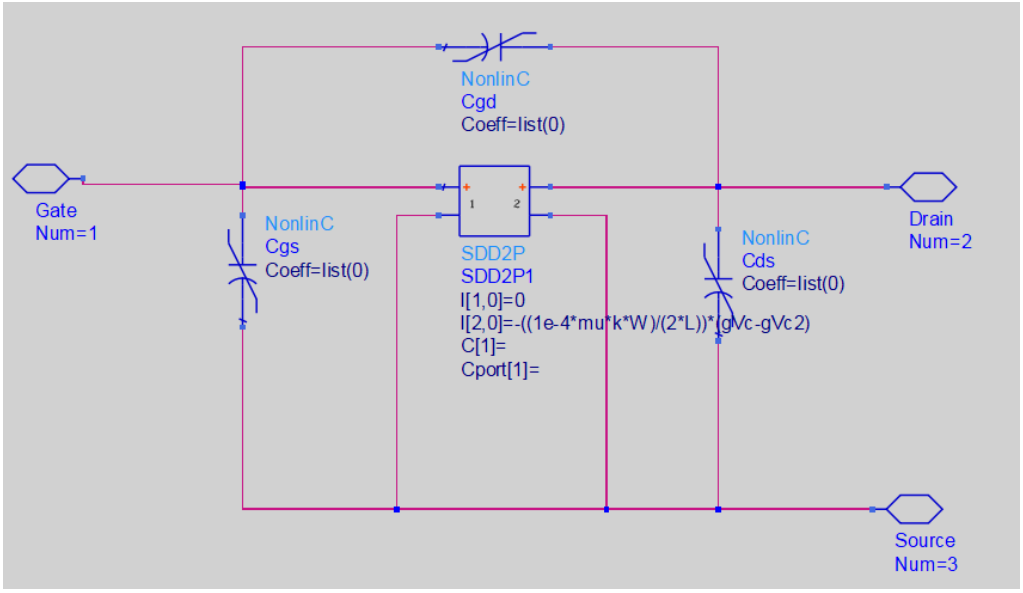

Figure A3: More accurate analytical model defined in simulation environment

The symbol of GFET is designed as shown in Fig. A4, here three-port transistor is derived by the circuit design that is shown as well. Moreover, the topology of circuit design in ADS simulator is illustrated in Fig. A5 and A6, for quad-ring and multi-functional topologies respectively.

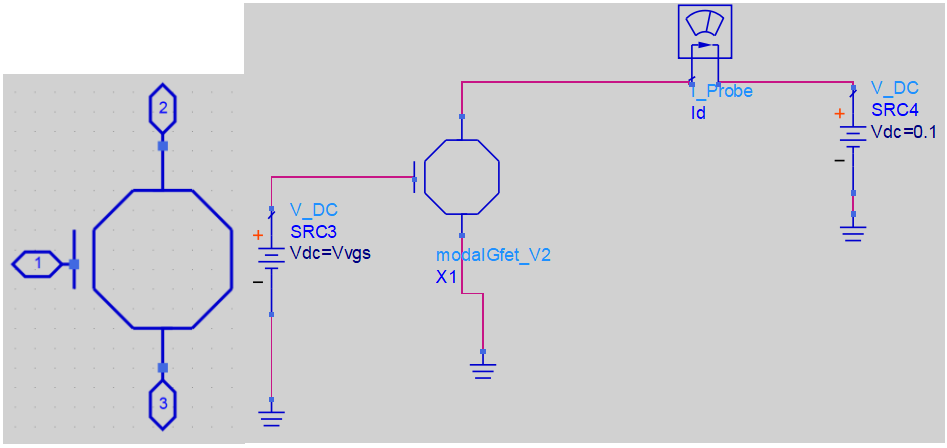

Figure A4: GFET symbol and driving circuit in simulation software

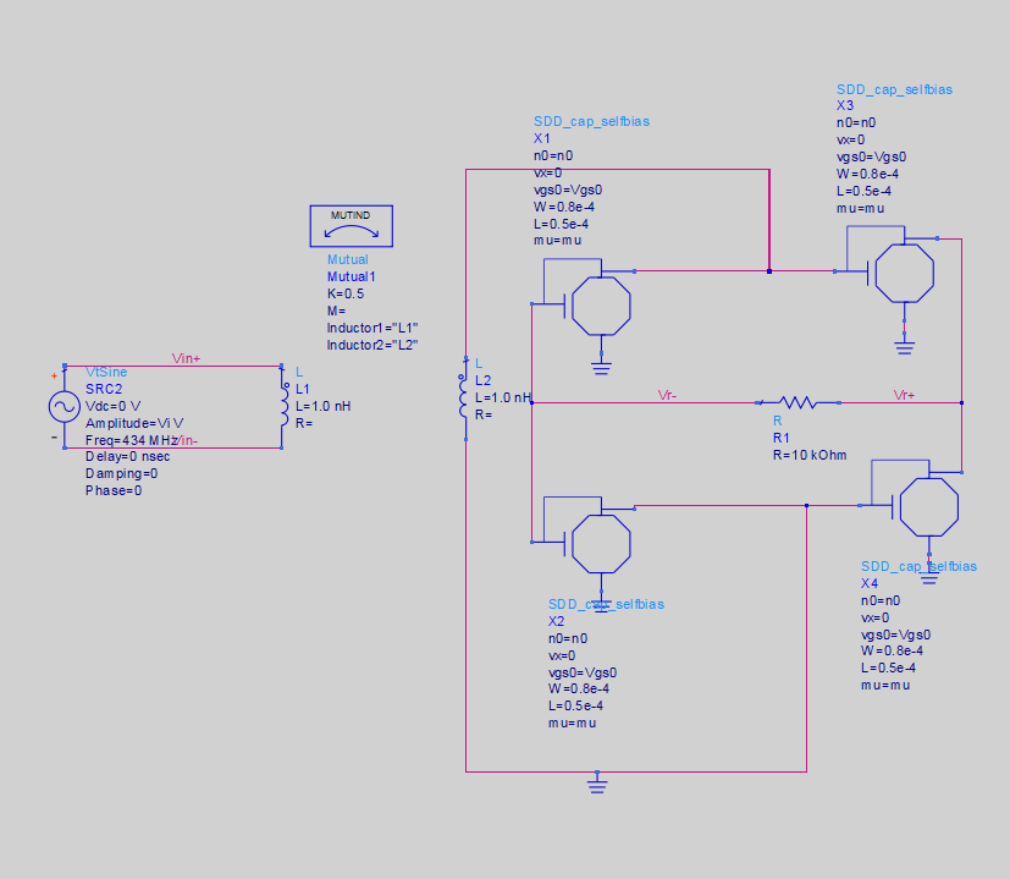

Figure A5: Circuit diagram of quad-ring topology in simulation software

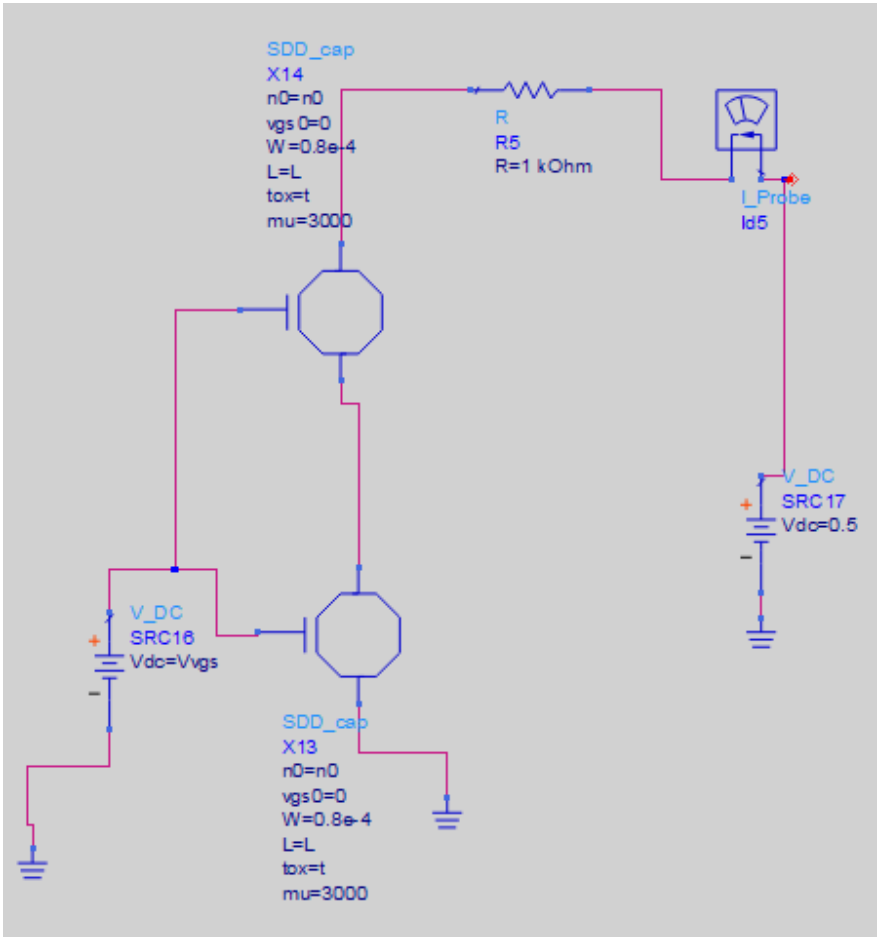

Figure A6: Circuit diagram of multi-agent topology in simulation software

Finally, the analytical model also defined in Matlab Simulink as illustrated in Fig. A7 and the analytical code below, to verify the simulator results and compare different circuit topologies.

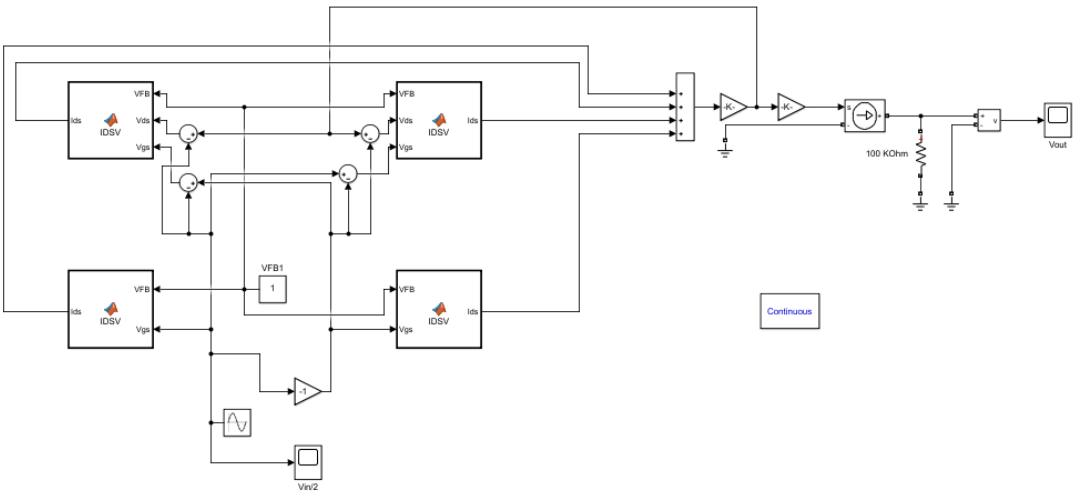

Figure A7: Block diagram of quad-ring topology in Matlab Simulink

```
function Ids= IDSV(VFB,Vds,Vgs)
%VFB=0.5;
%Vds=0.01;
%Vgs=-minVgs:0.01:MaxVgs;
```

```
%f=10;
%define constant
e=1.6021e-19;
kB=1.3806503e-23;
hb=(6.626068e-34)/(2*pi);
%muc=Ef.*1.6e-19;
%w=2.*pi.*f;
vF=1e6;
Bg=(2e-12*(1.6e-19)^2)/(pi*(hb*vF));
epsox=9;
eps0=8.85e-12;
k=(2*e^3)/(pi*(hb*vF)^2);
tox=25e-9;
Cox=(eps0*epsox)/tox;
L=0.5e-4;
mu=1000;
W=25e-4;
%define Vc
%Vcn=(-1*Cox+(Cox^2-(2.*k.*Cox.*(VFB-Vgs+Vds))).^0.5)./k;
%Vcp=(Cox-(Cox^2+(2.*k.*Cox.*(VFB-Vgs+Vds))).^0.5)./k;
 %change IDS vs. Vgs
```

```
Vc=Vgs;

Vc2=Vgs;

gVc=Vgs;

gVc2=Vgs;

IIDS=Vgs;

IDS=Vgs;

gDiff=Vgs;

gDiff2=Vgs;

gm=Vgs;


for i = 1:1:length(Vgs);

if (VFB-Vgs(i)+Vds(i))<0

   Vc(i)=(-1*Cox+(Cox^2-(2*k*Cox*(VFB-Vgs(i)+Vds(i))))^0.5)/k;

else

   Vc(i)=(Cox-(Cox^2+(2*k*Cox*(VFB-Vgs(i)+Vds(i))))^0.5)./k;

end

if (VFB-Vgs(i))<0

   Vc2(i)=(-1*Cox+(Cox^2-(2*k*Cox*(VFB-Vgs(i))))^0.5)/k;

else

   Vc2(i)=(Cox-(Cox^2+(2*k*Cox*(VFB-Vgs(i))))^0.5)/k;

end
```

```
%define g(Vc)
gVc(i)=(-(Vc(i)^3)/3)-(sign(Vc(i))*((k*(Vc(i)^4))/(4*Cox)));
gVc2(i)=(-(Vc2(i)^3)/3)-(sign(Vc2(i))*((k*(Vc2(i)^4))/(4*Cox)));
Leff0=L+((mu*abs(Vds))/vF);
IIDS(i)=((1e-4*mu*k*W)/(2*L))*(gVc(i)-gVc2(i));
IDS(i)=(IIDS(i));
gDiff(i)=-Vc(i)^2-((k*Vc(i)^3*sign(Vc(i)))/Cox);
gDiff2(i)=-Vc2(i)^2-((k*Vc2(i)^3*sign(Vc2(i)))/Cox);
gm(i)=((1e-4*mu*k*W)/(2*L))*(gDiff(i)-gDiff2(i));
end
%figure (2);
%hold on
%plot(Vgs,1e6.*IDS)


Ids = IDS;
```

Copyrights

In this appendix, I present the copyright permissions for the articles, whose contents were used in this thesis. The list of the articles includes an article in Applied Physic Letters (Huang et al., 2016), an article in IEEE sensor Journals (Hajizadegan et al., 2017), an article in Microsystems and Nanoengineering (Huang et al., 2016), and an article in Proceed IEEE Sensors (Shahini et al., 2016).

AIP PUBLISHING LICENSE
TERMS AND CONDITIONS

Mar 31, 2020

This Agreement between UNIVERSITY OF ILLINOIS at Chicago -- Mehdi Hajizadegan ("You") and AIP Publishing ("AIP Publishing") consists of your license details and the terms and conditions provided by AIP Publishing and Copyright Clearance Center.

License Number	4799640919061
License date	Mar 31, 2020
Licensed Content Publisher	AIP Publishing
Licensed Content Publication	Applied Physics Letters
Licensed Content Title	Toward transparent and self-activated graphene harmonic transponder sensors
Licensed Content Author	Haiyu (Harry) Huang, Maryam Sakhdari, Mehdi Hajizadegan, et al
Licensed Content Date	Apr 25, 2016
Licensed Content Volume	108
Licensed Content Issue	17
Type of Use	Thesis/Dissertation
Requestor type	Author (original article)
Format	Electronic

Portion	Figure/Table
Number of figures/tables	4
Title	Research Assistant
Institution name	UNIVERSITY OF ILLINOIS at Chicago
Expected presentation date	Apr 2020
Portions	Figures 1-4
Requestor Location	UNIVERSITY OF ILLINOIS at Chicago 1200 W Harrison St, CHICAGO, IL 60612 United States Attn: UNIVERSITY OF ILLINOIS at Chicago
Total	0.00 USD

Terms and Conditions

AIP Publishing -- Terms and Conditions: Permissions Uses

AIP Publishing hereby grants to you the non-exclusive right and license to use and/or distribute the Material according to the use specified in your order, on a one-time basis, for the specified term, with a maximum distribution equal to the number that you have ordered. Any links or other content accompanying the Material are not the subject of this license.

1. You agree to include the following copyright and permission notice with the reproduction of the Material:"Reprinted from [FULL CITATION], with the permission of AIP Publishing." For an article, the credit line and permission notice must be printed on the first page of the article or book chapter. For photographs, covers, or tables, the notice may appear with the Material, in a footnote, or in the reference list.
2. If you have licensed reuse of a figure, photograph, cover, or table, it is your responsibility to ensure that the material is original to AIP Publishing and does not contain the copyright of another entity, and that the copyright notice of the figure, photograph, cover, or table does not indicate that it was reprinted by AIP Publishing, with permission, from another source. Under no circumstances does AIP Publishing purport or intend to grant permission to reuse material to which it does not hold appropriate rights.

You may not alter or modify the Material in any manner. You may translate the Material into another language only if you have licensed translation rights. You may not use the Material for promotional purposes.

3. The foregoing license shall not take effect unless and until AIP Publishing or its agent, Copyright Clearance Center, receives the Payment in accordance with Copyright Clearance Center Billing and Payment Terms and Conditions, which are incorporated herein by reference.
4. AIP Publishing or Copyright Clearance Center may, within two business days of granting this license, revoke the license for any reason whatsoever, with a full refund payable to you. Should you violate the terms of this license at any time, AIP Publishing, or Copyright Clearance Center may revoke the license with no refund to you. Notice of such revocation will be made using the contact information provided by you. Failure to receive such notice will not nullify the revocation.
5. AIP Publishing makes no representations or warranties with respect to the Material. You agree to indemnify and hold harmless AIP Publishing, and their officers, directors, employees or agents from and against any and all claims arising out of your use of the Material other than as specifically authorized herein.
6. The permission granted herein is personal to you and is not transferable or assignable without the prior written permission of AIP Publishing. This license may not be amended except in a writing signed by the party to be charged.
7. If purchase orders, acknowledgments or check endorsements are issued on any forms containing terms and conditions which are inconsistent with these provisions, such inconsistent terms and conditions shall be of no force and effect. This document, including the CCC Billing and Payment Terms and Conditions, shall be the entire agreement between the parties relating to the subject matter hereof.

This Agreement shall be governed by and construed in accordance with the laws of the State of New York. Both parties hereby submit to the jurisdiction of the courts of New York County for purposes of resolving any disputes that may arise hereunder.

V1.2

Questions? customercare@copyright.com or +1-855-239-3415 (toll free in the US) or +1-978-646-2777.

IEEE
Requesting permission to reuse content from an IEEE publication

Graphene Sensing Modulator: Toward Low-Noise, Self-Powered Wireless Microsensors

Author: Mehdi Hajizadegan
Publication: IEEE Sensors Journal
Publisher: IEEE
Date: 15 Nov.15, 2017

Copyright © 2017, IEEE

Thesis / Dissertation Reuse

The IEEE does not require individuals working on a thesis to obtain a formal reuse license, however, you may print out this statement to be used as a permission grant:

Requirements to be followed when using any portion (e.g., figure, graph, table, or textual material) of an IEEE copyrighted paper in a thesis:

1) In the case of textual material (e.g., using short quotes or referring to the work within these papers) users must give full credit to the original source (author, paper, publication) followed by the IEEE copyright line © 2011 IEEE.
2) In the case of illustrations or tabular material, we require that the copyright line © [Year of original publication] IEEE appear prominently with each reprinted figure and/or table.
3) If a substantial portion of the original paper is to be used, and if you are not the senior author, also obtain the senior author's approval.

Requirements to be followed when using an entire IEEE copyrighted paper in a thesis:

1) The following IEEE copyright/ credit notice should be placed prominently in the references: © [year of original publication] IEEE. Reprinted, with permission, from [author names, paper title, IEEE publication title, and month/year of publication]
2) Only the accepted version of an IEEE copyrighted paper can be used when posting the paper or your thesis on-line.
3) In placing the thesis on the author's university website, please display the following message in a prominent place on the website: In reference to IEEE copyrighted material which is used with permission in this thesis, the IEEE does not endorse any of [university/educational entity's name goes here]'s products or services. Internal or personal use of this material is permitted. If interested in reprinting/republishing IEEE copyrighted material for advertising or promotional purposes or for creating new collective works for resale or redistribution, please go to http://www.ieee.org/publications_standards/publications/rights/rights_link.html to learn how to obtain a License from RightsLink.

If applicable, University Microfilms and/or ProQuest Library, or the Archives of Canada may supply single copies of the dissertation.

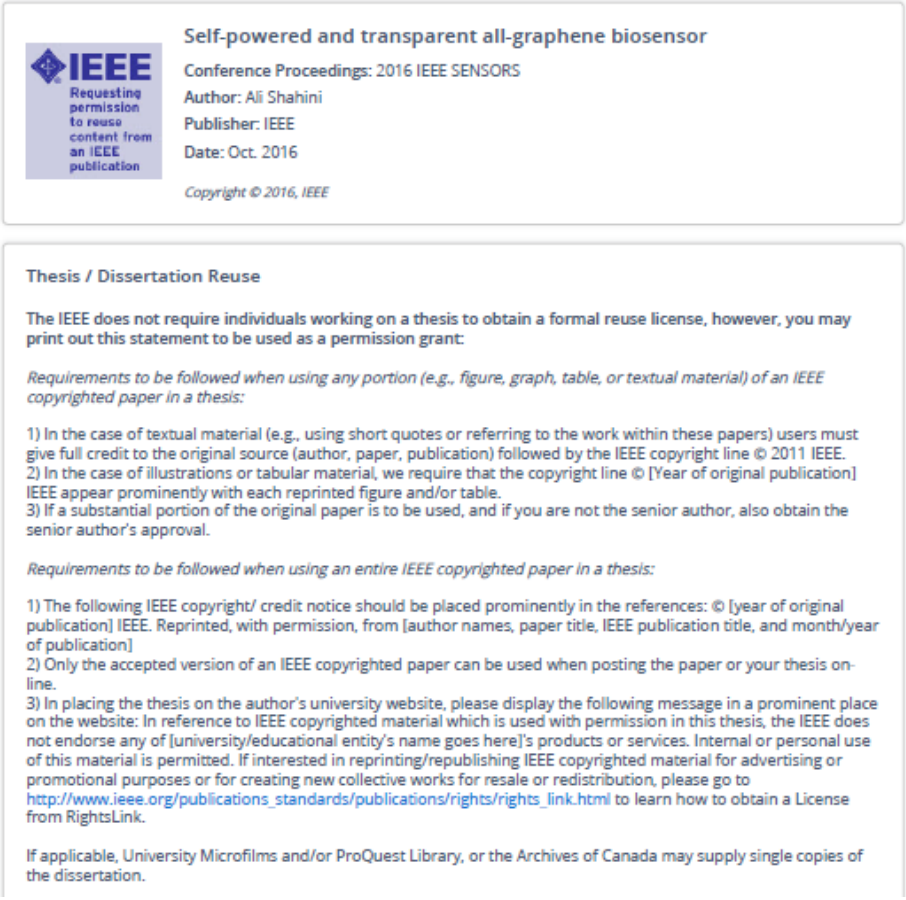

Self-powered and transparent all-graphene biosensor

Conference Proceedings: 2016 IEEE SENSORS

Author: Ali Shahini

Publisher: IEEE

Date: Oct. 2016

Copyright © 2016, IEEE

Requesting permission to reuse content from an IEEE publication

Thesis / Dissertation Reuse

The IEEE does not require individuals working on a thesis to obtain a formal reuse license, however, you may print out this statement to be used as a permission grant:

Requirements to be followed when using any portion (e.g., figure, graph, table, or textual material) of an IEEE copyrighted paper in a thesis:

1) In the case of textual material (e.g., using short quotes or referring to the work within these papers) users must give full credit to the original source (author, paper, publication) followed by the IEEE copyright line © 2011 IEEE.
2) In the case of illustrations or tabular material, we require that the copyright line © [Year of original publication] IEEE appear prominently with each reprinted figure and/or table.
3) If a substantial portion of the original paper is to be used, and if you are not the senior author, also obtain the senior author's approval.

Requirements to be followed when using an entire IEEE copyrighted paper in a thesis:

1) The following IEEE copyright/ credit notice should be placed prominently in the references: © [year of original publication] IEEE. Reprinted, with permission, from [author names, paper title, IEEE publication title, and month/year of publication]
2) Only the accepted version of an IEEE copyrighted paper can be used when posting the paper or your thesis on-line.
3) In placing the thesis on the author's university website, please display the following message in a prominent place on the website: In reference to IEEE copyrighted material which is used with permission in this thesis, the IEEE does not endorse any of [university/educational entity's name goes here]'s products or services. Internal or personal use of this material is permitted. If interested in reprinting/republishing IEEE copyrighted material for advertising or promotional purposes or for creating new collective works for resale or redistribution, please go to http://www.ieee.org/publications_standards/publications/rights/rights_link.html to learn how to obtain a License from RightsLink.

If applicable, University Microfilms and/or ProQuest Library, or the Archives of Canada may supply single copies of the dissertation.

Publisher: Springer Nature

Copyright © 2016, Springer Nature

Creative Commons

This is an open access article distributed under the terms of the Creative Commons CC BY license, which permits unrestricted use, distribution, and reproduction in any medium, provided the original work is properly cited.

You are not required to obtain permission to reuse this article.

To request permission for a type of use not listed, please contact Springer Nature

IEEE
Requesting permission to reuse content from an IEEE publication

A self-powered harmonic sensor based on simple graphene circuit and hybrid-fed antenna

Conference Proceedings:
2017 IEEE International Symposium on Antennas and Propagation & USNC/URSI National Radio Science Meeting

Author: Mehdi Hajizadegan

Publisher: IEEE

Date: July 2017

Copyright © 2017, IEEE

Thesis / Dissertation Reuse

The IEEE does not require individuals working on a thesis to obtain a formal reuse license, however, you may print out this statement to be used as a permission grant:

Requirements to be followed when using any portion (e.g., figure, graph, table, or textual material) of an IEEE copyrighted paper in a thesis:

1) In the case of textual material (e.g., using short quotes or referring to the work within these papers) users must give full credit to the original source (author, paper, publication) followed by the IEEE copyright line © 2011 IEEE.
2) In the case of illustrations or tabular material, we require that the copyright line © [Year of original publication] IEEE appear prominently with each reprinted figure and/or table.
3) If a substantial portion of the original paper is to be used, and if you are not the senior author, also obtain the senior author's approval.

Requirements to be followed when using an entire IEEE copyrighted paper in a thesis:

1) The following IEEE copyright/ credit notice should be placed prominently in the references: © [year of original publication] IEEE. Reprinted, with permission, from [author names, paper title, IEEE publication title, and month/year of publication]
2) Only the accepted version of an IEEE copyrighted paper can be used when posting the paper or your thesis on-line.
3) In placing the thesis on the author's university website, please display the following message in a prominent place on the website: In reference to IEEE copyrighted material which is used with permission in this thesis, the IEEE does not endorse any of [university/educational entity's name goes here]'s products or services. Internal or personal use of this material is permitted. If interested in reprinting/republishing IEEE copyrighted material for advertising or promotional purposes or for creating new collective works for resale or redistribution, please go to http://www.ieee.org/publications_standards/publications/rights/rights_link.html to learn how to obtain a License from RightsLink.

If applicable, University Microfilms and/or ProQuest Library, or the Archives of Canada may supply single copies of the dissertation.

BIBLIOGRAPHY

[1] F. Shrouf, J. Ordieres, and G. Miragliotta. “Smart factories in Industry 4.0: A review of the concept and of energy management approached in production based on the Internet of Things paradigm.” In *Industrial Engineering and Engineering Management (IEEM), 2014 IEEE International Conference on*, pp. 697-701. IEEE, 2014.

[2] Y. Lu, “Industry 4.0: A survey on technologies, applications and open research issues.” *J. Ind. Inf. Integr.*, vol. 6, p.p. 1-10, 2017.

[3] M. Wollschlaeger, Th. Sauter, and J. Jasperneite. “The future of industrial communication: Automation networks in the era of the internet of things and industry 4.0.” *IEEE Ind. Electron. Mag., vol.* 11, no. 1, p.p. 17-27, 2017.

[4] K.H. Chang, “Bluetooth: a viable solution for IoT? [Industry Perspectives].” *IEEE Wireless Commun.*, vol. 21, no. 6, p.p. 6-7, 2014.

[5] R.H. Weber, and R. Weber. *Internet of things*. vol. 12. Heidelberg: Springer, 2010.

[6] D. Evans, “The IoT, how the next evolution of the internet is changing everything.” Cisco, 2011.

[7] S.Ch. Mukhopadhyay, and N. K. Suryadevara. “Internet of things: Challenges and opportunities.” *In Internet of Things*, pp. 1-17. Springer, Cham, 2014.

[8] R. Want, “An introduction to RFID technology,” *IEEE Pervas. Comput*., vol. 5, no. 1, pp. 25–33, Jan. 2006.

[9] F. Klaus, RFID Handbook: Fundamentals and Applications in Contactless Smart Cards and Identification, 2nd ed. Hoboken, NJ, USA: Wiley, 2003.

[10] D. Kim, M. A. Ingram, and W. W. Smith, “Measurements of small-scale fading and path loss for long range RF tags,” *IEEE Trans. Antennas Propag*., vol. 51, no. 8, pp. 1740–1749, Aug. 2003.

[11] P. V. Nikitin and K. V. S. Rao, “Theory and measurement of backscattering from RFID tags,” *IEEE Antennas Propag. Mag*., vol. 48, no. 6, pp. 212–218, Dec. 2006.

[12] J. Landt, “The history of RFID,” *IEEE Potentials*, vol. 24, no. 4, pp. 8–11, Oct. 2005.

[13] C. He, Z. J. Wang, and V. C. M. Leung, “Unitary query for the M×L×N MIMO backscatter RFID channel,” *IEEE Trans. Wireless Commun*., vol. 14, no. 5, pp. 2613–2625, May 2015.

[14] C. He, Z. J. Wang, C. Miao, and V. C. M. Leung, “Block-level unitary query: Enabling orthogonal-like space-time code with query diversity for MIMO backscatter RFID,” *IEEE Trans. Wireless Commun.*, vol. 15, no. 3, pp. 1937–1949, Mar. 2016.

[15] M. M. Islam, J. Song, K. Rasilainen, and V. Viikari, “Optimization of RFID sensor with frequency modulation,” *IEEE Sensors J*., vol. 16, no. 15, pp. 5993–6002, Aug. 2016.

[16] M. Farhat, M. M. C. Cheng, K. Q. Le, and P. Y. Chen, “Nanoantenna harmonic sensor: Theoretical analysis of contactless detection of molecule with light,” *Nanotechnology*, vol. 26, p. 415201, Oct. 2015.

[17] H. Huang, M. Sakhdari, M. Hajizadegan, A. Shahini, D. Akinwande, and P. Y. Chen, "Toward transparent and self-activated graphene harmonic transponder sensors," *Appl. Phys. Lett*., vol. 108, no. 17, p. 173503, 2016.

[18] J. R. Riley, A. D. Smith, D. R. Reynolds, and A. S. Edwards, "Tracking bees with harmonic radar," *Nature*, vol. 379, p. 29, Jan. 1996.

[19] E. A. Capaldi et al., "Ontogeny of orientation flight in the honeybee revealed by harmonic radar," *Nature*, vol. 403, pp. 537–540, Feb. 2000.

[20] K. G. Ong and C. A. Grimes, "Tracking the harmonic response of magnetically-soft sensors for wireless temperature, stress, and corrosive monitoring," *Sens. Actuators A, Phys*., vol. 101, pp. 49–61, Sep. 2002.

[21] A. Lazaro, R. Villarino, and D. Girbau, "A passive harmonic tag for humidity sensing," *Int. J. Antennas Propag*., vol. 2014, Jul. 2014, Art. no. 670345.

[22] H. Huang, P. Y. Chen, C. H. Hung, R. Gharpurey, and D. Akinwande, "A zero power harmonic transponder sensor for ubiquitous wireless μL liquid-volume monitoring." *Sci. Rep*., vol. 6, p. 18795, Jan. 2016.

[23] H. Huang, P. Y. Chen, C. H. Hung, R. Gharpurey, and D. Akinwande, "Frequency hopped wireless passive sensing system with harmonic transponder antenna sensor," *in IEEE MTT-S Int. Microw. Symp. Dig*., pp. 1–4, May 2015,.

[24] J. Gubbi, R. Buyya, S. Marusic, and M. Palaniswami. "Internet of Things (IoT): A vision, architectural elements, and future directions." *Future Gener. Comput. Syst.*, vol. 29, no. 7, pp. 1645-1660, 2013.

[25] I. Lee, and K. Lee. "The Internet of Things (IoT): Applications, investments, and challenges for enterprises." *Business Horizons*, vol. 58, no. 4, pp. 431-440, 2015.

[26] R. Kanan, O. Elhassan, and R. Bensalem. "An IoT-based autonomous system for workers' safety in construction sites with real-time alarming, monitoring, and positioning strategies." *Autom. Constr.*, vol. 88, pp. 73-86, 2018.

[27] X. Qiu, H. Luo, G. Xu, R. Zhong, and G. Q. Huang. "Physical assets and service sharing for IoT-enabled Supply Hub in Industrial Park (SHIP)." *Int. J. Prod. Econ.*, vol. 159, pp. 4-15, 2015.

[28] J. Höller, D. Boyle, S. Karnouskos, S. Avesand, C. Mulligan, and V. Tsiatsis. *From machine-to-machine to the internet of things*. Cambridge: Academic Press, 2014.

[29] L. Kong, M. Khurram Khan, F. Wu, G. Chen, and P. Zeng. "Millimeter-wave wireless communications for IoT-cloud supported autonomous vehicles: Overview, design, and challenges." *IEEE Commun. Mag.*, vol. 55, no. 1, pp. 62-68, 2017.

[30] M. Keertikumar, M. Shubham, and R. M. Banakar. "Evolution of IoT in smart vehicles: An overview." In *Green Computing and Internet of Things (ICGCIoT), 2015 International Conference on*, pp. 804-809. IEEE, 2015.

[31] M. Gerla, E.K. Lee, G. Pau, and U. Lee. "Internet of vehicles: From intelligent grid to autonomous cars and vehicular clouds." In *Internet of Things (WF-IoT), 2014 IEEE World Forum on*, pp. 241-246. IEEE, 2014.

[32] K.M. Alam, M. Saini, and A. El Saddik. "Toward social internet of vehicles: Concept, architecture, and applications." *IEEE Access*, vol. 3, pp. 343-357, 2015.

[33] Y. Zhang, and J. Wen. "The IoT electric business model: Using blockchain technology for the internet of things." *Peer-to-Peer Networking and Applications*, vol. 10, no. 4, pp. 983-994, 2017.

[34] J. Ruan, and Y. Shi. “Monitoring and assessing fruit freshness in IOT-based e-commerce delivery using scenario analysis and interval number approaches.” *Information Sciences,* vol. 373, pp. 557-570, 2016.

[35] S. Singh, and N. Singh. “Internet of Things (IoT): Security challenges, business opportunities & reference architecture for E-commerce.” In *Green Computing and Internet of Things (ICGCIoT), 2015 International Conference on*, pp. 1577-1581. IEEE, 2015.

[36] B. Cheng, D. Zhu, S. Zhao, and J. Chen. “Situation-aware IoT service coordination using the event-driven SOA paradigm.” *IEEE Trans. Netw. Serv. Manage.,* vol. 13, no. 2, pp. 349-361, 2016.

[37] Ch. Wang, M. Daneshmand, M. Dohler, X. Mao, R.Q. Hu, and H. Wang. “Guest Editorial-Special issue on internet of things (IoT): Architecture, protocols and services.” *IEEE Sens. J.,* vol. 13, no. 10, pp. 3505-3510, 2013.

[38] Ch. Bhatt, N. Dey, and A.S. Ashour, eds. “Internet of things and big data technologies for next generation healthcare.” (2017): 978-3.

[39] Ch. Doukas, and I. Maglogiannis. “Bringing IoT and cloud computing towards pervasive healthcare.” In *Innovative Mobile and Internet Services in Ubiquitous Computing (IMIS), 2012 Sixth International Conference on*, pp. 922-926. IEEE, 2012.

[40] L. Catarinucci, D.D. Donno, L. Mainetti, L. Palano, L. Patrono, M. L. Stefanizzi, and L. Tarricone. “An IoT-aware architecture for smart healthcare systems.” *IEEE IoT J.*, vol. 2, no. 6, pp. 515-526, 2015.

[41] P. Gope, and T. Hwang. “BSN-Care: A secure IoT-based modern healthcare system using body sensor network.” *IEEE Sens. J.*, vol. 16, no. 5, pp. 1368-1376, 2016.

[42] S. Sharma, K. Chen, and A. Sheth. “Toward practical privacy-preserving analytics for iot and cloud-based healthcare systems.” *IEEE Internet Comput.,* vol. 22, no. 2, pp. 42-51, 2018.

[43] P. J. Chen, D. C. Rodger, S. Saati, M. S. Humayun, and Y. C. Tai, “Microfabricated implantable parylene-based wireless passive intraocular pressure sensors.” *J. Microelectromech. Syst*., vol. 17, no. 6, pp. 1342-1351, Dec. 2008.

[44] C. Li, D. C. Rodger, S. Saati, M. S. Humayun, and Y. C. Tai, “A noncontact wireless passive radio frequency (RF) resonant pressure sensor with optimized design for applications in high-temperature environments.” *Meas. Sci. Technol*., vol. 25, no. 7, pp. 075101, May. 2014.

[45] Q. Tan, T. Luo, J. Xiong, H. Kang, X. Ji, Y. Zhang, M. Yang, X. Wang, C. Xue, J. Liu, and W. Zhang, “A harsh environment-oriented wireless passive temperature sensor realized by LTCC technology.” *Sensors*, vol. 14, no. 3, pp. 4154-4166, Mar. 2014.

[46] H. Kairm, D. Delfin, M. A. I. Shuvo, L. A. Chavez, C. R. Garcia, J. H. Barton, S. M. Gaytan, M. A. Cadena, R. C. Rumpf, R. B. Wicker, and Y. Lin, “Concept and model of a metamaterial-based passive wireless temperature sensor for harsh environment applications.” *IEEE Sens. J.,* vol. 15, no. 3, pp. 1445-1452, Mar. 2015.

[47] C. Li, Q. Tan, C. Xue, W. Zhang, Y. Li, and J. Xiong, “A high-performance LC wireless passive pressure sensor fabricated using Low-Temperature Co-Fired Ceramic (LTCC) technology.” *Sensors*, vol. 14, no. 12, pp. 23337-23347, Dec. 2014.

[48] P. J. Chen, S. Saati, R. Varma, M. S. Humayun, and Y. C. Tai, “Wireless intraocular pressure sensing using microfabricated minimally invasive flexible-coiled LC sensor implant.” *J. Microelectromech. Syst*., vol. 19, no. 4, pp. 721-734, Aug. 2010.

[49] U. Kawoos, X. Meng, M. Tofighi, and A. Rosen, “Too much pressure: Wireless intracranial pressure monitoring and its application in traumatic brain injuries.” *IEEE Microwave Mag*., vol. 16, no. 2, pp. 39-53, Mar. 2015.

[50] E. Silavwe, N. Somjit, and I. D. Robertson, "A Microfluidic-Integrated SIW Lab-on-Substrate Sensor for Microliter Liquid Characterization." *IEEE Sens. J.*, vol. 16, no. 21, pp. 7628-7635, Nov. 2016.

[51] Q. Y. Ren, L. F. Wang, J. Q. Huang, C. Zhang, and Q. A. Huang, "Simultaneous remote sensing of temperature and humidity by LC-type passive wireless sensors." *J. Microelectromech. Syst.*, vol. 24, no. 4, pp. 1117-1123, Aug. 2015.

[52] X. Wang, O. Larsson, D. Platt, S. Nordlinder, I. Engquist, M. Berggren, and X. Crispin, "An all-printed wireless humidity sensor label." *Sens. Actuators*, B, vol. 166, pp. 556-561, May. 2012.

[53] Y. Peng, B. F. Rahman, T. Wang, G. Wang, X. Liu, and X. Wen, "Characterization of a passive telemetric system for ISM band pressure sensors." *J. Electron. Test.*, vol. 30, no. 6, pp. 665-671, Dec. 2014.

[54] Q. Li, L. Chen, M. Li, Sh.L. Shaw, and A. Nüchter. "A sensor-fusion drivable-region and lane-detection system for autonomous vehicle navigation in challenging road scenarios." *IEEE Trans. Veh. Technol.*, vol. 63, no. 2, pp. 540-555, 2014.

[55] J.C. Kinsey, R.M. Eustice, and L.L. Whitcomb. "A survey of underwater vehicle navigation: Recent advances and new challenges." In *IFAC Conference of Manoeuvering and Control of Marine Craft*, vol. 88, pp. 1-12. 2006.

[56] P.A. Miller, J.A. Farrell, Y. Zhao, and V. Djapic. "Autonomous underwater vehicle navigation." *IEEE J. Oceanic Eng.*, vol. 35, no. 3, pp. 663-678, 2010.

[57] D. Yuan, L. Cai, M. Li, Ch. Liang, and X. Hou. "Multi-Sensor Integration Based on a New Quantum Neural Network Model for Land-Vehicle Navigation." *NeuroQuantology*, vol. 16, no. 6, 2018.

[58] A. Wichmann, T. Korkmaz, and A. S. Tosun. "Robot control strategies for task allocation with connectivity constraints in wireless sensor and robot networks." *IEEE Trans. Mob. Comput.*, vol. 17, no. 6, pp. 1429-1441, 2018.

[59] J.I. Furukawa, T. Noda, T. Teramae, and J. Morimoto. "Human movement modeling to detect biosignal sensor failures for myoelectric assistive robot control." *IEEE Trans. Rob.*, vol. 33, no. 4, pp. 846-857, 2017.

[60] M. Schwager, Ph. Dames, D. Rus, and V. Kumar. "A multi-robot control policy for information gathering in the presence of unknown hazards." In *Robotics research*, pp. 455-472. Springer, Cham, 2017.

[61] A. Magassouba, N. Bertin, and F. Chaumette. "Aural servo: sensor-based control from robot audition." *IEEE Trans. Rob.*, 2018.

[62] B. Gerkey, R.T. Vaughan, and A. Howard. "The player/stage project: Tools for multi-robot and distributed sensor systems." In *Proceedings of the 11th international conference on advanced robotics*, vol. 1, pp. 317-323. 2003.

[63] L.E.E.E. Weiss, A. R. T. H. U. R. C. Sanderson, and C. H. A. R. L. E. S. P. Neuman. "Dynamic sensor-based control of robots with visual feedback." *IEEE J. Rob. Autom.*, vol. 3, no. 5, pp. 404-417, 1987.

[64] G.J. Pottie, and W.J. Kaiser. "Wireless integrated network sensors." *Commun. ACM*, vol. 43, no. 5, pp. 51-58, 2000.

[65] F. Leccese, "Remote-control system of high efficiency and intelligent street lighting using a ZigBee network of devices and sensors." *IEEE Trans. Power Delivery*, vol. 28, no. 1, pp. 21-28, 2013.

[66] D. Pickem, P. Glotfelter, L. Wang, M. Mote, A. Ames, E. Feron, and M. Egerstedt. "The Robotarium: A remotely accessible swarm robotics research testbed." In *Robotics and Automation (ICRA), 2017 IEEE International Conference on*, pp. 1699-1706. IEEE, 2017.

[67] G.Zh. Yang, and G. Yang. *Body sensor networks*. vol. 1. London: Springer, 2006.

[68] H. Kudo, T. Sawada, E. Kazawa, H. Yoshida, Y. Iwasaki, and K. Mitsubayashi. "A flexible and wearable glucose sensor based on functional polymers with Soft-MEMS techniques." *Biosens. Bioelectron.,* vol. 22, no. 4, pp. 558-562, 2006.

[69] C.M.N Brigante, N. Abbate, A. Basile, A.C. Faulisi, and S. Sessa. "Towards miniaturization of a MEMS-based wearable motion capture system." *IEEE Trans. Ind. Electron.,* vol. 58, no. 8, pp. 3234-3241, 2011.

[70] W. Honda, Sh. Harada, T. Arie, S. Akita, and K. Takei. "Wearable, human-interactive, health-monitoring, wireless devices fabricated by macroscale printing techniques." *Adv. Func. Mater.,* vol. 24, no. 22, pp. 3299-3304, 2014.

[71] H. Cao, V. Leung, C. Chow, and H. Chan. "Enabling technologies for wireless body area networks: A survey and outlook." *IEEE Commun. Mag.,* vol. 47, no. 12, 2009.

[72] Z. Wang, V. Leonov, P. Fiorini, and Ch.V. Hoof. "Realization of a wearable miniaturized thermoelectric generator for human body applications." *Sens. Actuators A,* vol. 156, no. 1, pp. 95-102, 2009.

[73] K. Martinez, R. Ong, and J. Hart. "Glacsweb: a sensor network for hostile environments." In *Sensor and Ad Hoc Communications and Networks, 2004. IEEE SECON 2004. 2004 First Annual IEEE Communications Society Conference on*, pp. 81-87. IEEE, 2004.

[74] I.F. Akyildiz, W. Su, Y. Sankarasubramaniam, and E. Cayirci. "Wireless sensor networks: a survey." *Comput. Networks,* vol. 38, no. 4, pp. 393-422, 2002.

[75] S.D. Muruganathan, D.CF. Ma, R.I. Bhasin, and A. O. Fapojuwo. "A centralized energy-efficient routing protocol for wireless sensor networks." *IEEE Commun. Mag.,* vol. 43, no. 3, pp. S8-13, 2005.

[76] Ch.Y. Chong, and S. P. Kumar. "Sensor networks: evolution, opportunities, and challenges." *Proc. IEEE,* vol. 91, no. 8, pp. 1247-1256, 2003.

[77] S. Preradovic, N. C. Karmakar, and I. Balbin. "RFID transponders." *IEEE Microwave Mag.,* vol. 9, no. 5 2008.

[78] B.L.R Stojkoska, and K.V. Trivodaliev. "A review of Internet of Things for smart home: Challenges and solutions." *J. Cleaner Prod,* vol. 140, pp. 1454-1464, 2017.

[79] A. Dorri, S.S. Kanhere, R. Jurdak, and P. Gauravaram, 2017, March. Blockchain for IoT security and privacy: The case study of a smart home. In *Pervasive Computing and Communications Workshops (PerCom Workshops), 2017 IEEE International Conference on* (pp. 618-623).

[80] Ch. Perera, A. Zaslavsky, P. Christen, and D. Georgakopoulos. "Sensing as a service model for smart cities supported by internet of things." *Trans. Emerging Telecommun. Technol.,* vol. 25, no. 1, pp. 81-93, 2014.

[81] X. Li, R. Lu, X. Liang, X. Shen, J. Chen, and X. Lin. "Smart community: an internet of things application." *IEEE Commun. Mag.,* vol. 49, no. 11, 2011.

[82] A. Zanella, N. Bui, A. Castellani, L. Vangelista, and M. Zorzi. "Internet of things for smart cities." *IEEE IoT J.,* vol. 1, no. 1, pp. 22-32, 2014.

[83] J. Jin, J. Gubbi, S. Marusic, and M. Palaniswami. "An information framework for creating a smart city through internet of things." *IEEE IoT J.,* vol. 1, no. 2, pp. 112-121, 2014.

[84] P. Vlacheas, R. Giaffreda, V. Stavroulaki, D. Kelaidonis, V. Foteinos, G. Poulios, P. Demestichas, A. Somov, A. R. Biswas, and K. Moessner. "Enabling smart cities through a cognitive management framework for the internet of things." *IEEE Commun. Mag.,* vol. 51, no. 6, pp. 102-111, 2013.

[85] O. Vermesan, and P. Friess, eds. *Internet of things: converging technologies for smart environments and integrated ecosystems*. River Publishers, 2013.

[86] L. Tan, and N. Wang. "Future internet: The internet of things." In *Advanced Computer Theory and Engineering (ICACTE), 2010 3rd International Conference on*, vol. 5, pp. V5-376. IEEE, 2010.

[87] G.J. Mazzaro, A. F. Martone, K. I. Ranney, and R. M. Narayanan. "Nonlinear radar for finding rf electronics: System design and recent advancements." *IEEE Trans. Microwave Theory Tech.,* vol. 65, no. 5, pp. 1716-1726, 2017.

[88] R. Hstger. "Harmonic radar systems for near-ground in-foliage nonlinear scatterers." *IEEE Trans. Aerosp. Electron. Syst.,* vol. 2, pp. 230-245, 1976.

[89] F. Crowne, and Ch. Fazi. "Nonlinear radar signatures from metal surfaces." In *Radar Conference-Surveillance for a Safer World, 2009. RADAR. International*, pp. 1-6. IEEE, 2009.

[90] K.A. Gallagher, G. J. Mazzaro, K. I. Ranney, L. H. Nguyen, A. F. Martone, K. D. Sherbondy, and R. M. Narayanan. "Nonlinear synthetic aperture radar imaging using a harmonic radar." In *Radar Sensor Technology XIX; and Active and Passive Signatures VI*, vol. 9461, p. 946109. International Society for Optics and Photonics, 2015.

[91] K. Ranney, K. Gallagher, A. Martone, G. Mazzaro, K. Sherbondy, and R. Narayanan. "Instantaneous, stepped-frequency, nonlinear radar." In *Radar Sensor Technology XIX; and Active and Passive Signatures VI*, vol. 9461, p. 946122. International Society for Optics and Photonics, 2015.

[92] G. J. Mazzaro, A. F. Martone, and D. M. McNamara. "Detection of RF electronics by multitone harmonic radar." *IEEE Trans. Aerosp. Electron. Syst.,* vol. 50, no. 1, pp. 477-490, 2014.

[93] H. Aniktar, D. Baran, E. Karav, E. Akkaya, Y. S. Birecik, and M. Sezgin. "Getting the bugs out: A portable harmonic radar system for electronic countersurveillance applications." *IEEE Microwave Mag.,* vol. 16, no. 10, pp. 40-52, 2015.

[94] B. G. Colpitts, and G. Boiteau. "Harmonic radar transceiver design: miniature tags for insect tracking." *IEEE Trans. Antennas Propag.,* vol. 52, no. 11, pp. 2825-2832, 2004.

[95] D. Milanesio, M. Saccani, R. Maggiora, D. Laurino, and M. Porporato. "Design of an harmonic radar for the tracking of the A sian yellow-legged hornet." *Ecol. Evol.,* vol. 6, no. 7, pp. 2170-2178, 2016.

[96] L. Chioukh, H. Boutayeb, D. Deslandes, and K. Wu. "Noise and sensitivity of harmonic radar architecture for remote sensing and detection of vital signs." *IEEE Trans. Microwave Theory Tech.,* vol. 62, no. 9, pp. 1847-1855, 2014.

[97] M. Hajizadegan, M. Sakhdari, L. Zhu, Q. Cui, H. Huang, M. M. Cheng, J. CH. Hung, and P.Y. Chen. "Graphene Sensing Modulator: Toward Low-Noise, Self-Powered Wireless Microsensors." *IEEE Sens. J.* vol. 17, no. 22, pp. 7239-7247, 2017.

[98] B. Kubina, J. Romeu, C. Mandel, M. Schüßler, and R. Jakoby. "Quasi-chipless wireless temperature sensor based on harmonic radar." *Electron. Lett.,* vol. 50, no. 2, pp. 86-88, 2014.

[99] A. K. Geim and K. S. Novoselov, "The rise of graphene," *Nature Mater*., vol. 6, no. 3, pp. 183–191, 2007.

[100] K. S. Novoselov et al., "Electric field effect in atomically thin carbon films," *Science*, vol. 306, no. 5696, pp. 666–669, 2004.

[101] D.-W. Shin et al., "A facile route to recover intrinsic graphene over large scale," *ACS Na*no, vol. 6, no. 9, pp. 7781–7788, 2012.

[102] H. Wang, Y. Wu, C. Cong, J. Shang, and T. Yu, "Hysteresis of electronic transport in graphene transistors," *ACS Nano*, vol. 4, no. 12, pp. 7221–7228, 2010.

[103] M. Lafkioti et al., "Graphene on a hydrophobic substrate: Doping reduction and hysteresis suppression under ambient conditions," *Nano Lett.*, vol. 10, no. 4, pp. 1149–1153, 2010.

[104] P. L. Levesque et al., "Probing charge transfer at surfaces using graphene transistors," *Nano Lett.*, vol. 11, no. 1, pp. 132–137, 2011.

[105] P. G. Collins, K. Bradley, M. Ishigami, and A. Zettl, "Extreme oxygen sensitivity of electronic properties of carbon nanotubes," *Science*, vol. 287, pp. 1801–1804, Mar. 2000.

[106] J. Kong et al., "Nanotube molecular wires as chemical sensors," *Science*, vol. 287, no. 5453, pp. 622–625, 2000.

[107] M. S. Mannoor et al., "Graphene-based wireless bacteria detection on tooth enamel," *Nature Commun.*, vol. 3, p. 763, Mar. 2012.

[108] F. Schedin et al., "Detection of individual gas molecules adsorbed on graphene," *Nature Mater.*, vol. 6, pp. 652–655, Jul. 2007.

[109] C. A. Merchant et al., "DNA translocation through graphene nanopores," *Nano Lett.*, vol. 10, pp. 2915–2921, Jul. 2010.

[110] P. Y. Chen and J. Jung, "PT symmetry and singularity-enhanced sensing based on photoexcited graphene metasurfaces," *Phys. Rev. Appl.*, vol. 5, p. 064018, Jun. 2016.

[111] P. Y. Chen and A. Alù, "Atomically thin surface cloak using graphene monolayers," *ACS Nano*, vol. 5, pp. 5855–5863, Jun. 2011.

[112] P.-Y. Chen and A. Alu, "Terahertz metamaterial devices based on graphene nanostructures," *IEEE Trans. THz Sci. Technol.*, vol. 3, no. 6, pp. 748–756, Nov. 2013.

[113] P. Y. Chen, H. Huang, D. Akinwande, and A. Alù, "Graphene-based plasmonic platform for reconfigurable terahertz nanodevices," *ACS Photon.*, vol. 1, no. 8, pp. 647–654, 2014.

[114] C. Yu *et al.*, "Quasi-free-standing bilayer epitaxial graphene field-effect transistors on 4H-SiC (0001) substrates," *Appl. Phys. Lett.*, vol. 108, no. 1, p. 013102, 2016.

[115] H. Wang, A. Hsu, K. K. Kim, J. Kong, and T. Palacios, "Gigahertz ambipolar frequency multiplier based on CVD graphene," in *IEDM Tech. Dig.*, vol. 1, Dec. 2010, pp. 572–575.

[116] M. E. Ramon *et al.*, "Three-gigahertz graphene frequency doubler on quartz operating beyond the transit frequency," *IEEE Trans. Nanotechnol.*, vol. 11, no. 5, pp. 877–883, Sep. 2012.

[117] H. Wang, D. Nezich, J. Kong, and T. Palacios, "Graphene frequency multipliers," *IEEE Electron Device Lett.*, vol. 30, no. 5, pp. 547–549, May 2009.

[118] K. N. Parrish and D. Akinwande, "Even-odd symmetry and the conversion efficiency of ideal and practical graphene transistor frequency multipliers," *Appl. Phys. Lett.*, vol. 99, no. 22, p. 223512, 2011.

[119] Z. Wang, Z. Zhang, H. Xu, L. Ding, S. Wang, and L. M. Peng, "A highperformance top-gate graphene field-effect transistor based frequency doubler," *Appl. Phys. Lett.*, vol. 96, no. 17, pp. 17–19, 2010.

[120] Y. Wu *et al.*, "High-frequency, scaled graphene transistors on diamondlike carbon," *Nature*, vol. 472, pp. 74–78, Apr. 2011.

[121] H. Huang *et al.*, "Chemical-sensitive graphene modulator with a memory effect for Internet-of-Things applications," *Microsyst. Nanoeng.*, vol. 2, p. 15049, May 2016.

[122] A. Shahini, M. Hajizadegan, M. Sakhdari, M. M. C. Cheng, P. Y. Chen, and H. H. Huang, "Self-powered and transparent all-graphene biosensor," in *Proc. IEEE SENSORS*, Oct. 2016, pp. 1–3.

[123] M. Peplow, "Graphene: the quest for supercarbon." *Nature News*, vol. 503, no. 7476, p. 327, 2013.

[124] H. Wang, A. L. Hsu, and T. Palacios. "Graphene electronics for RF applications." *IEEE Microwave Mag.*, vol. 13, no. 4, pp. 114-125, 2012.

[125] K. S. Novoselov, A. K. Geim, S. V. Morozov, D. Jiang, M. I. Katsnelson, I. V. Grigorieva, S. V. Dubonos, and A. A. Firsov, "Two-dimensional gas of massless Dirac fermions in graphene," *Nature*, vol. 438, no. 7065, pp. 197–200, Nov. 2005.

[126] R. Martel, V. Derycke, C. Lavoie, J. Appenzeller, K. K. Chan, J. Tersoff, and Ph. Avouris, "Ambipolar electrical transport in semiconducting single-wall carbon nanotubes," *Phys. Rev. Lett.*, vol. 87, no. 25, p. 256805, Dec. 2001.

[127] G. W. Neudeck, H. F. Bare, and K. Y. Chung, "Modeling of ambipolar a-Si:H thin-film transistors," *IEEE Trans. Electron Devices*, vol. 34, no. 2, pp. 344–350, Feb. 1987.

[128] A. Dodabalapur, H. E. Katz, L. Torsi, and R. C. Haddon, "Organic heterostructure field-effect transistors," *Science*, vol. 269, no. 5230, pp. 1560–1562, 1995.

[129] S. Lee, K. Lee, Ch. H. Liu, G. S. Kulkarni, and Zh. Zhong. "Flexible and transparent all-graphene circuits for quaternary digital modulations." *Nature communications* 3 (2012): 1018.

[130] C. Berger, Z. Song, X. Li, X. Wu, N. Brown, C. Naud, D. Mayou, T. Li, J. Hass, A. N. Marchenkov, E. H. Conrad, P. N. First, and W. A. de Heer, "Electronic confinement and coherence in patterned epitaxial graphene," *Science*, vol. 312, no. 5777, pp. 1191–1196, May 2006.

[131] A. Reina, X. Jia, J. Ho, D. Nezich, H. Son, V. Bulovic, M. S. Dresselhaus, and J. Kong, "Large area, few-layer graphene films on arbitrary substrates by chemical vapor deposition," *Nano Lett.*, vol. 9, no. 1, pp. 30–35, Jan. 2009.

[132] X. Li, W. Cai, J. An, S. Kim, J. Nah, D. Yang, R. Piner, A. Velamakanni, I. Jung, E. Tutuc, S. K. Banerjee, L. Colombo, and R. S. Ruoff, "Large-area synthesis of high-quality and uniform graphene films on copper foils," *Science*, vol. 324, no. 5932, pp. 1312–1314, June 2009.

[133] S. Bae, H. Kim, Y. Lee, X. Xu, J.-S. Park, Y. Zheng, J. Balakrishnan, T. Lei, H. R. Kim, Y. I. Song, Y.-J. Kim, K. S. Kim, B. Ozyilmaz, J.-H. Ahn, B. H. Hong, and S. Iijima, "Roll-to-roll production of 30-inch graphene films for transparent electrodes," *Nat. Nanotechnol.*, vol. 5, no. 8, pp. 574–578, 2010.

[134] M. Hajizadegan, M. Sakhdari, and P.Y. Chen, "*High-sensitivity wireless displacement sensing enabled by PT-symmetric telemetry."* IEEE Transactions on Antennas & Propagation, vol. 67, 3445-3449, 2019.

[135] P.Y. Chen, M. Sakhdari, M. Hajizadegan, et al., "*Generalized Parity-Time symmetry condition for enhanced sensor telemetry.*" Nature Electronics, vol. 1, No. 5, p. 297, 2018.

[136] M. Sakhdari, M. Hajizadegan, Y. Li, M.M. Cheng, Jonathan C. H. Hung, P.Y. Chen, "*Ultrasensitive, parity-time symmetric wireless reactive and resistive sensors.*" IEEE Sensors Journal, vol. 18, No. 23, pp. 9548-9555, 2018.

[137] Bhimanapati, Ganesh R., Zhong Lin, Vincent Meunier, Yeonwoong Jung, Judy Cha, Saptarshi Das, Di Xiao et al. "Recent advances in two-dimensional materials beyond graphene." *ACS nano* 9, no. 12 (2015): 11509-11539.

[138] Donnelly, Matthew, Dacheng Mao, Junsu Park, and Guangyu Xu. "Graphene field-effect transistors: the road to bioelectronics." *Journal of Physics D: Applied Physics* 51, no. 49 (2018): 493001.

[139] Wang, Han, Allen Hsu, Benjamin Mailly, Ki Kang Kim, Jing Kong, and Tomas Palacios. "Towards ubiquitous RF electronics based on graphene." In *2012 IEEE/MTT-S International Microwave Symposium Digest*, pp. 1-3. IEEE, 2012.

[140] Wang, Zhenxing, Zhiyong Zhang, Huilong Xu, Li Ding, Sheng Wang, and Lian-Mao Peng. "A high-performance top-gate graphene field-effect transistor based frequency doubler." *Applied Physics Letters* 96, no. 17 (2010): 173104.

[141] Han, Shu-Jen, Keith A. Jenkins, Alberto Valdes Garcia, Aaron D. Franklin, Ageeth A. Bol, and Wilfried Haensch. "High-frequency graphene voltage amplifier." *Nano letters* 11, no. 9 (2011): 3690-3693.

[142] Yang, Xuebei, Guanxiong Liu, Masoud Rostami, Alexander A. Balandin, and Kartik Mohanram. "Graphene ambipolar multiplier phase detector." *IEEE Electron Device Letters* 32, no. 10 (2011): 1328-1330.

[143] Yang, Xuebei, Guanxiong Liu, Alexander A. Balandin, and Kartik Mohanram. "Triple-mode single-transistor graphene amplifier and its applications." *ACS nano* 4, no. 10 (2010): 5532-5538.

[144] Wang, Han, Allen Hsu, Justin Wu, Jing Kong, and Tomas Palacios. "Graphene-based ambipolar RF mixers." *IEEE Electron Device Letters* 31, no. 9 (2010): 906-908.

[145] Yap, Yoke Khin, and Zhixian Zhou, eds. *Two-Dimensional Electronics and Optoelectronics*. MDPI, 2018.

[146] *Lin, Y.-M. et al. 100 GHz transistors from wafer-scale epitaxial graphene. Science 327, 662 (2010).*

[147] *Liao, L. et al. High-speed graphene transistors with a self-aligned nanowire gate. Nature 467, 305–308 (2010).*

[148] *Proakis JG, Salehi M. Communication Systems Engineering, 2nd edn, 2001. Prentice Hall, Upper Saddle River, New Jersey, 07458.*

[149] *Rappaport TS. Wireless Communications: Principles and Practice, 2nd edn, 2002. Prentice Hall, Upper Saddle River, New Jersey, 07458.*

[150] Mao, Shun, Jingbo Chang, Haihui Pu, Ganhua Lu, Qiyuan He, Hua Zhang, and Junhong Chen. "Two-dimensional nanomaterial-based field-effect transistors for chemical and biological sensing." *Chemical Society Reviews* 46, no. 22 (2017): 6872-6904.

[151] Schroter, M., M. Claus, P. Sakalas, D. Wang, and M. Haferlach. "An overview on the state-of-the-art of carbon-based radio-frequency electronics." In *2012 IEEE Bipolar/BiCMOS Circuits and Technology Meeting (BCTM)*, pp. 1-8. IEEE, 2012.

[152] Baumgardner, James E., Aaron A. Pesetski, James M. Murduck, John X. Przybysz, John D. Adam, and Hong Zhang. "Inherent linearity in carbon nanotube field-effect transistors." *Applied Physics Letters* 91, no. 5 (2007): 052107.

[153] Lin, Yu-Ming, Keith A. Jenkins, Alberto Valdes-Garcia, Joshua P. Small, Damon B. Farmer, and Phaedon Avouris. "Operation of graphene transistors at gigahertz frequencies." *Nano letters* 9, no. 1 (2008): 422-426.

[154] Di Bartolomeo, Antonio, Filippo Giubileo, Francesco Romeo, Paolo Sabatino, Giovanni Carapella, Laura Iemmo, Thomas Schroeder, and Grzegorz Lupina. "Graphene field effect transistors with niobium contacts and asymmetric transfer characteristics." *Nanotechnology* 26, no. 47 (2015): 475202.

[155] Park, Saungeun, Weinan Zhu, Hsiao-Yu Chang, Maruthi N. Yogeesh, Rudresh Ghosh, Sanjay K. Banerjee, and Deji Akinwande. "High-frequency prospects of 2D nanomaterials for flexible nanoelectronics from baseband to sub-THz devices." In *2015 IEEE International Electron Devices Meeting (IEDM)*, pp. 32-1. IEEE, 2015.

[156] Li, Song-Lin, Hisao Miyazaki, Hidefumi Hiura, Chuan Liu, and Kazuhito Tsukagoshi. "Enhanced logic performance with semiconducting bilayer graphene channels." *ACS nano* 5, no. 1 (2010): 500-506.

[157] Yogeesh, Maruthi, Hsiao-Yu Chang, Wei Li, Somayyeh Rahimi, Amritesh Rai, Atresh Sanne, Rudresh Ghosh, Sanjay K. Banerjee, and Deji Akinwande. "Towards wafer scale monolayer MoS 2 based flexible low-power RF electronics for IoT systems." In *2016 74th Annual Device Research Conference (DRC)*, pp. 1-2. IEEE, 2016.

[158] Yogeesh, Maruthi N., Atresh Sanne, Saungeun Park, Hsiao-Yu Chang, Rudresh Ghosh, Sanjay K. Banerjee, and Deji Akinwande. "State-of-the-art large area CVD MoS 2 based RF electronics." In *2016 3rd International Conference on Emerging Electronics (ICEE)*, pp. 1-3. IEEE, 2016.

[159] Chang, Hsiao-Yu, Maruthi Nagavalli Yogeesh, Rudresh Ghosh, Amritesh Rai, Atresh Sanne, Shixuan Yang, Nanshu Lu, Sanjay Kumar Banerjee, and Deji Akinwande. "Large-Area Monolayer MoS2 for Flexible Low-Power RF Nanoelectronics in the GHz Regime." *Advanced Materials* 28, no. 9 (2016): 1818-1823.

[160] Ameri, Shideh Kabiri, Myungsoo Kim, Irene Agnes Kuang, Withanage K. Perera, Mohammed Alshiekh, Hyoyoung Jeong, Ufuk Topcu, Deji Akinwande, and Nanshu Lu. "Imperceptible electrooculography graphene sensor system for human–robot interface." *npj 2D Materials and Applications* 2, no. 1 (2018): 19.

[161] Kim, Myungsoo, Saungeun Park, Atresh Sanne, Sanjay Kumar Banerjee, and Deji Akinwande. "Towards mm-wave nanoelectronics and RF switches using MoS 2 2D Semiconductor." In *2018 IEEE/MTT-S International Microwave Symposium-IMS*, pp. 352-354. IEEE, 2018.

[162] Kim, Myungsoo, Ruijing Ge, Xiaohan Wu, Xing Lan, Jesse Tice, Jack C. Lee, and Deji Akinwande. "Zero-static power radio-frequency switches based on MoS 2 atomristors." *Nature communications* 9, no. 1 (2018): 2524.

[163] Zhu, Weinan, Saungeun Park, Maruthi N. Yogeesh, and Deji Akinwande. "Advancements in 2D flexible nanoelectronics: From material perspectives to RF applications." *Flexible and Printed Electronics* 2, no. 4 (2017): 043001.

[164] Ghorbani-Asl, Mahdi, Agnieszka Kuc, Pere Miró, and Thomas Heine. "A Single-Material Logical Junction Based on 2D Crystal PdS2." *Advanced Materials* 28, no. 5 (2016): 853-856.

[165] Lin, Yu-Ming, Alberto Valdes-Garcia, Shu-Jen Han, Damon B. Farmer, Inanc Meric, Yanning Sun, Yanqing Wu et al. "Wafer-scale graphene integrated circuit." *Science* 332, no. 6035 (2011): 1294-1297.

[166] Huang, Jing-Kai, Jiang Pu, Chang-Lung Hsu, Ming-Hui Chiu, Zhen-Yu Juang, Yung-Huang Chang, Wen-Hao Chang, Yoshihiro Iwasa, Taishi Takenobu, and Lain-Jong Li. "Large-area synthesis of highly crystalline WSe2 monolayers and device applications." *ACS nano* 8, no. 1 (2013): 923-930.

[167] Das, Saptarshi, Marcel Demarteau, and Andreas Roelofs. "Ambipolar phosphorene field effect transistor." *ACS nano* 8, no. 11 (2014): 11730-11738.

[168] Li, Likai, Yijun Yu, Guo Jun Ye, Qingqin Ge, Xuedong Ou, Hua Wu, Donglai Feng, Xian Hui Chen, and Yuanbo Zhang. "Black phosphorus field-effect transistors." *Nature nanotechnology* 9, no. 5 (2014): 372.

[169] Carvalho, Alexandra, Min Wang, Xi Zhu, Aleksandr S. Rodin, Haibin Su, and Antonio H. Castro Neto. "Phosphorene: from theory to applications." *Nature Reviews Materials* 1, no. 11 (2016): 16061.

[170] Wang, Han, Xiaomu Wang, Fengnian Xia, Luhao Wang, Hao Jiang, Qiangfei Xia, Matthew L. Chin, Madan Dubey, and Shu-jen Han. "Black phosphorus radio-frequency transistors." *Nano letters* 14, no. 11 (2014): 6424-6429.

[171] Lin, Y-M., Christos Dimitrakopoulos, Keith A. Jenkins, Damon B. Farmer, H-Y. Chiu, Alfred Grill, and Ph Avouris. "100-GHz transistors from wafer-scale epitaxial graphene." *Science* 327, no. 5966 (2010): 662-662.

[172] Lee, Jongho, Tae-Jun Ha, Huifeng Li, Kristen N. Parrish, Milo Holt, Ananth Dodabalapur, Rodney S. Ruoff, and Deji Akinwande. "25 GHz embedded-gate graphene transistors with high-K dielectrics on extremely flexible plastic sheets." *ACS nano* 7, no. 9 (2013): 7744-7750.

[173] Yoon, Youngki, Kartik Ganapathi, and Sayeef Salahuddin. "How good can monolayer MoS2 transistors be?." *Nano letters* 11, no. 9 (2011): 3768-3773.

[174] Cheng, Rui, Shan Jiang, Yu Chen, Yuan Liu, Nathan Weiss, Hung-Chieh Cheng, Hao Wu, Yu Huang, and Xiangfeng Duan. "Few-layer molybdenum disulfide transistors and circuits for high-speed flexible electronics." *Nature communications* 5 (2014): 5143.

[175] Barreiro, Amelia, Michele Lazzeri, Joel Moser, Francesco Mauri, and Adrian Bachtold. "Transport properties of graphene in the high-current limit." *Physical review letters* 103, no. 7 (2009): 076601.

[176] Baumgardner, James E., Aaron A. Pesetski, James M. Murduck, John X. Przybysz, John D. Adam, and Hong Zhang. "Inherent linearity in carbon nanotube field-effect transistors." *Applied Physics Letters* 91, no. 5 (2007): 052107.

[177] Guo, Zelei, Rui Dong, Partha Sarathi Chakraborty, Nelson Lourenco, James Palmer, Yike Hu, Ming Ruan et al. "Record maximum oscillation frequency in C-face epitaxial graphene transistors." *Nano letters* 13, no. 3 (2013): 942-947.

[178] Schroter, Michael, Martin Claus, Paulius Sakalas, M. Haferlach, and Dawei Wang. "Carbon nanotube FET technology for radio-frequency electronics: State-of-the-art overview." *IEEE Journal of the Electron Devices Society* 1, no. 1 (2013): 9-20.

[179] Krasnozhon, Daria, Dominik Lembke, Clemens Nyffeler, Yusuf Leblebici, and Andras Kis. "MoS2 transistors operating at gigahertz frequencies." *Nano letters* 14, no. 10 (2014): 5905-5911.

[180] Sanne, Atresh, Rudresh Ghosh, Amritesh Rai, Maruthi Nagavalli Yogeesh, Seung Heon Shin, Ankit Sharma, Karalee Jarvis et al. "Radio frequency transistors and circuits based on CVD MoS2." *Nano letters* 15, no. 8 (2015): 5039-5045.

[181] Radisavljevic, Branimir, Aleksandra Radenovic, Jacopo Brivio, Valentina Giacometti, and Andras Kis. "Single-layer MoS 2 transistors." *Nature nanotechnology* 6, no. 3 (2011): 147.

[182] Chang, Hsiao-Yu, Maruthi Nagavalli Yogeesh, Rudresh Ghosh, Amritesh Rai, Atresh Sanne, Shixuan Yang, Nanshu Lu, Sanjay Kumar Banerjee, and Deji Akinwande. "Large-Area Monolayer MoS2 for Flexible Low-Power RF Nanoelectronics in the GHz Regime." *Advanced Materials* 28, no. 9 (2016): 1818-1823.

[183] Zhang, Xu, Jesús Grajal, Jose Luis Vazquez-Roy, Ujwal Radhakrishna, Xiaoxue Wang, Winston Chern, Lin Zhou et al. "Two-dimensional MoS 2-enabled flexible rectenna for Wi-Fi-band wireless energy harvesting." *Nature* 566, no. 7744 (2019): 368.

[184] Akinwande, Deji, Nicholas Petrone, and James Hone. "Two-dimensional flexible nanoelectronics." *Nature communications* 5 (2014): 5678.

[185] Wu, Di, Wei Li, Amritesh Rai, Xiaoyu Wu, Hema CP Movva, Maruthi N. Yogeesh, Zhaodong Chu, Sanjay K. Banerjee, Deji Akinwande, and Keji Lai. "Visualization of Local Conductance in MoS2/WSe2 Heterostructure Transistors." *Nano letters* 19, no. 3 (2019): 1976-1981.

[186] Chamlagain, Bhim, Qingsong Cui, Sagar Paudel, Mark Ming-Cheng Cheng, Pai-Yen Chen, and Zhixian Zhou. "Thermally oxidized 2D TaS2 as a high-κ gate dielectric for MoS2 field-effect transistors." *2D Materials* 4, no. 3 (2017): 031002.

[187] Roy, Tania, Mahmut Tosun, Jeong Seuk Kang, Angada B. Sachid, Sujay B. Desai, Mark Hettick, Chenming C. Hu, and Ali Javey. "Field-effect transistors built from all two-dimensional material components." *ACS nano* 8, no. 6 (2014): 6259-6264.

[188] Liu, Tao, Song Liu, Kun-Hua Tu, Hennrik Schmidt, Leiqiang Chu, Du Xiang, Jens Martin, Goki Eda, Caroline A. Ross, and Slaven Garaj. "Crested two-dimensional transistors." *Nature nanotechnology* 14, no. 3 (2019): 223.

[189] Le T, Thai T, Lakafosis V et al. Graphene enhanced wireless sensors. IEEE Sensors 2012; 2012: 1–4.

[190] Graphene MA. Technologies, applications and markets. BCC Research Mark Forecast 2013. Available at: http://www.bccresearch.com/market-research/ advanced-materials/graphene-technologies-applications-markets-avm075c.html (accessed on 16 March 2016).

[191] Schwierz F. Electronics: industry-compatible graphene transistors. Nature 2011; 472: 41–42.

[192] Chen X, Lee K-J, Deji A et al. High-speed graphene interconnects monolithically integrated with CMOS ring oscillators operating at 1.3GHz. 2009 IEEE International Electron Devices Meeting (IEDM); 7–9 Dec 2009; Baltimore, MD, USA; 2009: 1–4.

[193] Akyildiz I, Jornet J. The Internet of nano-things. IEEE Wireless Communications 2010; 17: 58–63.

[194] Palacios T, Hsu A, Wang H. Applications of graphene devices in RF communications. IEEE Communication Magazine 2010; 48: 122–128.

[195] Cheng Z, Li Q, Li Z et al. Suspended graphene sensors with improved signal and reduced noise. Nano Letters 2010; 10: 1864–1868.

[196] Fowler JD, Allen MJ, Tung VC et al. Practical chemical sensors from chemically derived graphene. ACS Nano 2009; 3: 301–306.

[197] Dan Y, Lu Y, Kybert NJ et al. Intrinsic response of graphene vapor sensors. Nano Letters 2009; 9: 1472–1475.

[198] Ohno Y, Maehashi K, Yamashiro Y et al. Electrolyte-gated graphene field-effect transistors for detecting ph and protein adsorption. Nano Letters 2009; 9: 3318–3322.

[199] K. N. Parrish and D. Akinwande, "An exactly solvable model for the graphene transistor in the quantum capacitance limit," *Appl. Phys. Lett.*, vol. 101, no. 5, p. 053501, 2012.

[200] Tao L, Lee J, Chou H et al. Synthesis of high quality monolayer graphene at reduced temperature on hydrogen-enriched evaporated copper (111) films. ACS Nano 2012; 6: 2319–2325.

[201] Tao L, Lee J, Holt M et al. Uniform wafer-scale chemical vapor deposition of graphene on evaporated Cu (111) film with quality comparable to exfoliated monolayer. Journal of Physical Chemistry C 2012; 116: 24068–24074.

[202] Piner R, Li H, Kong X et al. Graphene synthesis via magnetic inductive heating of copper substrates. ACS Nano 2013; 7: 7495–7499.

[203] Tao L, Lee J, Li H et al. Inductively heated synthesized graphene with record transistor mobility on oxidized silicon substrates at room temperature. Applied Physics Letters 2013; 103: 183115.

[204] S. M. Sze, and K. K. Ng, *Physics of Semiconductor Devices*. Hoboken, NJ, USA: Wiley, 2006.

[205] J. Tian, A. Katsounaros, D. Smith, and Y. Hao, "Graphene field-effect transistor model with improved carrier mobility analysis," *IEEE Trans. Electron Devices*, vol. 62, no. 10, pp. 3433–3440, Oct. 2015.

[206] G. M. Landauer, D. Jímenez, and J. L. González, "An accurate and Verilog-A compatible compact model for graphene field-effect transistors," *IEEE Trans. Nanotechnol.*, vol. 13, no. 5, pp. 895–904, Sep. 2014.

[207] S. Wang, P. K. Ang, Z. Wang, A. L. L. Tang, J. T. Thong, and K. P. Loh, "High mobility, printable, and solution-processed graphene electronics," *Nano Lett.*, vol. 10, no. 1, pp. 92–98, 2009.

[208] W. Zhu, V. Perebeinos, M. Freitag, and P. Avouris, "Carrier scattering, mobilities, and electrostatic potential in monolayer, bilayer, and trilayer graphene," *Phys. Rev. B*, vol. 80, p. 235402, Dec. 2009.

[209] V. E. Dorgan, M. H. Bae, and E. Pop, "Mobility and saturation velocity in graphene on SiO2," *Appl. Phys. Lett.*, vol. 97, no. 8, p. 082112, 2010.

[210] J. Martin *et al.*, "Observation of electron-hole puddles in graphene using a scanning single-electron transistor," *Nature Phys.*, vol. 4, no. 2, pp. 144–148, 2008.

[211] S. A. Thiele, J. A. Schaefer, and F. Schwierz, "Modeling of graphene metal-oxide-semiconductor field-effect transistors with gapless large-area graphene channels," *J. Appl. Phys.*, vol. 107, no. 9, pp. 094505-1–094505-8, 2010.

[212] D. Jimenez and O. Moldovan, "Explicit drain-current model of graphene field-effect transistors targeting analog and radio-frequency applications," *IEEE Trans. Electron Devices*, vol. 58, no. 11, pp. 4049–4052, Nov. 2011

[213] T. Fang, A. Konar, H. Xing, and D. Jena, "Carrier statistics and quantum capacitance of graphene sheets and ribbons," *Appl. Phys. Lett.*, vol. 91, no. 9, p. 092109, 2007.

[214] *Advanced Design System*. [Online]. Available: http://www.keysight. com/en/pc-1297113/advanced-Design-System

[215] M. Hajizadegan, and P. Y. Chen, "*A self-powered harmonic sensor based on simple graphene circuit and hybrid-fed antenna*." In Antennas and Propagation & USNC/URSI National Radio Science Meeting, 2017 IEEE International Symposium on, pp. 581-582. IEEE, 2017.

[216] D. L. Poole, A. K. Mackworth, R. Goebel, *Computational intelligence: a logical approach*. (Oxford University Press New York, 1998), vol. 1.

[217] S. S. Haykin, S. S. Haykin, S. S. Haykin, S. S. Haykin, *Neural networks and learning machines*. (Pearson Upper Saddle River, NJ, USA:, 2009), vol. 3.

[218] A. K. Jain, J. Mao, and K. M. Mohiuddin, "Artificial neural networks: A tutorial," *Computer*, vol. 29, no. 3, pp. 31–44, Mar. 1996.

[219] N. Jones, "The learning machines," *Nature*, vol. 505, no. 7482, p. 146, 2014.

[220] D. H. Ballard, G. E. Hinton, and T. J. Sejnowski, "Parallel visual computation," *Nature*, vol. 306, pp. 21–26, Nov. 1983.

[221] P. R. Gray, and R. G. Meyer, *Analysis and Design of Analog Integrated Circuits*. Hoboken, NJ, USA: Wiley, 1990.

[222] M. Hagan, H. B. Demuth, M. H. Beale, O. D. Jess, and M. T. Hagan, *Neural Network Design*. Seattle, WA, USA: Amazon, 2014.

[223] R. Hecht-Nielsen, "Theory of the backpropagation neural network," *Neural Netw.*, vol. 1, pp. 445–448, Jan. 1988.

[224] C. Christodoulou and M. Georgiopoulos, *Applications of Neural Networks in Electromagnetics*. Norwood, MA, USA: Artech House, 2000.

[225] A. Patnaik and R. K. Mishra, "ANN techniques in microwave engineering," *IEEE Microw. Mag.*, vol. 1, no. 1, pp. 55–60, Mar. 2000.

[226] P. Y. Chen, C. H. Chen, and H. Wang, “A neural network: Family competition genetic algorithm and its applications in electromagnetic optimization,” *Appl. Comput. Intell. Soft Comput.*, p. 4, Jan. 2009.

[227] B. Razavi, “RF Microelectronics,” Microelectron. J. 29, 932–934 (2012).

[228] P. Y. Chen, C. Argyropoulos, and A. Alu, “Terahertz antenna phase shifters using integrally-gated graphene transmission-lines,” *IEEE Trans. Antennas Propag*., vol. 61, pp. 1528–1537, 2013.

[229] S. Gomez-Diaz and J. Perruisseau-Carrier, “Microwave to THz properties of graphene and potential antenna applications,” *In 2012 International Symposium on Antennas Propagation* (2012), pp. 239–242.

[230] S. G_omez-D_ıaz, J. Perruisseau-Carrier, P. Sharma, and A. Ionescu, “Non-contact characterization of graphene surface impedance at micro and millimeter waves,” *J. Appl. Phys*., vol. 111, p. 114908, 2012.

[231] See http://www.dailywireless.org/2012/08/09/fcc-more-backhaul-at-6-11-and- 23-ghz/ for “FCC: More Backhaul at 6, 11 and 23 GHzjdailywireless.org” (last accessed January 27, 2016).

[232] Y.-C. Chang, C.-H. Liu, C.-H. Liu, Z. Zhong, and T. B. Norris, “Midinfrared hyperbolic metamaterial based on graphene-dielectric multilayers,” *In 2015 Conference on Lasers and Electro-Optics* (*CLEO*) (IEEE, 2015), pp. 1–2.

[233] K. Wei, Z. Zhang, W. Chen, and Z. Feng, “A novel hybrid-fed patch antenna with pattern diversity,” *IEEE Antennas Wireless Propag. Lett.*, vol. 9, pp. 562–565, 2010.

[234] H. Y. Chen, and J. Appenzeller, “Graphene-based frequency tripler,” *Nano lett*., vol. 12, pp. 2067-2070, 2012.

[235] L. Yu-Te, Y. Huanfen, B. Parviz, and B. Otis, “A 3lW wirelessly powered CMOS glucose sensor for an active contact lens,” in 2011 IEEE International Solid-State Circuits Conference Digest of Technical Papers (ISSCC) (2011), pp. 38–40.

[236] Y. T. Liao, H. Yao, A. Lingley, B. Parviz, and B. P. Otis, “A 3lW CMOS glucose sensor for wireless contact-lens tear glucose monitoring,” IEEE J. Solid-State Circuits 47, 335–344 (2012).

[237] CST Microwave Studio: http://www.cst.com

[238] L. Zhu, N. Alkhaldi, H. M. Kadry, S. L. Liao, and P. Y. Chen, "A compact hybrid-fed microstrip antenna for harmonics-based radar and sensor system," *IEEE Antennas Wireless Propag. Lett.,* vol. 17, no. 12, pp. 2444-2448, 2018.

VITA

NAME: Mehdi Hajizadegan

EDUCATION: B.A., Electrical Engineering, Shahid Rajaei University, Tehran, IRAN, 2010

M.S., Electrical Engineering, Tarbiat Modares University, Tehran, IRAN, 2013

Ph.D., Electrical and Computer Engineering, University of Illinois at Chicago, IL, 2020

PUBLICATION: **M. Hajizadegan**, M. Sakhdari, and P.Y. Chen, "*High-sensitivity wireless displacement sensing enabled by PT-symmetric telemetry."* **IEEE Transactions on Antennas & Propagation**, vol. 67, No. 5, pp. 3445-3449, 2019.

M. Sakhdari, **M. Hajizadegan**, Q. Zhong, D. N. Christodoulides, R. El-Ganainy, and P. Y. Chen, "*Experimental observation of PT symmetry breaking near divergent exceptional points*." **Physical Review Letters**, vol. 123, No. 19, p. 193901, 2019.

P.Y. Chen, M. Sakhdari, **M. Hajizadegan**, et al., "*Generalized Parity-Time symmetry condition for enhanced sensor telemetry*." **Nature Electronics**, vol. 1, No. 5, p. 297, 2018.

M. Sakhdari, **M. Hajizadegan**, and P. Y. Chen, *"Robust extended-range wireless power transfer using a higher-order PT-symmetric platform"* **Physical Review Research**, vol. 2, No. 1, p. 013152, 2020.

M. Sakhdari, **M. Hajizadegan**, Y. Li, M.M. Cheng, Jonathan C. H. Hung, P.Y. Chen, "*Ultrasensitive, parity-time symmetric wireless reactive and resistive sensors.*" **IEEE Sensors Journal**, vol. 18, No. 23, pp. 9548-9555, 2018.

M. Hajizadegan, M. Sakhdari, and P.Y. Chen, "*Hyperbolic metamaterial-based plasmoelectronic nanodevices for detection and harvesting of infrared radiation*." **In Micro-and**

Nanotechnology Sensors, Systems, and Applications X, vol. 10639, p. 106390M. Int. Soc. Opt. Photonics, 2018.

M. Hajizadegan, M.Sakhdari, P.Y. Chen, and et al., "*Graphene sensing modulator: toward low-noise, self-powered wireless microsensors*." **IEEE Sensors Journal**, vol. 17, No. 22, p. 7239, 2017.

P. Y. Chen, **M. Hajizadegan**, M. Sakhdari, and A. Alù, "*Giant photoresponsivity of midinfrared hyperbolic metamaterials in the photon-assisted-tunneling regime*." **Physical Review Applied**, vol. 5, No. 4, p.041001, 2016.

H. H. Huang, M. Sakhdari, **M. Hajizadegan**, A. Shahini, D. Akinwande, and P. Y.Chen, "*Toward transparent and self-activated graphene harmonic transponder sensors*." **Applied Physics Letters**, vol.108, No.17, p.173503, 2016.

M. Sakhdari, **M. Hajizadegan**, M. Farhat, and P. Y. Chen, "*Efficient, broadband and wide-angle hot-electron transduction using metal-semiconductor hyperbolic metamaterials*." **Nano Energy**, vol. 26, pp.371-381, 2016.

M. Hajizadegan, V. Ahmadi, and M. Sakhdari, "*Design and analysis of ultrafast and tunable all optical metamaterial switch enhanced by metal nanocomposite*" **Journal of Lightwave Technology**, vol. 31, No. 12, pp. 1877-1883, 2013.

M. Hajizadegan, D. Fathi, M. Sakhdari, "*All-optical metamaterial switch based on Kerr effect with MWCNT composite*" **Physica E: Low-dimensional Systems and Nanostructures**, vol. 48, pp. 1-6, 2013.

D. Fathi, M. Sakhdari, and **M. Hajizadegan**, "*All optical SRR switch using carbon nanotube composite.*" **Optik-International Journal for Light and Electron Optics**, vol. 125, No.16, pp. 4405-4410, 2014.

CONFERENCES:

M. Hajizadegan, L. Zhu, and P. Y. Chen, "*Highly Directive Leaky-Wave Antennas Based On PT-Symmetric Metasurfaces.*"

In International Conference on Electromagnetics in Advanced Applications (ICEAA), 2019 Granada, Spain.

M. Hajizadegan and P. Y. Chen, "*A PT-Symmetric Metasurface and Its Exotic Waveguiding and Radiation Properties*." META 2019, Lisbon, Portugal, July 2019.

M. Hajizadegan, and P. Y. Chen, "*Gesture Recognition Using A Portable and Flexible Meta-Atom Panel and Machine Learning.*" In Antennas and Propagation & USNC/URSI National Radio Science Meeting, 2019 IEEE International Symposium on, Atlanta, GA.

M. Hajizadegan, M. Sakhdari, P.Y. Chen "*PT-symmetric inductive displacement sensors.*" In 2018 IEEE MTT-S International Microwave Workshop Series on Advanced Materials and Processes for RF and THz Applications (IMWS-AMP), pp. 1-3. IEEE, 2018.

M. Hajizadegan, and P. Y. Chen, "*Harmonics-Based RFID Sensor Based on Graphene Frequency Multiplier and Machine Learning*." In Antennas and Propagation & USNC/URSI National Radio Science Meeting, 2018 IEEE International Symposium on, pp. 1621-1622. IEEE, 2018.

M. Hajizadegan, Pai-Yen Chen, "*Parity-Time symmetric leaky-wave metasurfaces*", National Radio Science Meeting (URSI 2018), Boulder, Colorado, US, 2018.

M. Hajizadegan, and P. Y. Chen, "*A self-powered harmonic sensor based on simple graphene circuit and hybrid-fed antenna*." In Antennas and Propagation & USNC/URSI National Radio Science Meeting, 2017 IEEE International Symposium on, pp. 581-582. IEEE, 2017.

M. Hajizadegan, Pai-Yen Chen, "*Ultrasensitive Parity-Time symmetric wireless microsensors*", National Radio Science Meeting (URSI 2017), Boulder, Colorado, US, 2017.

M. Hajizadegan, P. Y. Chen, " *Efficient rectification of infrared radiation using nano-rectennas and slow-light microstructure*", 2016 IEEE International Symposium on Antennas and Propagation/USNC-URSI National Radio Science Meeting, Fajardo, Puerto Rico, 2016.

M. Hajizadegan, P. Y. Chen, "*Efficient, broadband and wide-angle hot-electron photoemission: a metamaterial approach*", National Radio Science Meeting (URSI 2016), Boulder, Colorado, US, 2016.

A. shahini, **M. Hajizadegan**, M. Sakhdari, P. Y. Chen, "*Self-Powered and transparent all-graphene biosensor*", IEEE SENSORS 2016 Conference in Orlando, Florida, 2016.

M. Hajizadegan, M. Sakhdari, and V. Ahmadi "*Design of a tunable all-optical metamaterial switch enhanced by metal nanocomposite*" 19th Iranian Conference on Optics and Photonics (ICOP), Zahedan University, Iran, 2013.

M. Hajizadegan, M. Sakhdari, and V. Ahmadi "*Investigation of density and distribution of metal nanoparticles effect on the plasmonic absorption in metal nanocomposite using FEM*" 1st National Congress and Workshop on Nanoscience and Nanotechnology (NCWNN), Tarbiat Modares University, Tehran, Iran, 2013.

M. Hajizadegan, M. Sakhdari, and V. Ahmadi "*Design of a Kerr effect based terahertz all-optical switch using metallic nanocomposite metamaterial structure*" Second Conference on Millimeter -Wave and Terahertz Technologies (MMWaTT), Tehran University, Iran, 2012.

S. Olyaee, **M. Hajizadegan** "*Design and implementation of a new optical microphone independent of membrane structure technology*" 2nd Iranian Conference on Optic and Laser Engineering (ICOLE), Isfahan, Iran, 2011.

PATENT:

P.Y. Chen, M. Sakhdari, **M. Hajizadegan**, M.M. Cheng, "*Parity-Time (PT)-Symmetric Wireless Telemetric Sensors and Systems*" U.S. Patent Application 62/695,133, filed on July 8, 2018, in progress.